



Novel edible, vegan and electroconductive bioinks for 3D Bioprinting

Diana Maria Condeço Marques

Thesis to obtain the Master of Science Degree in

Biotechnology

Supervisors: Prof. Frederico Castelo Ferreira and Dr. Paola Sanjuan Alberte

Examination Committee:

Chairperson: Prof. Helena Maria Rodrigues Vasconcelos Pinheiro

Supervisor: Dr. Paola Sanjuan Alberte

Members of the Committee: Prof. Jorge Manuel Ferreira Morgado

November 2021

Preface

I declare that this document is an original work of my authorship and that it fulfils all the requirements of the Code of Conduct and Good Practices of the Universidade de Lisboa. The work presented in this thesis was performed at the Institute for Bioengineering and Biosciences of Instituto Superior Técnico (Lisbon, Portugal), during the period September 2020 - August 2021, under the supervision of Prof. Dr Frederico Ferreira. The thesis was co-supervised by Dr Paola Sanjuan Alberte.

Acknowledgements

First, I must sincerely thank Professor Frederico Ferreira for believing in this project. Nothing would have been possible without your constant support, availability, and motivation to come up with new ideas and new solutions. Thank you for making me surpass myself and for making me grow as a scientist.

I would like to give a special thanks to Paola, who was always present and made herself available to help me in the lab. Thanks for your guidance, teachings, help, and motivation.

Thanks to all the members of the Bioengineering laboratory, especially those who helped me and worked with me directly (Laura Sordini, Leonor Resina, João Silva and Fábio Garrudo). Thanks to all members present at Alameda and all members of SCERG.

Personally, I leave my most enormous thank you to Catarina Vieira for supporting me and motivating me every day. Thanks for all the laughs, hugs, and walks to release my stress. Your support was essential to be where I am today. I'm very happy to have made this journey by your side. Thank you for believing in me and all my projects.

Thank you Diogo Estrela, the one who has been on my side for a long time. Thank you for listening to me, for lining up with me and for not letting me down. I also want to leave a big thank you to all my friends from *Rua Alfredo* who even in these difficult times marked their presence.

A giant thanks to Gonçalo Fernando. Thank you for sharing your knowledge with me, for helping and encouraging me to always seek more.

A huge thank you to my family. Thank you, Carolina, André, Pedro, and Daniel. Thanks, mom. Thank you for listening to my crazy ideas and motivating and encouraging me to move forward with them. You are the best. Thanks to all the other members who were essential and always supported me during my journey.

Finally, I would like to thank for the funding received from the FCT granted to the project Neuron (PTDC/CTM-CTM/30237/2017) to the Research Unit iBB - Institute for Bioengineering and Biosciences (UIDB/04565/2020 and UIDP/04565/2020) and to i4HB - the Associate Laboratory Institute for Health and Bioeconomy (LA/P/0140/2020). Importantly the research conducted on this thesis supported a successful application to the 2021 the Good Food Institute (GFI) Competitive Grant Program. (GFI) entitle "Algae2Fish", a project that started on September 2021 and therefore the team thanks to GFI for all the support.

Abstract

Cell-cultured fish has the potential to solve overexploitation of marine resources by growing fish stem cells in a laboratory-controlled environment and supported by an edible scaffold to manufacture fish tissue. This project aims to develop novel edible and electroconductive bioinks for 3D bioprinted vegan tissues fabrication using marine algae derivatives. Novel algae polysaccharides-based inks were successfully formulated and used to fabricate 3D scaffolds using 3D printing and 3D bioprinting. Ink formulation and printing parameters were optimised, allowing printability of 3D complex structures. Mechanical compression assays and dry weight estimations revealed young's modulus between 60-80 kPa and water contents above 97%, valuable properties for cell-cultured seafood, as found in fish species' natural tissues. Natural conductive conjugated molecules were added as dopants into the ink formulations to increase electroconductivity and support electrical stimulation of myogenic cell differentiation. The lit-up of an LED lamp demonstrated the electroconductive properties. Moreover, a slightly higher conductivity was estimated for wet hydrogels than that obtained for non-doped hydrogels. A predominance of capacitive behaviour was observed. Cell characterisation using L929 fibroblasts seeded on scaffolds showed high cell viability. However, the cell cultures carried on the doped scaffolds undergo a higher lag phase. The bioprinted cells were spread throughout the scaffolds with cells exhibiting a similar morphology to the controls. 3D structures with high viability were observed for fibroblasts cultured within the newly developed bioinks. Overall, we establish a strategy to manufacture 3D edible and electroconductive scaffolds with potential applications for cell-cultured food.

Keywords: edible scaffolds, 3D bioprinting, electroconductive hydrogels, algae polysaccharides

Resumo

Atualmente, uma solução para combater a sobre-exploração dos recursos marinhos é o desenvolvimento de peixe cultivado através do crescimento de células estaminais de peixe em laboratório, num ambiente controlado, com o auxílio de um *scaffold* comestível. Deste modo, este projeto tem como objetivo desenvolver novas bio-tintas comestíveis e eletrocondutoras para fabricar tecidos veganos bio-impresos, utilizando derivados de algas. Novas tintas à base de polissacarídeos de algas foram formuladas com sucesso e utilizadas para fabricar *scaffolds* usando impressão 3D e bio-impressão 3D. A formulação das tintas e os parâmetros de impressão foram otimizados, permitindo o fabrico de estruturas complexas. Ensaio mecânicos de compressão e valores estimados pelo peso seco das amostras revelaram que os géis possuem módulos de young entre 60-80kPa e mais de 97% em água, propriedades valiosas por serem semelhantes às de tecidos de espécies naturais de peixes. Moléculas naturalmente conjugadas foram adicionadas como dopantes às tintas, com o objetivo de aumentar a eletrocondutividade e suportar a estimulação elétrica da diferenciação miogénica. As propriedades electrocondutoras foram demonstradas ao acender um LED. Adicionalmente, estimou-se uma condutividade ligeiramente superior para hidrogéis dopados ao valor observado em tintas não-dopadas. Observou-se um predomínio do comportamento capacitivo nos hidrogéis. A caracterização celular com fibroblastos L929 depositados no topo dos *scaffolds*, demonstrou alta viabilidade. Contudo, as culturas mantidas nos *scaffolds* dopados resultaram numa fase de latência superior. Os fibroblastos bio-impresos espalharam-se pelos hidrogéis, exibindo um citoesqueleto semelhante ao controlo. Estruturas 3D com alta viabilidade foram observadas nas células cultivadas usando as novas bio-tintas. No geral, neste trabalho, estabelecemos uma estratégia para fabricar *scaffolds* 3D comestíveis com potencial para produzir alimentos cultivados em laboratório.

Palavras-chave: *scaffolds* comestíveis, bio-impressão 3D, hidrogéis eletrocondutores, polissacarídeos de algas

Contents

Acknowledgements	v
Abstract.....	vii
Resumo	ix
List of Tables	xiv
List of figures	xvi
List of abbreviations.....	xxii
1. Introduction	2
1.1. Motivation	2
1.1.1 Food industry impact on the environment	2
1.1.2 Marine ecosystems decline	3
1.1.3 Marine agriculture.....	4
1.2 State of the art in cell-cultured food industry	5
1.2.1 Tissue engineering for fish production: Cell-cultured fish	7
1.3 Aim, objectives, research strategy, and thesis outline	8
2. Theoretical Background.....	12
2.1 Tissue Engineering: current overview	12
2.1.1 Biomedical applications	12
2.1.2 Food applications	13
2.2 Materials for scaffolding design.....	14
2.2.1 Synthetic versus natural polymers	14
2.2.2 Edible materials	15
2.2.3 Natural available materials: marine resources	15
2.3.4 Electrically conductive materials	15
2.3 Hydrogels	16
2.3.1 Electroconductive hydrogels	16
2.4 Scaffolding fabrication techniques.....	17
2.4.1 Overview.....	17
2.4.2 3D extrusion bioprinting.....	17
2.5 Cell-material interactions	19
3. Materials and Methods	21
3.1 Ink formulation	21
3.1.1 Algae-based polysaccharide solutions	21
3.1.2 Doping with natural conjugated molecules.....	21
3.1.3 Ink nomenclature	22
3.2 Ink characterisation	23

3.2.1 UV-Visible spectra	23
3.2.2 Rheological Assessment	24
3.3 Scaffold characterisation	24
3.3.1 Casting hydrogels on moulds	24
3.3.2 Mechanical evaluation	25
3.3.2.1 Compression tests	25
3.3.3 Chemical and physical characterisation	26
3.3.3.1 Scaffold Water Uptake Evaluation (Swelling degree)	26
3.3.3.2 Water content evaluation	26
3.3.4 Surface proprieties	26
3.3.4.1 Evaluation of the surface wettability	26
3.3.4.2 Scanning Electron Microscopy (SEM)	28
3.3.5 Electrical proprieties	28
3.3.5.1 Electrochemical Impedance Spectroscopy	28
3.3.5.2 Four-probe method	29
3.3.5.3 Cyclic voltammetry	30
3.3.5.4 LED light test	30
3.4 3D Printing	30
3.4.1 Exploring different architectures	30
3.4.3 3D multi-layer structures	30
3.4.2 Printability evaluation	31
3.4.2.1 Printability factor	31
3.4.2.2 Line thickness	32
3.5. Cell seeding onto 3D scaffolds	33
3.5.1 Alamar Blue	33
3.5.2 Live/Dead viability assay via calcein-AM/ethidium homodimer-1 staining	34
3.5.3 Hoechst-Phalloidin staining	34
3.6 3D Bioprinting	34
3.6.1 Bioprinting media optimization	35
3.6.1.1 Bioink formulation	35
3.6.2 Bioprinting process	36
3.7 Statistical analysis	36
4. Results and Discussion	38
4.1 Ink formulation	38
4.1.1 Optimizing Algae-based polysaccharide ink concentration	38
4.1.2 Doping: dispersion of natural conjugated molecules	38
4.1.2 Cell Culture	40

4.1.2.1 Evaluation of formulation ingredients cytotoxicity	40
4.2 Ink characterisation	41
4.2.1 UV-Visible spectra	41
4.2.2 Rheological Assessment	42
4.2.2.1 Algae-based polysaccharide temperature-dependent behaviour	42
4.2.2.2 Algae-based polysaccharide gelation kinetics	43
4.3. Scaffold characterisation	45
4.3.1 Casting hydrogels on moulds	45
4.3.5.2 Four-probe method.....	56
4.3.5.3 LED light test	57
4.3.5.4 Cyclic voltammetry	57
4.4 3D Printing.....	58
4.4.1 Printability evaluation.....	58
4.4.1.1 Printability factor	58
4.4.1.2 Line thickness evaluation	60
4.5.1 Cell seeding onto 3D scaffolds.....	64
4.5.1.1 Alamar Blue	64
4.5.1.2 Live/Dead viability assay via calcein-AM/ethidium homodimer-1	65
4.5.1.3 Hoechst-Phalloidin staining	66
5. Conclusions and Future Perspectives.....	74
6. Bibliography	78

List of Tables

Table 1. Inks nomenclature according to the concentrations used during their formulation and respective colour code.	22
Table 2. Electrochemical impedance spectroscopy experimental parameters.....	29
Table 3. Pressure (psi) applied during printing and respective needle used for each ink. (Pink needle = 0.5 mm; orange needle = 0.6 mm)	32
Table 4. List of the methods available to disperse the vegetal conjugated molecules within the algae-polysaccharide ink. Stirring, emulsions, organic solvents, and ultrasound were considered. A brief description and feasibility output of each method is described.	38
Table 5. List of common edible fish species and their correspondent water contents in percentage with respective literature references.	49
Table 6. List of different shaped 3D printed scaffolds. An image of each scaffold is shown along with the parameters used during each printing process. Advantages and disadvantages of each structure were debated.....	61
Table 7. List of different shaped 3D printed multi-layered scaffolds mounted with intercalated inks. The illustration of each scaffold is shown along the real image after the mounting. Advantages and disadvantages of each structure were debated.	63

List of figures

Figure 1. A) Graphical representation of world population, in billions, from 1940 until 2020. B) Graphical representation of CO₂ in the atmosphere, in parts per million, from 1940 until 2020. C) Graphical representation of the remaining biodiversity, in percentage, from 1940 until 2020 (Alastair Fothergill, 2020). 3

Figure 2. A.T. Kearney analysis of global meat market forecast, in billion US\$, until 2040. Sources: United Nations, World Bank, expert interviews; Kearney analysis (Gerhardt *et al.* 2020). 6

Figure 3. A schematic cell-cultured fish approach. The process starts with cell extraction from a living fish, cell proliferation, and differentiation into a 3D bioprinted structured fish muscle tissue. (Figure created on BioRender) 7

Figure 4. Scheme of the thesis experimental strategy. 9

Figure 5. Cell-based seafood preparations. A. shrimp dumplings; B. salmon nigiri; C. fish maw; D. yellowtail. Source: (Marwaha Nisha, Beveridge Malcom 2020). 13

Figure 6. 3D printer scheme. At the right side there is a 3D printer nozzle. (Figure created on BioRender). 18

Figure 7. Illustration of the ink formulation procedure. A) Algae-polysaccharide dissolution at 80°C; B) Addition of particles of vegetal conjugated molecules to the algae-polysaccharide solution; C) Algae polysaccharide doped solution; D) Ultrasonic bath illustration; E) Vegetal conjugated molecules dispersed in the algae polysaccharide solution via ultrasonic exposure. Image created using BioRender. 21

Figure 8. A) The process of casting hydrogels using moulds. The process started with empty moulds that acted as a support structure until gelation occurred. After that, the mould was removed, and the solid hydrogel remained. 3D printed cylindrical moulds with 9 mm diameter and 4-8 mm in height were used as support to cast hydrogels. B) This process was performed for all formulate inks. Higher concentrations resulted in stronger colours. Image created using BioRender. 25

Figure 9. Illustration of the material surface-drop interaction with the Young's contact angle shown used the Young-Laplace fitting method..... 27

Figure 10. Illustration of the surface-drop behaviour obtained for materials with different wettability. Superhydrophilic surfaces show a Young's contact angle between 0 and 15, hydrophilic surfaces between 15 and 90, hydrophobic surfaces between 90 and 150, and superhydrophobic surfaces above 150. 27

Figure 11. Illustration of the hydrogels drying process using treatment with hexamethyldisilane (HMDS) and ethanol as dehydration solvents. The process was divided in 8 steps. Between each step were waited 20 minutes. The mixtures used are indicated below each illustration. Image created using BioRender. 28

Figure 12. Designs of different multi-layered structures to conjugate bioprinting with the enhancement of the electrical performance of the hydrogel. The constructs were manufactured intercalating layers of the 9AlgP ink and the 15AlgP_1molA or 15AlgP_5molA inks. A) circles (r = 4 mm) of intercalated inks; B) films of intercalated inks; C) parallel struts of intercalated inks; D) A large square surrounded by two squares of intercalated ink. Legend: white structures represent the 9AlgP ink and red structures represent the

15AlgP_1molA or 15AlgP_5molA inks; positive (+) and negative (-) symbols represent possible places for electrical current connection to induce structure polarization. 31

Figure 13. Illustration of the 3D printing process and following seeding experiment. 3D printed films (4 mm x 4mm) were fabricated directly into a petri dish using a printer at RT. After that, 50 000 mouse fibroblast cells were seeded in each film. DMEM (pink bottle) was added to the petri dish until the films were fully covered. The films were incubated for 8 days. Alamar Blue proliferation assay (at day 2 and day 7), Hoechst/Phalloidin staining (at day 5), and Live/Dead (at day 8) staining were performed. Image created using BioRender. 33

Figure 14. Illustration of the 3D bioprinting process. 3D bioprinted circles (r = 4 mm) were fabricated directly into a petri dish using a printer at RT. After printing, DMEM (pink bottle) was added to the petri dish until the circles were fully covered. The films were incubated for 8 days. Microscope observations and Live/Dead (at day 8) staining were performed. Image created using BioRender. 35

Figure 15. Ultrasonic bath duration of 15AlgP inks doped with 1, 5 and 10 g.L⁻¹ of molA or molB showing that higher concentrations require prolonged ultrasonic exposure. MolB particles disperse quicker than molA particles. 39

Figure 16. Cytotoxicity assay for biomaterials compounds. The viability of L929 fibroblasts cells grown on culture media (DMEM) supplemented with 15 g.L⁻¹ AlgP, 1 g.L⁻¹ molA, and 1 g.L⁻¹ molB using a WST-8 viability assay. Viability measured for 1h and 24h of incubation reveals a non-significative decrease. DMEM incubation shows higher viability than the supplemented media. Data are shown as mean ± SD (n=3). The student's test was performed (ns = not significant; * = 0.01 < p-value < 0.05). 41

Figure 17. A) Uv-visible spectroscopy spectra of 15AlgP, 15AlgP_1molA, 15AlgP_5molA, and 15AlgP_10molA hydrogels showing characteristic peaks forming at λ ≈ 460, 510, and 560 nm suggesting the presence of molA inside AlgP hydrogel. Black arrows indicate the mentioned peaks. B) Uv-visible spectroscopy spectra of 15AlgP, 15AlgP_1molB, 15AlgP_5molB, and 15AlgP_10molB hydrogels showing characteristic peaks forming at λ ≈ 520 and 565 nm suggesting the presence of molB inside AlgP hydrogel. Grey arrows indicate the peaks described in the text. 42

Figure 18. Rheological assessment of 15AlgP and 15AlgP_5molA inks. Temperature sweeps showing an increase in viscosity with decreasing temperature, indicating thermo-sensitivity. The addition of molA did not change the ink thermo-behaviour. Solid lines indicate the average values, and the dotted lines indicate the SD. Data are show as mean ± SD. 43

Figure 19. Monitoring the storage (G' —) and loss (G'' ----) modulus of 15AlgP, 15AlgP_1molA, 15AlgP_5molA, 15AlgP_10molA, 15AlgP_1molB, and 15AlgP_5molB inks for 10 minutes at 25°C. The values from y axis are presented in a confidential annex. 44

Figure 20. Graphical representation of the storage (G') and loss (G'') modulus of 15AlgP, 15AlgP_1molA, 15AlgP_5molA, 15AlgP_10molA, 15AlgP_1molB, and 15AlgP_5molB inks after 10 minutes of elapsed time, at 25°C. Data are shown as mean ± SD (n=3). Statistical significance was assessed using 2way ANOVA analysis showing non-significant (<0.9999) p-values for G'' and significant p-values for G' (* = 0.01 < p-

value < 0.05; ** = 0.0016; *** = 0.0009; **** < 0.0001). The values from y axis are presented in a confidential annex. 45

Figure 21. A) At left is shown the 5AlgP, 10AlgP, and 15AlgP inks once inside the 3D printed moulds, and at the right the respective structure after 5-10 minutes of gelation. 5AlgP, 10AlgP hydrogels were not solid while 15AlgP originated a solid structure. At the bottom 15AlgP based inks were used to construct hydrogels using moulds with different shapes B) 3D squared moulds (5 mm x 5 mm); C) 3D cylindric moulds with diameter a of 9 mm and 8 mm in height; D) 3D circle mould with a diameter of 9 mm and 2 mm in height. 46

Figure 22. A) Compression stress-strain curve of 15AlgP, 15AlgP_1molA, 15AlgP_5molA, and 15AlgP_10molA hydrogels. B) Stress-strain linear regressions of 15AlgP and 15AlgP_5molA showing $r^2 > 0.9$ and the calculated slope values (Young's modulus) in kPa. 47

Figure 23. Quantified Young's modulus of the 15AlgP, 15AlgP_1molA, 15AlgP_5molA, and 15AlgP_10molA hydrogels. A similar behaviour of Young's modulus is observed for all hydrogels. Data are shown as mean \pm SD. Statistical significance was assessed using t-student analysis showing non-significant p-values (p-value \geq 0.05). 48

Figure 24. A) Water content of the 15AlgP, 20AlgP, and 25AlgP hydrogels and of B) 15AlgP hydrogel compared with AlgP_1molA, AlgP_5molA, and AlgP_10molA. Data are shown as mean \pm SD (n = 3). Statistical significance was assessed using t-student analysis showing non-significant p-values (p-value \geq 0.05) and values with different significances (* = 0.01 < p-value < 0.05; ** = 0.001 < p-value < 0.01; *** = 0.0001 < p-value < 0.001). 49

Figure 25. A) Swelling degree for 10AlgP, 15AlgP, 20AlgP, and 25AlgP hydrogels at days 3, 5, and 7. Swelling reaches a swelling of 10% at day 3. B) Swelling degree for 10AlgP, 15AlgP, 20AlgP, and 25AlgP hydrogels at days 3, 5, 7 and 40. Data are shown as mean \pm SD (n = 3). 50

Figure 26. Surface properties of the 15AlgP, AlgP_5molA, and AlgP_5molB hydrogels. A) The hydrogels show low contact angles, typical of superhydrophilic specimens. Data are shown as mean \pm SD. B) Representative images of each contact angle measurement. 51

Figure 27. Scanning electron microscopy (SEM) images of the scaffolds. A) SEM images of 15AlgP hydrogel showing a sponge-like (top image), and flake-like (bottom image) structures; B) SEM images of 15AlgP_1molA, 15AlgP_5molA, and 15AlgP_10molA hydrogels also showing flake-like structures (at 10g.L⁻¹). C) SEM images 15AlgP_1molB, 15AlgP_5molB, and 15AlgP_10molB hydrogels with similar flake-like structures (at 5g.L⁻¹) and indicating the formation of molB particles (at 10g.L⁻¹) on the hydrogel surface in comparison to non-doped 15AlgP hydrogel. White arrows indicate the presence of molB particles surrounded by the AlgP matrix. D) SEM images of 15AlgP hydrogel and structures that can be crystals at the hydrogel surface. 52

Figure 28. EIS Bode plot of 15AlgP, 15AlgP_1molA, 15AlgP_5molA, and 15AlgP_10molA wet hydrogels. The x-axis is a logarithmic scale of the frequency, and the y-axis is the logarithm of the impedance, |Z|, while the second ordinate is the phase angle, θ . 15AlgP hydrogel shows higher impedance than molA doped

hydrogels. Data are show as mean \pm SD (n=3). The values from y axis are presented in a confidential annex. 54

Figure 29. EIS Nyquist plot of wet hydrogels doped with varying concentrations of natural conjugated molecules: 15AlgP, 15AlgP_1molA, 15AlgP_5molA, 15AlgP_10molA, and 15AlgP_10molB. The negative imaginary impedance $-Z''$ is plotted versus the real part of the impedance Z' . The values from y axis and x axis are presented in a confidential annex. 54

Figure 30. Equivalent circuit of the fabricated scaffolds system composed of a constant phase element (CPE), a Rct (Charge transfer resistance), and a Ws (Warburg element) representing the diffusional impedance. Rs is the solution resistance. 55

Figure 31. Conductivity of wet 15AlgP, 15AlgP_1molA, 15AlgP_5molA, 15AlgP_10molA, and 15AlgP_10molB hydrogels. Data are shown as mean curves \pm SD. 55

Figure 32. Electrical conductivity of dried 15AlgP, 15AlgP_1molA, 15AlgP_5molA, 15AlgP_10molA, 15AlgP_1molB, 15AlgP_5molB, 15AlgP_10molB evaluated via four-point probe measurements. Non-doped 15 AlgP showing less conductivity than doped hydrogels, except for 15AlgP_5molA. Lower concentrations of molA and molB resulted in higher conductivities. The conductivity of 15AlgP_1molB hydrogels is almost four times higher than 15AlgP_1molA hydrogel. Data are shown as mean \pm SD (n=3, except for 15AlgP_5molA due to sampling problems). Statistical significance was assessed using t-student analysis showing non-significant p-values (p-value \geq 0.05) and values with different significances (* = 0.01 < p-value < 0.05; ** = 0.001 < p-value < 0.01).. 56

Figure 33. A) Images of a DC circuit conducted using 15AlgP_5molA hydrogel and a LED. B) Quantified LED intensity using the area of emitted light. A conductive metal was used as o positive control and the air as the negative control. 57

Figure 34. Cyclic voltammetry measurement at different scan rates (0.04 V.s⁻¹, 0.1 V.s⁻¹, and 0.4 V.s⁻¹) of all the fabricated hydrogels indicating an enlargement of the curve area with the increase of the voltage scan rate. 58

Figure 35. A) Optical microscopy images of 3D-printed 15AlgP, 15AlgP_1molA, 15AlgP_5molA, 15AlgP_10molA, 15AlgP_1molB, and 15AlgP_5molB squared meshes (top) and the light microscope image of each evaluated square inside the respective squared mesh (bottom). B) Printability factor (Pr) derived from the 3D-printed hydrogels, is inversely proportional to pore-circularity, an indicator of pore circularity and hence printability of the ink (Pr = 1 perfectly square pore, Pr < 1 circular pore, and Pr > 1 over-gelated pore). The grey region marks the range of adequate ink printability (from 0.85 to 1.1) (Ouyang et al. 2016). Data are shown as mean \pm SD (n=7). 59

Figure 36. Optical microscopy images of 3D printed 15AlgP_5molA squared meshes with 1, 2, and 3 printed layers. 60

Figure 37. Line thickness over three different layers derived from the 15AlgP, 15AlgP_5molA, and 15AlgP_5molB 3D-printed hydrogels showing the expected line thickness marked with a black dotted line (0.5 mm = pink needle inner diameter). Data are shown as mean \pm SD (n=3). The values from y axis are presented in a confidential annex. 60

Figure 38. 3D printed films(10 mm x 10 mm) of 15AlgP, 15AlgP_5molB, and 15AlgP_molA. 64

Figure 39. Proliferation assay. AlamarBlue™ reduction as an indirect estimation of cell number of mouse fibroblasts seeded in different 3D printed films. Cells were seeded in 3D printed films on day 0. At day 2 and day 7 after seeding, AlamarBlue™ was added to the medium and incubated for 2h. The reduction of AlamarBlue™ was detected using fluorescence (excitation at 560 nm and emission at 590 nm) in a plate reader. Each column shows the mean ± SD of three independent experiments (n=3) with three 3D printed films for each condition. 65

Figure 40. A) Fluorescence microscope images of L929 fibroblast cells seeded onto 3D printed films after staining with calcein/ethidium homodimer-1, at day 8. B) Cytocompatibility study of 15AlgP, 15AlgP_5molA, and 15AlgP_5molB hydrogels using a Live-Dead viability assay. Data are shown as mean ±SD (n=3). Scale bar: 500 µm. 66

Figure 41. Fluorescence microscope images of L929 fibroblast cells adhered on 15AlgP, 15AlgP_5molA, and 15AlgP_5molB 3D printed films, after 5 days in culture. Alexa 488 Phalloidin stained actin cytoskeleton (green) and Hoechst 33342 stained the cell nuclei (blue). Scale bar: 500 µm. 66

Figure 42. A) Number of clusters present at each 3D printed hydrogel (15AlgP, 15AlgP_5molA, and 15AlgP_5molB); B) separation of the clusters by size (very small, small, medium, large, and very large) according to the number of cells per cluster. The number of cells per cluster size legend is represented at right side. 68

Figure 43. A) Light-microscope images of L929 fibroblast cells grown on DMEM (positive control), Triton-X (negative control), and Media 3 after 30 and 120 minutes of incubation. Cells incubated in media 3 show similar proliferation and morphology as cells incubated in DMEM. B) Respective viability percentage of L929 fibroblasts cells grown on DMEM, Triton-X, and Media 3 using a WST-8 viability assay. Viability measured at 30, 60 and 120 minutes of incubation is similar and reveals a non-significative decrease on viability when using media 3. C) Absorbance at 450 nm (A.U.), measured at 30, 60 and 120 minutes, for L929 fibroblasts cells grown on DMEM, Triton-X, and media 3. Scale bar: 500 µm. 69

Figure 44. A) Inks with 10g.L⁻¹ and 5g.L⁻¹ AlgP in 1L of Media 3 showing a solid and liquid state, respectively. B) 3D printed circles. Inks with 7g.L⁻¹, 8g.L⁻¹, and 9g.L⁻¹ AlgP in Media 3. 70

Figure 45. Light-microscope images of 3D bioprinted 9AlgP rings after 11 days in culture, at different magnitudes (x4, x10, and x20). The black dotted lines highlight the interface between the ring and the culture plate, showing the curvature of the bioprinted rings. 70

Figure 46. Light-microscope images of 3D bioprinted 9AlgP, 9AlgP_1molA, and 9AlgP_5molB rings at day 8. Scale bar: 500 µm. 71

Figure 47. A) Fluorescence microscope images of 3D bioprinted L929 fibroblast cells after staining with calcein/ethidium homodimer-1, at day 8. B) Cytocompatibility study of 9AlgP, 9AlgP_5molA, and 9AlgP_5molB hydrogels using a Live-Dead viability assay. Data are shown as mean ±SD (n=4). Scale bar: 500 µm. 72

List of abbreviations

PBS - Phosphate-buffered saline buffer solution

RT – Room Temperature

3D – Three-dimensional

4D – Four-dimensional

GHGs - Greenhouse gases

CSO – Chief strategy officer

GFI – The Good Food Institute

iPSCs - Induced pluripotent stem cells

hiPSCs - Human-induced pluripotent stem cells

hMSCs - Human mesenchymal stem cells

ASCs - Adipose tissue-derived stem cells

CRISPR - Clustered regularly interspaced short palindromic repeats

TE – Tissue engineering

ECM – Extracellular matrix

GAGs - Gmolsaminogmols

NASA - National Aeronautics and Space Administration

PEG - Poly(ethylene gmols)

PEO - Poly(ethylene oxide)

PLA - Poly(lactic acid)

PGA - Poly(gmolsic acid)

PCL - Poly-(caprolactone)

CPs – Conducting polymers

PPy - Polypyrrole

PANI - Polyaniline

PT - Polythiophene

PEDOT - Poly(3,4-ethylene dioxythiophene)

TSP – Textured soy protein

DMEM - Dulbecco's Modified Eagle's Medium

FBS - Fetal Bovine Serum

EDTA - Ethylenediaminetetraacetic acid

WST-8 - Water-soluble tetrazolium salt

OD – Optical density

G' - Storage modulus

G'' - loss modulus

SEM - Scanning Electron Microscopy

HMDS - hexamethyldisilane

AC - Alternating current

DC – Direct current

LED - Light-emitting diode

EIS – Electrochemical impedance spectroscopy

CV – Cyclic voltammetry

GFP - Green fluorescent protein

UV – Ultraviolet

Chapter 1. Introduction

1. Introduction

1.1. Motivation

1.1.1 Food industry impact on the environment

Humanity relies entirely on the existing ecosystems and their wellbeing. In turn, ecosystems welfare and prosperousness rely on their biodiversity. The variety of life in every habitat is tightly linked and genuinely dependent on living beings' interactions and dynamics. However, a loss of biodiversity has been observed over the past years (Figure 1A). Nowadays, the human population represents around 30% of the planet's mammals, living the consequences of extensive overexploitation of resources. The other 60% are animals for human consumption, and there are only 4% of the remaining species (Alastair Fothergill, 2020). The collapse of the natural world has thrown the planet off balance, resulting in global warming and climate change. Today, freshwater supplies are shrinking, agricultural yields are dropping, forests are burning, ice is melting, and rising oceans are more acidic, all, in part, due to a warmer climate. In 40 years, the summer sea ice in the Arctic has decreased by 40% (Alastair Fothergill, 2020). Climate change is altering the time of life cycles, causing many species to relocate as their ecosystems change, most immediately in coral reefs, forests, mountains, the Arctic, and in some cases, leading to death or even extinction. Changes observed in Earth's climate since the early 20th century are driven by human activities as fossil fuel burning, which increases heat-trapping greenhouse gases (GHGs) levels in the atmosphere (Figure 1B), raising Earth's temperature and promoting global warming. However, another issue is at the heart of all these global problems: human demand and reliance on animal products. Animal agriculture is responsible for nearly 40% of the planet's entire land surface. Most of that land is directed to raise grains, fruits, and vegetables that support animal growth, directly inducing deforestation (Bryan Walsh 2013; Phelps and Kaplan 2017). More precisely, every year, humans cut down 15 billion trees. Also, nearly 300 million tons of animals are slaughtered every year, just including beef, pork, and chicken. On the other side, the human population is continuously increasing (Figure 1C). It is expected to grow up to 9.8 billion by 2050, which will require annual meat production to rise substantially to 470 million tonnes (ONU 2019; Heidemann *et al.* 2020).

The scenario is also critical in the oceans, with 96.4 million tons of fish captured every year (FAO 2020). Moreover, intensive fishing drags to death thousands of specimens not intended for consumption. Today, fish stocks are under considerable pressure, with 29% of fish stocks classified as overfished and 61% of them as fully exploited (WWF 2015). Besides this, animals grow under intensive and degrading conditions leading to diseases, viral outbreaks and bacteria, which management implies the use of antibiotics and consequentially the appearance of antibiotic-resistant bacteria (Scanes 2017). Indeed, the animal industry contributes to 14.5% of all worldwide GHGs emissions (Rojas-Downing *et al.* 2017). Livestock and their by-products account for million tons of carbon dioxide (CO₂) per year, as well as other GHGs, such as methane (CH₄) and nitrous oxide (N₂O), which are gases with global warming potentials 28

and 265 times higher than CO₂, respectively (Rojas-Downing *et al.* 2017). Moreover, the growing demand for animal farming is expected to significantly contribute to a roughly 80% increase in global GHGs emissions from the agricultural sector (Tilman and Clark 2014). Therefore, the production and use of this protein feed source causes severe environmental impact detrimental to the land, air, water, and significantly contributes to global climate change by deforestation worldwide, and, therefore, present a significant threat to the world's biodiversity.

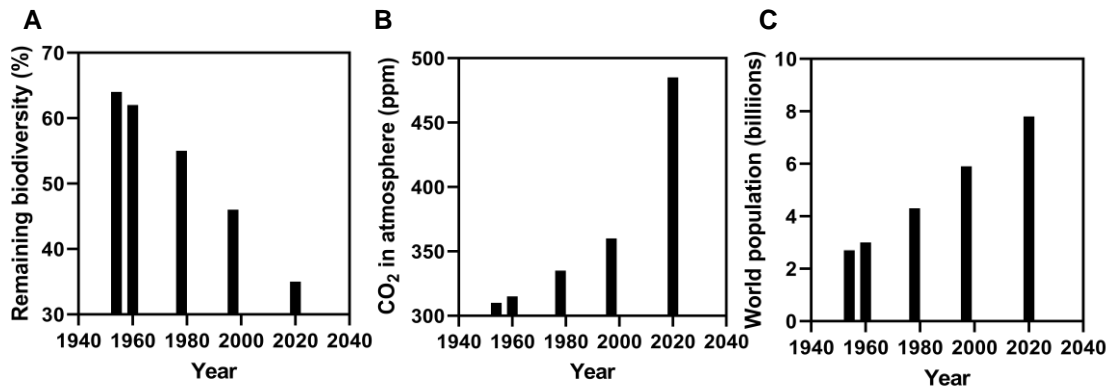


Figure 1. A) Graphical representation of world population, in billions, from 1940 until 2020. B) Graphical representation of CO₂ in the atmosphere, in parts per million, from 1940 until 2020. C) Graphical representation of the remaining biodiversity, in percentage, from 1940 until 2020 (Alastair Fothergill, 2020).

1.1.2 Marine ecosystems decline

Marine ecosystems include the open ocean, the deep-sea ocean, and coastal marine ecosystems, each of them with different physical and biological characteristics. These ecosystems are essential for the existence of life on this planet. Human wellbeing depends on water and on the ocean as it can support or change existing landscapes and form new ones, support economic activities and transportation, and be the primary source for protein for one in seven of the world's population (Henson *et al.* 2017). The ocean covers 71% of Earth's surface, is home to many ecosystems, supports a rich wildlife biodiversity, sustains billions of people's lives, regulates the climate, produces half the atmospheric oxygen, and fuels the water cycle (CQ Press 2020). However, after decades of overexploitation these functions are being compromised. As the global temperature increases, the concurrent ocean acidification, deoxygenation, and sea-level rise is severely impacting vital marine ecosystems (Gattuso *et al.* 2018). The rate at which these conditions emerge means that species have less time to either adapt or migrate, potentially increasing ecosystem disruption (Henson *et al.* 2017). An example of these ecosystem reconfigurations is the Australian reef communities which, after decades of ocean warming and critical ecological damaging, lost their defining kelp forests and became dominated by persistent seaweeds (Wernberg *et al.* 2016). There is also evidence that warm water species are being displaced towards the poles and experiencing changes in their size and habitat productivity (Reddy 2015). Additionally, a problem of great concern is plastic. Microplastics exposure has

many adverse effects on marine animals, such as mortality, reduced feeding rate, body mass, reduced allocation of energy for growth, and behavioural responses changes (Barboza *et al.* 2018). Models have estimated that over 5 trillion pieces of plastic are floating in the world's oceans and that its impact is comparable with persistent pollutants, being a global threat (Galloway *et al.* 2017).

1.1.3 Marine agriculture

Marine agriculture already supports 20% of global demand for consumed animal protein, including fish, crustaceans, molluscs, and other aquatic animals, excluding reptiles, seaweeds, and other aquatic plants (Potter *et al.* 2020). Fish and seafood products are a source of high-quality protein, polyunsaturated omega-3 fatty acids and various micronutrients such as iron, zinc, vitamin A, and vitamin B₁₂. However, human activities such as industrialised fishing pose severe challenges to marine ecosystems, and today the oceans are vulnerable. Besides fish farming, aquaculture has been expanding in recent decades to fill the gap between supply and demand and it is now the fastest-growing food production system (Potter *et al.* 2020). Although there is a high market demand for fish, there is several reports pointing out that aquaculture's growth will face alarming environmental challenges (Cheung *et al.* 2018; Ahmed *et al.* 2019). Such challenges include habitat destruction, water pollution, eutrophication, biotic depletion, ecological effects, and disease outbreaks (Ahmed and Thompson 2019). Moreover, aquaculture settings utilising antimicrobials may serve as reservoirs for antimicrobial resistance genes, providing routes for human and animal exposure to antimicrobial-resistant bacteria. It is estimated that global antimicrobial consumption in aquaculture will increase by 33% between 2017 and 2030 (Schar *et al.* 2020). Climate change affects weather conditions leading to fluctuations in ocean currents that alter the aquaculture dynamics (Maulu *et al.* 2021). Aquatic animals metabolic rates, growth and reproductive cycles are drastically affected by rising temperature (Sarkar *et al.* 2019). In aquaculture, changes in temperature, pH, salinity, and ecosystem health change productivity and increase several risks (Reddy 2015). Currently, innovation and revolutionary ideas represent the best strategy to overturn these situations and achieve sustainable marine agriculture in the future.

1.1.4 Marine food security: risks to seafood consumers

Even though fish and seafood carry numerous health benefits, contaminants present in this food group can pose a significant threat to consumers health. For example, marine organisms ingest and uptake microplastics that induce adverse effects and accumulate in many species, mainly top predators. Bioaccumulation and biomagnification into food chain increase the risks and toxic effects. Moreover, microplastics may act as vehicles for toxic chemicals (carcinogens, endocrine disruptors, neurotoxic chemicals) (Barboza *et al.* 2018). On the other hand, heavy metal pollution produced by anthropogenic sources such as agricultural drainage, industrial effluent discharge, sewage discharge, accidental chemical waste spills, and gasoline from fishing boats also has high negative impacts on fish health and fish consumers (Arulkumar *et al.* 2017). Heavy metals such as mercury (Hg) are widespread contaminants in

fish products. A recent assessment of metals bioaccumulation in global marine food chains has shown that Hg, lead (Pb) and zinc (Zn) are the most worrying magnifiers (Sun *et al.* 2020; Bosch *et al.* 2016). Furthermore, in aquaculture, antibiotics are incorporated into the feed or fed directly into the water. Consumption of antibiotics-contaminated food could pose risks to human health (Liu *et al.* 2017a). Moreover, in the aquaculture environments 80% of the antibiotics administered to fish are excreted without being completely decomposed, being able to reach other environments, diffuse into sediments, or being washed away by currents to remote locations (Manage 2018). This dissemination could end up providing antibiotic-resistant pathogenic bacteria (such as *A. salmonicida*, *A. hydrophila*, *C. freundii*, *V. salmonicida*, *F. psychrophilum* and *P. fluorescens*) to humans through drinking water, handling or consumption of aquaculture fish (Manage 2018; Liyanage *et al.* 2021). Manage also alarms to the risk of potential horizontal gene transfer from fish pathogens to humans due to the rapid growth of aquaculture sector (Manage 2018). Recently, Hui Chen and colleagues detected several antibiotics in the water, sediments and fish tissues showing high transportability and accumulation for the fish bile, liver and muscle, posing potential health risks to the consumers (Chen *et al.* 2018).

Nowadays, consumers are increasingly concerned about the quality effects of fish consumed and effects of it on human health (Mitchell 2011; Altintozglou *et al.* 2016). Consumer concerns include the potential ingestion of the substances mentioned above that may be incorporated in the fish, crustaceans, molluscs, and other seafood products. Therefore, alternative seafood without microplastics, mercury, parasites, or other common toxins are sought (Mason-Jenkins 1991; Farady 2019).

1.2 State of the art in cell-cultured food industry

As mentioned above, animal agriculture presents a significant threat to the planet environment with highly damaging impacts on biodiversity, soils, air, water, animal welfare and human health. Therefore, cell-cultured food has emerged as a breakthrough technology for the food industry that provides an alternative to animal intensive agriculture and farming (Hocquette 2016). Moreover, the adverse impacts of climate change on the planet and respective public awareness on urgency to act is changing consumers' mindset to be more prone to accept meat alternatives such as plant-based and cell-cultured meat (Bryant *et al.* 2019). Also, consumers' demand for sustainable and health beneficial food products with functional ingredients has recently increased (Zhang *et al.* 2012). Furthermore, cell-cultured meat is a potential solution to meet the increasing demand for proteins due to the expected population increase. Compared with conventional meat production, it could use 7-45% less energy, 99% less land, 96% less water, and emit 78-96% fewer GHGs (Choudhury *et al.* 2020). Combining tissue engineering approaches and biotechnology knowledge, it is potentially possible to grow *in-vitro* meat tissues from an animal cell biopsy, instead of growing animals for that purpose. In the first step, a cell is extracted from a living animal, is fed with a media to proliferate in a 3D scaffold material to differentiate into structured muscle and fat cells that resemble meat. There are critical research areas associated with cell-cultured meat production: cell culture

medium formulation, cell line development, scaffolding and product structuring and bioreactor design and bioprocess.

According to industry experts, novel vegan meat replacements and cell-cultured meat have significant commercial potential to disrupt the \$1,000 billion conventional meat industry. Based on A.T. Kearney analysis, around one-third of the global meat supply will be provided by these new technologies within the next ten years (Gerhardt *et al.* 2020). Novel vegan meat replacements is forecast to sharply grow until 2030, whereas cell-cultured meat is, in that study, expected to outgrow them between 2025 and 2040 due to technological advancements and consumer preferences (Figure 2) (Gerhardt *et al.* 2020a).

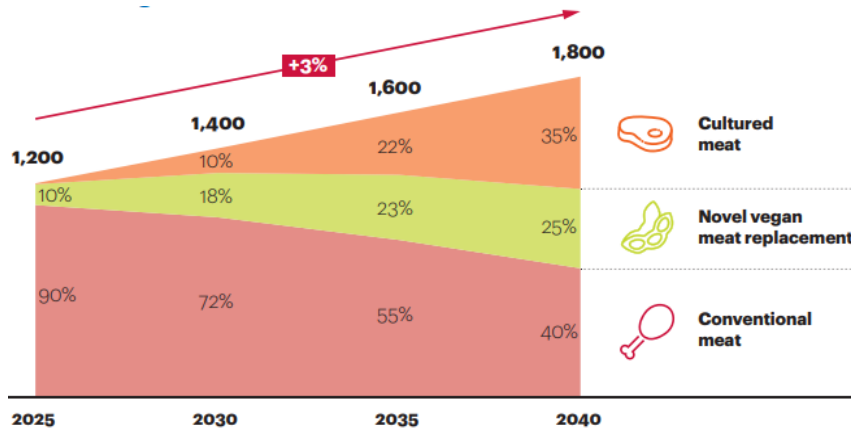


Figure 2. A.T. Kearney analysis of global meat market forecast, in billion US\$, until 2040. Sources: United Nations, World Bank, expert interviews; Kearney analysis (Gerhardt *et al.* 2020).

Since the first slaughter-free cell-cultured hamburger was unveiled in 2013 by Mosa Meat’s CSO, Prof. Mark Post, cell-cultured agriculture has received extraordinary attention. Many companies have been founded to commercialize cultured meat products (Post 2014). Besides meat alternatives, several companies focus on novel cell-cultured seafood, leather, silk, egg white, and milk. According to The Good Food Institute’s (GFI) external company database, nearly 80 start-ups worldwide work on cell-cultured meat-related topics. While the primary business model is business-to-consumer (B2C), other business-to-business (B2B) models have emerged that produce serum-free cell culture, plant-based growth factors, cell lines, and edible scaffolds. In 2019, “GFI state of the industry report” on cell-cultured meat revealed that 55 early-stage companies announced to aim at producing cell-cultured meat and seafood or at serving these producers along the value chain that year. From these, 33 position themselves as future cell-cultured meat producers (beef, chicken, pork, duck, horse, kangaroo, and others), 7 as future cell-cultured seafood producers (tuna, salmon, crustaceans, fish maw, and sturgeon), and the other 15 companies envisaged B2B business models.

1.2.1 Tissue engineering for fish production: Cell-cultured fish

Oceans and other marine ecosystems are particularly vulnerable due to the highly negative impacts of overfishing and climate change. With oceans at risk, cell-cultured seafood provides a unique opportunity to transform the sustainability landscape of these products by avoiding marine capture or aquaculture systems. Cell-cultured fish suggests that it is possible to extract cells from a living fish, feed them with serum-free media to proliferate in a 3D scaffold, and differentiate them into structured muscle and fat cells organised in structures that resemble fish tissue (Figure 3). In this way, it is possible to supply fish protein for human consumption with high nutritional value, without harming animals and avoiding contaminants or antibiotics. Furthermore, cell-cultured fish has advantages over cell-cultured meat, such as lower culture temperature and adaptation to hypoxia conditions that make them uniquely suited for bioreactor environments (Rubio *et al.* 2019). Also, all sectors that involve the production of cell-cultured fish still need extensive research. Few cell lines are available from marine species, seafood scaffolding and large-scale culture environments remain speculative. However, these technological gaps represent opportunities for research innovation advances. Moreover, with the growing interest and knowledge in cell-cultured agriculture for meat production, the investigation focused on cell-cultured seafood production is highly relevant. Cell-cultured fish is an innovative and relevant area with many opportunities and challenges with extreme investment and growth potential in future markets.

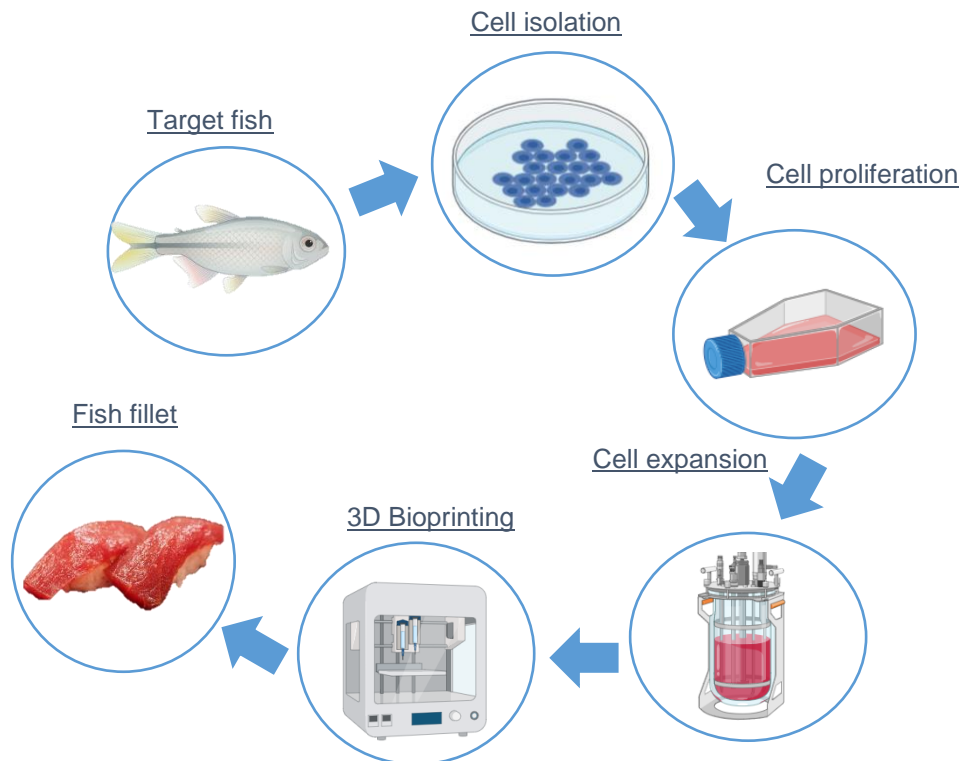


Figure 3. A schematic cell-cultured fish approach. The process starts with cell extraction from a living fish, cell proliferation, and differentiation into a 3D bioprinted structured fish muscle tissue (Figure created on BioRender).

1.3 Aim, objectives, research strategy, and thesis outline

This work aims to fabricate novel edible, vegan, and electroconductive bioinks for 3D bioprinting. The objectives of this work are the development of novel edible and electroconductive scaffolds for cell-cultured fish, able to fulfil three purposes:

- Prepare ink formulations for 3D printing and 3D bioprinting, 100% composed of vegan materials, thus allowing their edibility when further used to produce the cell-cultured tissue.
- Characterise the scaffolds obtained in terms of their mechanical properties, electrical conductivity, and 3D printability. Natural conjugated molecules were added, aiming to increase material electroconductivity for their further use to support electrical stimulation of myogenic differentiation.
- Validate the cytocompatibility of the materials by fibroblast cultivation on the surface of 3D printed structures or inside the hydrogels after their 3D bioprinting.

To achieve the goals proposed, six milestones were defined:

1. Ink formulation
2. Ink characterisation
3. Scaffold characterisation (properties of the solidified hydrogel)
4. 3D printing & 3D bioprinting
5. Printability evaluation
6. Biological characterisation

For each milestone, specific experimental methods were developed that are specified in the following Chapter 3.

To achieve the goals proposed for this thesis, the subsequent experimental strategy was followed:

The ink was formulated to fulfil the previously stated requirements. Then this ink was extruded by a 3D printer following a specific 3D designed model and printing parameters. The formed 3D hydrogels were then subsequently characterized. Characterization and optimisation studies were made on the materials, namely concerning the assessment of mechanical properties and electrical conductivity. The biological response via fibroblast cell culture was also assessed. The experimental strategy followed in this study is outlined in Figure 4.

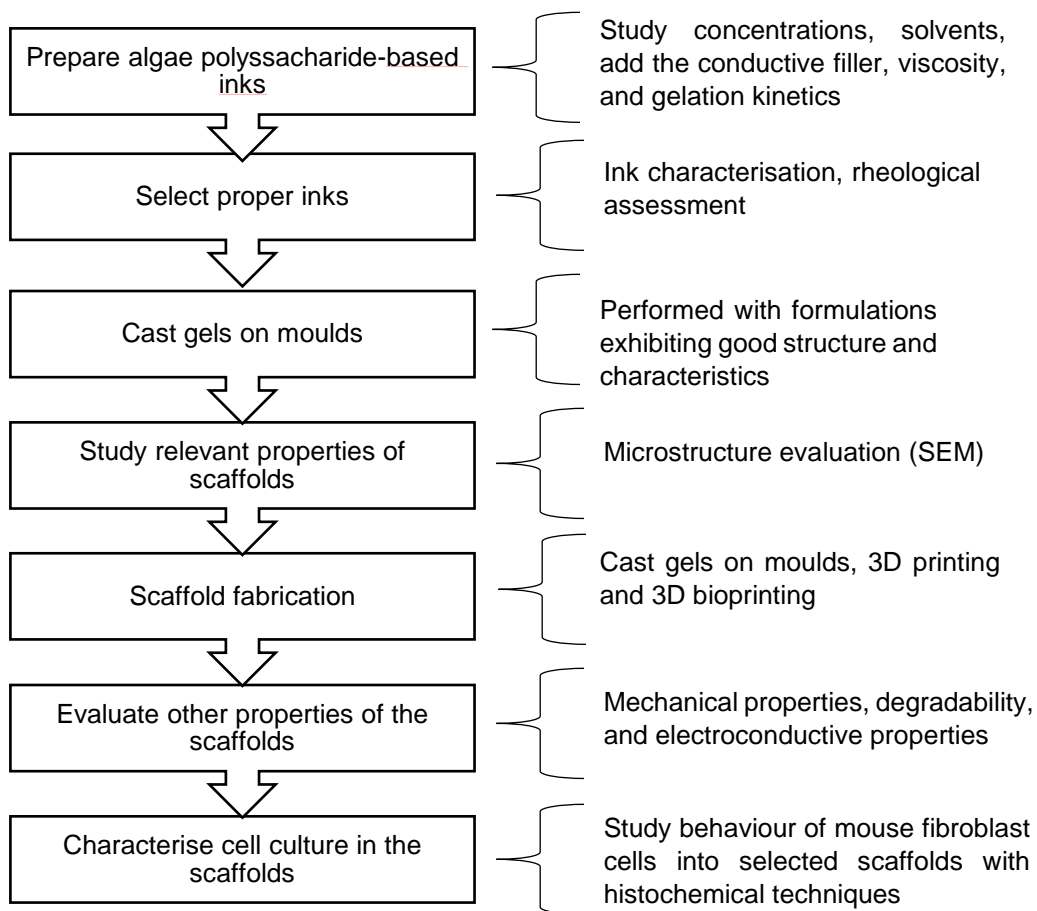


Figure 4. Scheme of the thesis experimental strategy.

Chapter 2. Theoretical Background

2. Theoretical Background

2.1 Tissue Engineering: current overview

In the past decade, tissue engineering (TE) advanced significantly combining knowledge gained from biology, materials science, chemistry research fields with engineering strategies. The discovery of induced pluripotent stem cells (iPSCs) and the clustered regularly interspaced short palindromic repeats (CRISPR) enabled specific cell manipulation and novel personalised medicine. On the other hand, adult stem cell research had a remarkable breakthrough by discovering that mesenchymal stromal cells (MSCs) produce a pool of desired growth factors and cytokines beneficial for local wound healing or disease treatment. Moreover, applying rigorous *in vitro* selection processes and directed evolution has facilitated more versatile engineered biomolecule delivery systems. However, all these advances and discoveries would not be possible to apply to tissue engineering approaches if biomaterials engineering and scaffolding fabrication methods had not evolved tremendously. Advances in fabrication technologies, including programmed self-assembly and 3D bioprinting, allowed the generation of high-resolution biomimetic structures with multiple cell types that recreate the extracellular matrix (ECM) architecture (Khademhosseini and Langer 2016).

2.1.1 Biomedical applications

TE and regenerative medicine are part of the biomedical research areas with a potential high impact on human health-related issues. There are currently applications in developing and constructing tissues and/or organs like nerves, bones, cartilages, skin, liver, pancreas, and muscles. Furthermore, for applications related to drug screening, the advances mentioned above led to the construction of human iPSCs-derived organoids and organ-on-chip platforms that integrate biomimetic organ models capable of screen drugs, their responses and side effects (Khademhosseini and Langer 2016). Recent experimental works have successfully constructed complex organ substitutes such as bone, nerve conduits, blood vessels, liver, and heart valves. In TE, developing materials and topographies that highly resemble the natural components of the ECM promotes cell functions such as cell adhesion, proliferation, and differentiation. Scaffolds are structures made of materials engineered to form new functional tissues that recreate the *in vivo* microenvironments. Scaffolds require intrinsic biocompatibility and proper chemistry to induce molecular biorecognition from cells (Carletti *et al.* 2011). Materials, mechanical scaffold properties, and degradation kinetics with non-toxic degradation products are critical and must be tailored to the specific TE application. For scaffolds, a 3D pore structure with tuneable pore sizes, exposed surface area, and porosity play a significant role, allowing the transportation of nutrients and wastes, well as influencing the distribution of cells within the scaffold volume and the architecture of the produced ECM (Carletti *et al.* 2011). Besides, scaffolds should provide appropriate mechanical properties and stability to resist stresses and maintain the designed construct structure's integrity (Zhao *et al.* 2018). Also, the scaffold should

provide, or recruit from the media, suitable proteins to promote cells adherence to it. In this work, we intend to develop a scaffold specific to cell-cultured fish. For example, fish glycosaminoglycans (GAGs) could be vital to promote cell attachment when developing such a scaffold. Scaffold properties, biomaterials and fabrication conditions will be dependent on the fish species and the type of cells. A polymer scaffold has various topological formulations such as film, sponges, meshes, fibres, and foams. For example, aligned fibre meshes that mimic muscle cell alignment can improve tissue texturization. However, films and softer scaffolds will be more suitable to produce fish adipose tissue.

2.1.2 Food applications

More recently, other unconventional applications have emerged that take advantage of engineered tissues being potentially edible (Khademhosseini and Langer 2016). Cell-cultured meat and seafood projects aim to reduce GHGs emissions produced by animal farming and improve animal welfare. This alternative purpose to replicate the organoleptic properties (i.e sensory and nutritional profile) of conventional food products through cultivation of the same cell types within a similar 3D structure as in natural animal products (Halpern *et al.* 2021). For example, in few years, the recent emergent cell-cultured seafood industry successfully grown shrimp, salmon, fish maw, and yellowtail (Figure 5) (Marwaha Nisha, Beveridge Malcom 2020). Besides these alternatives, several researchers are focus on producing novel cultured leather, silk, egg white, milk, gelatine and even mouse meat for pet feed purposes.

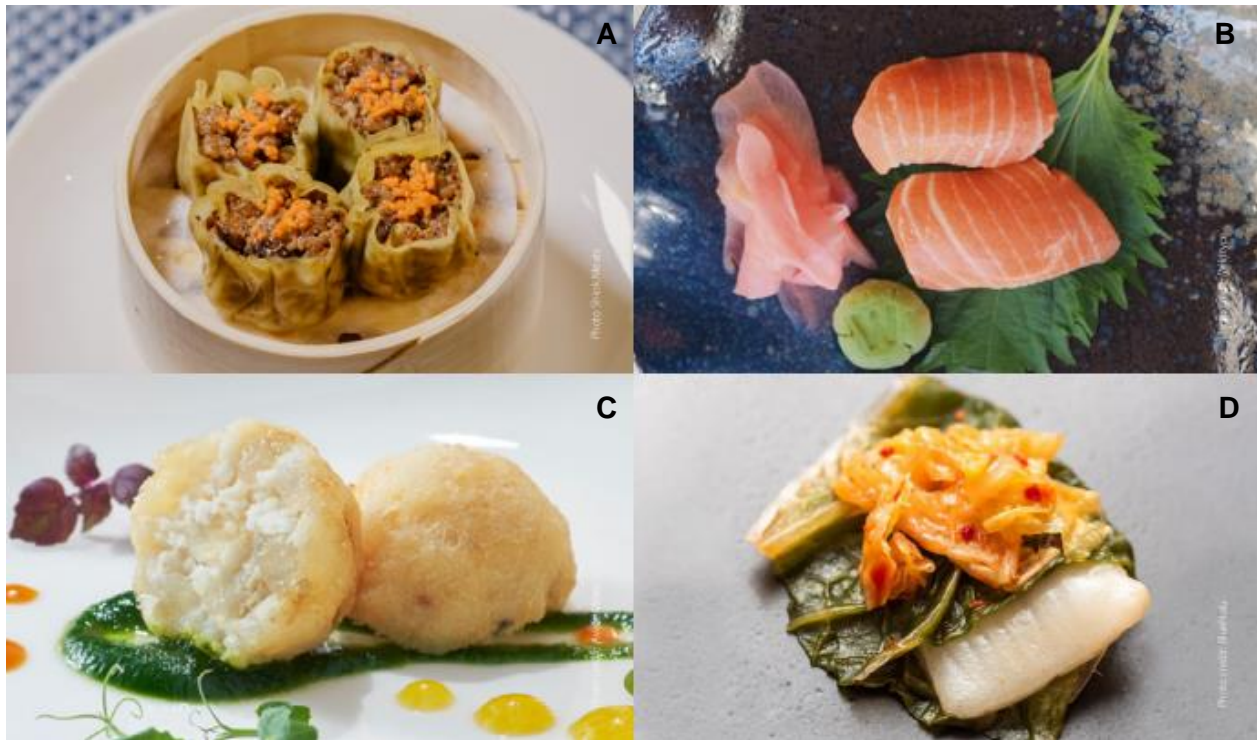


Figure 5. Cell-based seafood preparations. A. shrimp dumplings; B. salmon nigiri; C. fish maw; D. yellowtail. Source: (Marwaha Nisha, Beveridge Malcom 2020).

2.2 Materials for scaffolding design

As stated in the “Aims and Objectives” section, one of the main goals of this project is to fabricate scaffolds using natural and edible materials that could potentially be applied in cell-cultured agriculture. To achieve this, our scaffolds will have two main components: (1) an algae-derived polysaccharide that will provide the primary support and mechanical properties and (2) a conductive filler based on vegetal pigments that possess a chain of conjugated π bonds to increase the conductivity of the material (conductivity of the scaffold is a desirable parameter for developing electroconductive tissues *in vitro* such as muscle tissue). Emphasis has been given to these materials in the sections below.

2.2.1 Synthetic versus natural polymers

In TE, the most widely used synthetic biocompatible polymers are poly(ethylene glycol) (PEG), poly(lactic acid) (PLA) and poly(α -hydroxy acids) as, poly(glycolic acid) (PGA), poly(ϵ -caprolactone) (PCL) and their copolymers (Place *et al.* 2009). In industry, synthetic materials are mostly obtained from petroleum resources, while natural polymers are derived from biological or renewable resources (Soares *et al.* 2018). The increasing demand for petroleum-based raw materials has been threatening the global economy and, most importantly, has been responsible for climate change. Petroleum-derived polymers degradation methods highly contribute to CO₂ emissions, causing global warming and environmental degradation. For this reason, new sources of polymeric materials are strongly required to reduce the current environmental impact of using petroleum-based materials. Considering environmental concerns and the need for a more sustainable future, more and more researchers are looking for green and environmentally friendly materials from naturally available resources. Therefore, new biodegradable natural polymers with low environmental impact are under development, and their applications need to be a part of the systemic approach to biomedicine, TE, and material science. These polymers are mainly composed of non-fossil materials and offer a renewable alternative. They derive from various biological sources such as agricultural products (corn, potato, or soybeans), microorganisms, algae and crustaceans (Soares *et al.* 2018). Wood-derived biopolymers also have attracted great attention due to their versatile properties (Xu *et al.* 2018). The use of protein-based biopolymers for biomedical applications are also under current investigation. Animal proteins such as collagen and gelatine, as well as nano cellulosic biopolymers have been assessed as promising biomedical applications such as drug delivery, wound healing, and tissue implants (Ngwabebhoh and Yildiz 2019). Also, environmentally-friendly cellulose-based products, sericin, fibroin and plant-derived proteins such as soy protein and zein are under development (Mishra *et al.* 2020) (Nagarajan *et al.* 2019). Another emerging eco-friendly source for biomaterials is marine resources. Despite overfishing, climate change, and the increasing ocean pollution with industrial waste, some marine resources remain plentiful and, currently undergoing a renaissance in modern materials science. In 2017, Roberto Nisticò explored the possibility of producing valuable, useful materials from the underutilised shellfish biowaste, namely chitin and its derived by-products (Nisticò 2017). Marine polysaccharides of algal origin also have vast potential as biomaterials

(Khrunyk *et al.* 2020). From the mentioned polymers, only the edible materials fill our purpose of creating a scaffold specific for cell-cultured fish applications. These materials are discussed in the following sections.

2.2.2 Edible materials

Edible scaffolds are needed to answer cell-cultured food demand and provide an animal-free environment for cell growth without associated ethical or environmental concerns. Therefore, the production of vegan scaffolds derived from bio-valorised, low-cost, non-toxic, and biocompatible polymers has emerged as a popular research field. Scaffolds are essential components to increase cell-cultured food scalability, provide structure, and contribute to organoleptic properties (Rubio *et al.* 2020). In this sense, in 2014, a 3D apple based on a cellulose scaffold was manufactured, successfully supporting the *in vitro* 3D culture of NIH3T3 fibroblasts, mouse C2C12 muscle myoblasts and human HeLa epithelial cells (Modulevsky *et al.* 2014). After that, in 2017, Enrione *et al.* developed a 3D scaffold-based on salmon gelatine, alginate, and gelating agents such as agar or agarose (Enrione *et al.* 2017). More recently, Acevedo (2018) and Orellana (2020) used such biomaterials combination to produce edible films for *in vitro* meat production (Acevedo *et al.* 2018; Orellana *et al.* 2020). In 2019, MacQueen *et al.* demonstrated bovine aortic smooth muscle cells and rabbit skeletal muscle myoblasts cultured on edible gelatine fibre scaffolds (MacQueen *et al.* 2019). In 2020, Ben-Arye and colleagues developed an economic and vegan scaffold from textured soy protein, showing that it can support the growth of bovine skeletal muscle cells for a prototype of cell-cultured meat (Ben-Arye *et al.* 2020).

2.2.3 Natural available materials: marine resources

As mentioned above, the oceans have plentiful marine resources and are currently arising in modern materials science. Marine biomaterials are rich sources of structurally diverse compounds with various biological activities, and most of them are underutilised (Pulakkat and Patravale 2020). Seaweeds are a potential feed resource due to their possible large biomass production that does not require agricultural land, fertilizers, or freshwater. Marine polysaccharides of algae origin also have vast potential as biomaterials. Seaweeds are divided into three main classes: green, red, and brown algae containing various polysaccharides such as alginate, agar, carrageenan's, fucoidans and ulvans.

2.3.4 Electrically conductive materials

Conductive materials are essential for the direct electrical stimulation of cells and, specifically, as substrates for producing tissues where electrical conductivity can enhance cell growth. Conducting polymers (CPs) are biocompatible and promote cell adhesion, migration, proliferation, differentiation, and protein secretion at the polymer–tissue interface with or without external electrical stimulations. Biomedical applications of CPs are essentially for biosensors, TE, artificial muscles, and drug delivery. These materials improved cell adhesion and proliferation of different cells such as L929 fibroblasts, C2C12 myoblasts, PC12 cells, RSC96 Schwann cells, H9c2 cardiac cells, primary cardiomyocytes, MC3T3-E1 cells, and

mesenchymal stem cells (Haryanto and Khan 2018). For muscle cells, electrical stimulation contributes to differentiation and increases myofiber diameter, enhances myotube structure, and increases the myofibrillar protein content (Edelman *et al.* 2005; Fraeye *et al.* 2020). Nowadays, polypyrrole (PPy), polyaniline (PANI), polythiophene (PT), and poly(3,4-ethylene dioxythiophene) (PEDOT) are very used since their phenyl or pentyl groups offer excellent thermal stability and conductivity. Usually, scaffolds with CPs are blended with other biomaterials to optimise the mechanical properties. Other non-polymer materials such as metal nanoparticles and ions, inorganic nanoparticles, graphene, carbon nanotubes, graphene oxide, and ionic liquids are also applied to provide electroconductive proprieties to scaffolds (Shi *et al.* 2016). Scaffolds using edible conductive polymers have not been developed, and strategies to manufacture and develop materials from natural conductive polymers such as natural conjugated molecules are currently lacking.

2.3 Hydrogels

Hydrogels are a group of polymeric materials that hold large amounts of water within their 3D structures, due to hydrophilic functional groups in the polymeric backbone, resulting in high hygroscopic structures. Their stability in water is due to the crosslinks established between the network chains (Ahmed 2015). According to the nature of the cross-linking reaction hydrogels can be classified as chemical or physical hydrogel. Covalently crosslinked networks result in chemical hydrogels, while networks that result from physical interactions such as hydrogen bonds, ionic interactions, hydrophobic interactions, or polymer chain entanglements result in physical hydrogels (Pal *et al.* 2009).

Hydrogels are highly biocompatible materials with tuneable characteristics, allowing the design and development of inks and/or scaffolds with tailored properties, such as biodegradation, mechanical stability, and the ability to respond to stimuli. This work aims to fabricate hydrogels scaffolds based on vegan polymers as algae polysaccharides that crosslink due to physical interactions as polymer chain entanglements and ionic interactions. Such hydrogels' mechanical properties (swelling degree, water content, and mechanical stability) will be evaluated. After, natural conjugated π molecules will be added to the hydrogels network as conductive fillers aiming to increase the material's conductivity. The importance of adding electroconductive capacity to our hydrogels is discussed in the next section.

2.3.1 Electroconductive hydrogels

Hydrogels have limiting electroconductive properties that hinder them to mimic the complex electrophysiological microenvironment of specific tissues. To overcome this challenge, electroconductive materials have been used as fillers for hydrogels to potential replicate the electrical and biological characteristics of biological tissues as cardiac, cartilage, muscle, neural, and skin (Rogers *et al.* 2020). Therefore, scaffolds for these tissues must support bioelectrical signalling. Besides, electroconductive hydrogels can be useful for several applications, such as bioconductors, biosensors, electro-stimulated drug delivery, bioactuators, and artificial muscles (Shi *et al.* 2016).

Electrical stimulation enhances myotube structure and increases the myofibrillar protein content in mammals (Fraeye *et al.* 2020). We hypothesised that also fish myoblast, proliferation, maturation, and organisation of myotubes could be accelerated using electrical stimuli. In this work, integration of natural conjugated π molecules in our formulations will be assessed to provide scaffold electroconductive features. As mentioned in sections above, scaffolds using edible conductive molecules have not yet been developed. This work aims to develop a strategy to fabricate electroconductive hydrogels by incorporating natural conjugated π molecules in algae-derived hydrogels.

2.4 Scaffolding fabrication techniques

2.4.1 Overview

Selecting a scaffold fabrication technique is critical since it determines several scaffold properties such as biodegradability, specific surface area, tensile strength, and porosity. Conventional fabrication techniques include solvent casting/particulate leaching, freeze-drying, gas foaming, thermally induced phase separation and electrospinning. On the other hand, there are also advanced techniques like 3D printing, 4D bioprinting, electrohydrodynamic jet printing, and melt electrospinning writing (Ambekar and Kandasubramanian 2019). Since the manufacturing technique selected in this thesis was 3D printing, we will focus on this method in the sections below. The most commonly used 3D bioprinting techniques include inkjet bioprinting, stereolithography, extrusion bioprinting and light assisted bioprinting (Zhu *et al.* 2016; Kyle *et al.* 2017). Additionally, recent methods as freeform reversible embedded hydrogels (FRESH) 3D bioprinting technique that works by extruding the bioink within a bath that serves as a temporary support are being evaluated (Corbett *et al.* 2019; Mirdamadi *et al.* 2020). The same for the process of suspended layer additive manufacture (SLAM) (Senior *et al.* 2019). The 3D printed product should be precise and reproducible.

2.4.2 3D extrusion bioprinting

3D extrusion bioprinting (Figure 6) is the precise deposition of cell-laden bioinks to construct complex and functional tissues. In this technique, pneumatic pressures are applied to a cartridge containing the bioinks (i.e. inks containing cells), which are pushed through a nozzle to be deposited on different locations with high resolutions and shape fidelity (Hockaday *et al.* 2012). The several parameters and conditions that can be controlled on a printing process are: (1) the solution intrinsic properties including polymer type, molecular weight, concentration, viscosity, and surface tension; (2) the required processing conditions as applied air pressure, deposition rate (line speed), nozzle diameter and distance between nozzle and substrate; (3) the environmental conditions as the oxygen concentration in printing environment and temperature. For example, higher polymer concentrations in the ink usually introduce more cross-linking and viscosity.

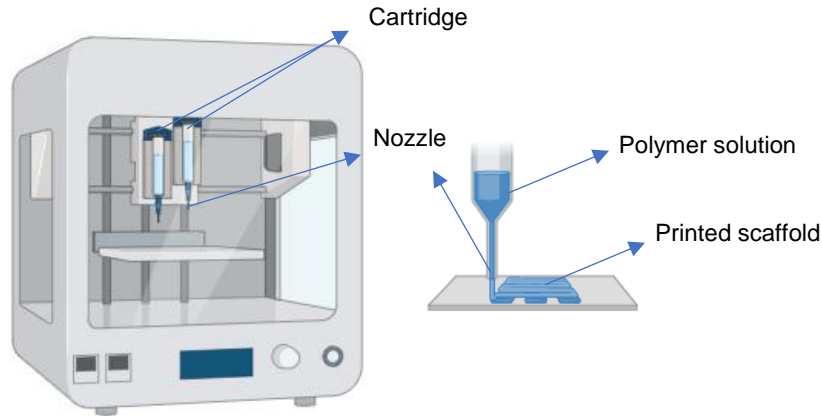


Figure 6. 3D printer scheme. At the right side there is a 3D printer nozzle. (Figure created on BioRender).

However, while solidier polymeric networks result in better printable bioinks, they also result on microenvironments that usually leads to low cell densities. Besides, printability is also dependent on the polymer gelation state. Bioinks with under gelation, proper gelation and over gelation given by their ability to be printable (i.e printability), result in different extrusion patterns and structures (Distler *et al.* 2021). Kyle and colleagues discussed the ideal properties of bioinks and the critical parameters for measuring printability in detail elsewhere (Kyle *et al.* 2017).

Scaffold architecture design and mechanical properties are critical for controlling cell behaviours. 3D microenvironments provide a more physiologically native-like structure to guide cells and enhance their functions. 3D printed scaffolds enable an adequate spread of media, nutrients, and growth factors. Importantly, this technology enables printing cells and scaffolds simultaneously, allowing accurate control of cell distribution, high resolution, scalability and cost-effectiveness (Mandrycky *et al.* 2016). Moreover, bioinks can also be functionalised with cell recognition sequences to enhance physical, chemical, and biological properties.

The 3D printed cell-cultured meat mimics conventional meat structure leading to greater consumer acceptance. 3D printing cell-cultured meat and seafood have many applications such as personalized nutritional treatment, military operations, space missions and public consumption (Liu *et al.* 2017). For example, the military and space missions can produce customized food products based on each soldier's nutrition and diet requirements. Furthermore, NASA has already funded research in 3D food printing (Stephens *et al.* 2018). Moreover, Aleph Farms and 3D Bioprinting Solutions companies have already proved the feasibility of cell-cultured meat in space (Liu *et al.* 2017).

2.5 Cell-material interactions

In TE, cells can be seeded in a 3D scaffold or encapsulated inside a hydrogel material. In both cases the material provides a suitable cellular microenvironment through cell protection and promoting cell-to-material or cell-to-cell adhesions that regulate cell differentiation, metabolic activity, and cell-cell signalling (Sun *et al.* 2006). A scaffold or hydrogel material should mimic the cell native microenvironment formed by the extracellular matrix (ECM). ECM is composed of biochemical components as adhesion proteins, soluble factors, growth factors, GAGs, and signalling molecules. Physical factors as three-dimensionality, mechanical stiffness, surface topography, and electrical signalling also play a vital role in maintaining tissue structure and integrity.

Cell adhesion to the material (cell-to-material interactions), cell-to-cell interactions, and cell orientation are crucial for sustaining tissue properties and functions. Moreover, cells dynamic and organisation of the cytoskeleton are closely associated with adhesion mechanisms. In our work, cell organization and cell-material interactions as adhesion and orientation will be evaluated through two different experiments: (i) cells seeded in 3D printed scaffolds and (ii) cells encapsulated in scaffolds by 3D bioprinting.

Chapter 3. Materials and Methods

3. Materials and Methods

3.1 Ink formulation

The algae-based polysaccharide (AlgP) and the natural conjugated molecules were purchased from Sigma-Aldrich and used without further treatment.

3.1.1 Algae-based polysaccharide solutions

To prepare AlgP solutions, ABP was dissolved in ultrapure water (MilliQ, Millipore, Merck) under continuous stirring in a hotplate (Stuart) at 80°C, until fully dissolved. Solutes for preparation of solutions containing 10 g.L⁻¹, 15 g.L⁻¹, 20 g.L⁻¹, and 25 g.L⁻¹ AlgP were weighted using a bench-scale (Mettler Toledo).

3.1.2 Doping with natural conjugated molecules

Sonication of the solutions was performed using an ultrasonic cleaner (VWR) via an ultrasonic bath induced by high-frequency pressure (sound) waves to agitate a liquid that allowed the natural conjugated molecules particles to disperse through the AlgP solution. The solution with 15 g.L⁻¹ AlgP was selected to be doped with molecule A (molA) and molecule B (molB). Conjugated particles were added directly to the 15 g.L⁻¹ AlgP solution and exposed to an ultrasonic bath for a specific time. The result is a red-coloured ink. To evaluate the maximum concentration possible to disperse, a visual assessment was conducted using different concentrations: 1, 5, 10, and 20 g.L⁻¹ of natural conjugated molecules. The sonication time increased with increasing molecule A and B concentrations, ranging from 30 minutes to 8 hours. The experimental procedure is illustrated in Figure 7.

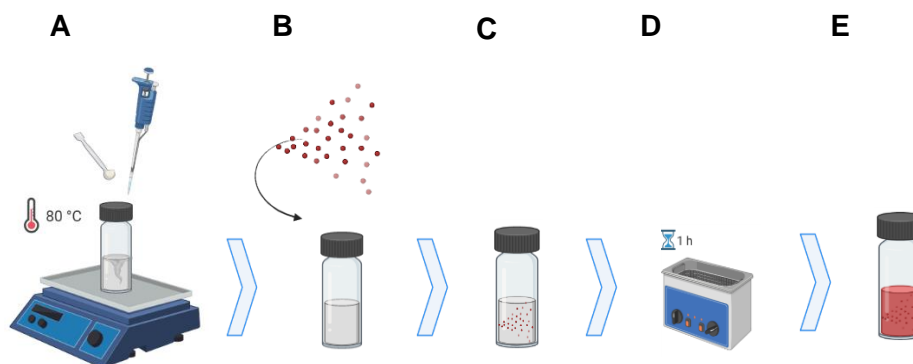


Figure 7. Illustration of the ink formulation procedure. A) Algae-polysaccharide dissolution at 80°C; B) Addition of particles of natural conjugated molecules to the algae-polysaccharide solution; C) Algae polysaccharide doped solution; D) Ultrasonic bath illustration; E) Natural conjugated molecules dispersed in the algae polysaccharide solution via ultrasonic exposure. Image created using BioRender.

3.1.3 Ink nomenclature

To simplify the reader interpretation and to facilitate figures and scheme visualisation, the results associated with the previously formulated inks are in this thesis reported following a specific nomenclature, as defined in Table 1. Data points are associate to a specific colour, for labelling purposes.

Table 1. Inks nomenclature according to the concentrations used during their formulation and respective colour code.

Concentrations (solvent=water)	Nomenclature	Colour
10 g.L ⁻¹ AlgP	10AlgP	
15 g.L ⁻¹ AlgP	15AlgP	
20 g.L ⁻¹ AlgP	20AlgP	
25 g.L ⁻¹ AlgP	25AlgP	
15 g.L ⁻¹ AlgP + 1 g.L ⁻¹ molA	15AlgP_1molA	
15 g.L ⁻¹ AlgP + 5 g.L ⁻¹ molA	15AlgP_5molA	
15 g.L ⁻¹ AlgP + 10 g.L ⁻¹ molA	15AlgP_10molA	
15 g.L ⁻¹ AlgP + 20 g.L ⁻¹ molA	15AlgP_20molA	
15 g.L ⁻¹ AlgP + 1 g.L ⁻¹ molB	15AlgP_1molB	
15 g.L ⁻¹ AlgP + 1 g.L ⁻¹ molB	15AlgP_5molB	
15 g.L ⁻¹ AlgP + 1 g.L ⁻¹ molB	15AlgP_10molB	

3.1.4 Cell culture and passaging

Mouse fibroblasts L929 purchased from Sigma were cultured in Dulbecco's Modified Eagle's Medium (DMEM) supplemented with 10% Fetal Bovine Serum (FBS) and 1% Penicillin/Streptomycin in a 5% CO₂ atmosphere at 37°C using a CO₂ incubator (Sanyo, MCO-19AIC). Sigma provided medium, serum and reagents. Cells were used from passage 10 to 20, with media changed every two days. Cells were harvested from the T-flask when they reached confluence using 2 mL trypsin/ethylenediaminetetraacetic acid (EDTA) solution (Sigma) and collected by 7 minutes centrifugation at 1250 rpm using a Heraeus Megafuge 8 centrifuge (Thermo Scientific). Trypan Blue staining (Thermo Scientific) was performed to determine the cell viability by counting cells on a haemocytometer. Trypan blue stock solution (10µL) was added to 10µL of cells, loaded in the hemacytometer and examined under a microscope (Olympus CKX31 Bright Field). Dilutions were made as appropriate to comply with hemacytometer cell number requirements. Cell viability was calculated as the number of viable cells divided by the total number of cells within the grids on the hemacytometer. Blue-stained cells were considered non-viable. The cell concentration was calculated by the average number of viable cells $\times 10^4 \times 2 \times$ dilution factor (10) = cells/mL culture.

3.1.4.2 Evaluation of formulation ingredients cytotoxicity

Water-soluble tetrazolium salt (WST-8) viability assay was performed to evaluate the toxicity of the scaffold's components (AlgP, molA and molB) in culture medium using a Cell Counting Kit-8 (CCK-8) from Sigma-Aldrich. A dilution of CCK-8 1:10 in DMEM was used.

L929 cells were suspended following the protocol in the above section, and cell viability (96.12%) using the Trypan Blue protocol was assessed. Cells were plated at a concentration of 100 000 cells/mL 24-48 h before the viability experiment in a 96-Well plate. To evaluate the biomaterials cyto-toxicity, AlgP, molA and molB 1g.L⁻¹ solutions were sterile-filtered, and 10 µL of the different solutions were added to 200 µL of cell culture media. Cells grown in plain DMEM served as the positive control, and Triton-X was used as the negative control. Each culture condition was performed in triplicate (n=3). All samples were incubated in 10 µL CCK-8 solution and DMEM for 1 h and 24 h at 37 °C. Once the incubation was completed, the supernatants were transferred to a new 96-well plate. The absorbance at 450 nm (optical density; OD) was measured using a Plate Reader Infinite® 200 PRO (TECAN) to assess the conversion of WST-8 into formazan as an indicator for cell viability.

3.2 Ink characterisation

3.2.1 UV-Visible spectra

To confirm the presence of molA and molB in the formulated inks, a Plate Reader Infinite® 200 PRO (TECAN) was used to measure the absorbance of the following inks: 15AlgP, 15AlgP_1molA, 15AlgP_5molA, 15AlgP_10molA, 15AlgP_1molB, 15AlgP_5molB, and 15AlgP_10molB. From the previous

experiment's observations, a peak wavelength was selected, and the molA and molB inks were also scanned at 560 nm (Annex 1).

3.2.2 Rheological Assessment

The rheological properties of the inks were determined using an MCR 92 modular compact rheometer (Anton Paar). The rheological assessment was conducted using a cone-plate geometry with a cone diameter of 50 mm, and a constant measurement gap of 0.1 mm, resulting in a sample volume of 0.5 mL. The instrument was calibrated to analyse the viscoelastic region.

To estimate the sol-gel transition temperature and cross-linking behaviour of the 15AlgP ink temperature sweeps were performed. The viscosity was determined at a shear rate of 50 s^{-1} with temperatures varying from 37 to 20 °C (cooling). The assay ran over 300 s with a rate of $0.2 \text{ }^{\circ}\text{C}\cdot\text{s}^{-1}$. The temperature range was selected considering the value of 37°C for the CO₂ incubator and of RT for the printer setup operations. To further evaluate the changes in the polymer framework after the addition of natural conjugated molecules, 15AlgP_5molA ink was also tested. Each ink measurement was performed in triplicate (n=3).

After, the elastic and viscous behaviour of the materials were characterised by recording the storage modulus (G'), and the loss modulus (G'') as a function of time under an oscillating time sweep test with a frequency of 1 Hz and temperature of 25 °C, for ten minutes. The time dependence of G' and G'' was evaluated for the following inks: 15AlgP, 15AlgP_1molA, 15AlgP_5molA, 15AlgP_10molA, 15AlgP_1molB and 15AlgP_5molB. The gelation time corresponds to the time where G'' intersects G' . Each ink measurement was performed in triplicate (n=3).

3.3 Scaffold characterisation

Scaffold characterisation techniques were performed to evaluate the proprieties of the solidified hydrogels.

3.3.1 Casting hydrogels on moulds

Cylindrical moulds with 9 mm diameter and 4-8 mm in height were used as support to cast hydrogels. The height was varied depending on the requirements of the characterisation techniques. These moulds were home-made by fused deposit modelling using a Prusa i3 MK3S 3D extruder loaded with an PLA filament. As shown in Figure 8, the process started with empty moulds that acted as a support structure until gelation occurred. To summarise the process, the moulds were filled with the desired solution volume, the gel was formed, and the mould was carefully removed with tweezers. All the formulated inks (Table 1) were used to cast hydrogels except for 15AlgP_20molA.

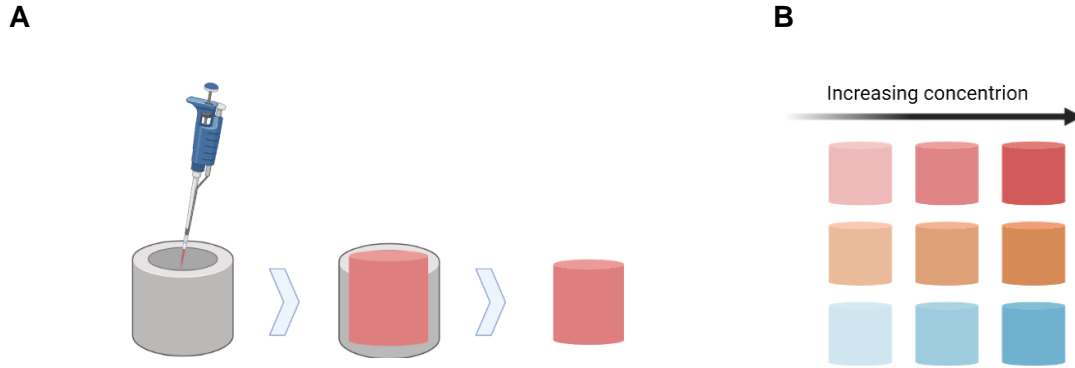


Figure 8. A) The process of casting hydrogels using moulds. The process started with empty moulds that acted as a support structure until gelation occurred. After that, the mould was removed, and the solid hydrogel remained. 3D printed cylindrical moulds with 9 mm diameter and 4-8 mm in height were used as support to cast hydrogels. B) This process was performed for all formulate inks. Higher concentrations resulted in stronger colours. Image created using BioRender.

3.3.2 Mechanical evaluation

3.3.2.1 Compression tests

A uniaxial compression test was performed using a Univert (CellScale Biomaterials Testing) load frame with a 10 N load cell. Hydrogels casted on the moulds were used for this assay, specimens were cylindrical (4-6 mm of diameter and 4 mm of height, $n = 5$), and the crosshead speed was set constant displacement rate at 3 mm min^{-1} during the test. Stress-strain curves were obtained considering Eq. 1 and Eq. 2. Young's modulus (Eq. 3) was calculated from the stress-strain curve's 0–15% linear strain region. The mechanical properties were evaluated for the following inks: 15AlgP, 15AlgP_1molA, 15AlgP_5molA, and 15AlgP_10molA.

$$\text{Stress} = \sigma = \frac{F}{A} \quad \text{Eq. (1)}$$

Where F (Newton, N) is applied force, and A (mm^2) is cross-area.

$$\text{Strain} = \varepsilon = \frac{\Delta L}{L_0} \quad \text{Eq. (2)}$$

Where ΔL (mm) is displacement and L_0 (mm) is initial height.

$$\text{Young's Modulus} = \frac{\sigma}{\varepsilon} \quad \text{Eq. (3)}$$

where σ (Nmm⁻²) is stress and ϵ (non-dimensional) is strain. Since 1 Nmm⁻² = 10⁶ Pascal (Pa) = 1000 kPa conversions were performed to discuss the Young's Modulus in kPa units.

3.3.3 Chemical and physical characterisation

3.3.3.1 Scaffold Water Uptake Evaluation (Swelling degree)

Hydrogels with 10AlgP, 15AlgP, 20AlgP, and 20AlgP were prepared and placed in a Falcon® 12-well plate to soak in PBS at RT for seven days. Measurements of swollen hydrogel weight were taken after preparation and subsequently on days three, five, seven. An additional time point at day forty was taken for long-term swelling observations. To measure the of swelling (%) of the hydrogels, the PBS excess was carefully removed with filter paper, and the samples were weighed to obtain the initial sample mass (W_o). For each measurement, hydrogels were removed from the well plate, PBS excess was wiped using filter paper, and the hydrogels were weighed (W_s). Swelling (%) of various AlgP concentrations was performed in triplicate to minimise error and reported as a mean value (n=3). The swelling degree was then calculated with Eq. 4:

$$\text{Swelling (\%)} = \frac{(W_s - W_o)}{W_o} \times 100 \quad \text{Eq. (4)}$$

where W_o is the initial weight of the hydrogel and W_s is the weight of the swollen hydrogel.

3.3.3.2 Water content evaluation

Hydrogels 15AlgP, 20AlgP, and 15AlgP were prepared and placed in a 12-well plate (Falcon®). To evaluate the hydrogels water content, samples were weighed to obtain the initial sample mass (W_o). To obtain dry weight (W_d), samples were vacuum dried at RT. The water content (%) is estimated according to Eq. 5:

$$\text{Water Content (\%)} = \frac{(W_o - W_d)}{W_o} \times 100 \quad \text{Eq. (5)}$$

where W_o is the initial weight of the hydrogel and W_d is the weight of the dried hydrogel.

Equation 5 was also applied for hydrogels 15AlgP_1molA, 15AlgP_5molA, and 15AlgP_10molA. For these samples, instead of using vacuum, the drying was performed with constant heat exposure in an incubator at 43.5°C.

3.3.4 Surface proprieties

3.3.4.1 Evaluation of the surface wettability

Contact angle (θ) is the angle formed between the surface of the solid and the tangent to the liquid/air interface at the three-phase boundary. This angle was measured for the moulded hydrogels in

contact with a glycerol drop, namely 15AlgP, 15AlgP_5molA, and 15AlgP5molB, at RT. A syringe was used to place the drops of glycerol on the top of the hydrogels. The sessile/captive drop profile method was used, and the contact angle was assessed with the Kruss DSA25B apparatus and Drop Shape Analysis (DSA) 4 Software by measuring the tangent angle at the three-phase contact point. DSA is an image analysis method for determining the contact angle from the shadow image of a drop. It directly measures the surface wettability (i.e., the capability of a liquid to spread across a material's surface) (Figure 9) using the Young-Laplace fitting method through Eq. 6:

$$Y_{S/L} = Y_{S/A} + Y_{L/A} \cos(\theta) \quad \text{Eq. (6)}$$

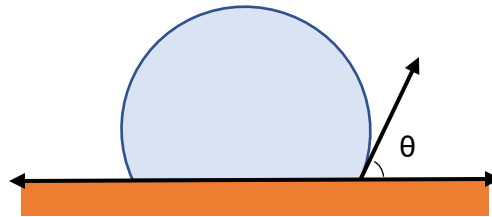


Figure 9. Illustration of the material surface-drop interaction with the Young's contact angle shown used the Young-Laplace fitting method.

Where $Y_{S/L}$, $Y_{S/A}$, $Y_{L/A}$ and represents the solid-liquid, solid-air, and liquid-air interfacial surface tensions, and θ is Young's contact angle.

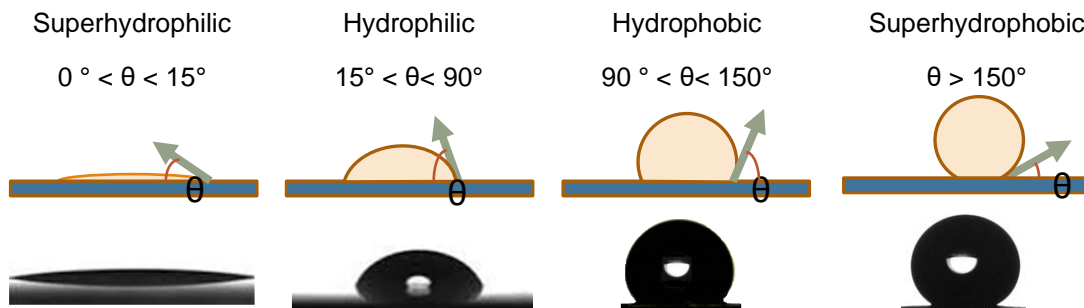


Figure 10. Illustration of the surface-drop behaviour obtained for materials with different wettability. Superhydrophilic surfaces show a Young's contact angle between 0 and 15, hydrophilic surfaces between 15 and 90, hydrophobic surfaces between 90 and 150, and superhydrophobic surfaces above 150.

3.3.4.2 Scanning Electron Microscopy (SEM)

The hydrogel morphology was evaluated by SEM using an analytic JEOL JSM7001F FEG-SEM (Jeol, Akishima, Tokyo, Japan) at 10 kV. This analysis was conducted under vacuum and thus required water phase removal from the hydrogel before imaging. The scaffolds were dried using treatment with hexamethyldisilane (HMDS) and ethanol as dehydration solvents as an alternative to critical point drying. Each hydrogel was dried following the steps represented in Figure 11. Samples were immersed for 20 min between each step and then air-dried overnight.

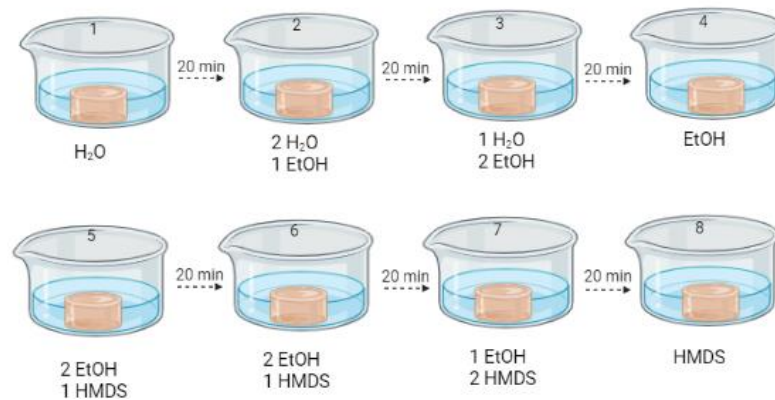


Figure 11. Illustration of the hydrogels drying process using treatment with hexamethyldisilane (HMDS) and ethanol as dehydration solvents. The process was divided in 8 steps. Between each step were waited 20 minutes. The mixtures used are indicated below each illustration. Image created using BioRender.

Before imaging, samples were coated with a thin layer of gold-palladium. Samples were imaged at several magnifications. SEM pictures were analysed using NIH ImageJ software (National Institute of Health, MD, USA).

3.3.5 Electrical properties

3.3.5.1 Electrochemical Impedance Spectroscopy

Electrochemical impedance spectroscopy (EIS) can be resolved into real (Z') and imaginary (Z'') parts. The impedance of the dielectric material is ultimately two components, resistive part, and capacitive part.

The Bode plot represents the magnitude of impedance $|Z|$ as a function of frequency or the phase angle θ as a function of frequency. The Nyquist plot is another commonly representation of the complex impedance behaviour. The Z'' is plotted as a function of the impedance's Z' for a range of frequencies.

The amplitude of the alternating current (AC) electric signal applied to the samples was 10 mV. The conductivity was obtained from the value of solution resistance (R_s) extracted from Zview 4 software using Eq. 7:

$$\text{Conductivity} = \frac{t}{R_s \times A} \quad \text{Eq. (7)}$$

Where t is the thickness of the hydrogel in millimetres, R_s is the solution resistance, and A is the contact area in a square millimetre.

EIS was performed on a Squidstat Plus potentiostat (Admiral Instruments) interfaced with a personal computer, including the Squidstat user interface software. Briefly, 8.9 mm diameter cylindrical hydrogels with 3.8 mm thickness were sandwiched between two homemade stainless-steel electrodes in a two-electrode configuration at RT. The experiment parameters followed are resumed in Table 2. Frequencies ranging from 0.1 to 100,000 Hz were applied. Residual water on the surface of the hydrogels was removed with filter paper before each experiment. For this, 15AlgP, 15AlgP_1molA, 15AlgP_5molA, and 15AlgP_10molA were tested. Each measurement was performed in triplicate ($n=3$).

Table 2. Electrochemical impedance spectroscopy experimental parameters.

<u>Parameter</u>	<u>Value</u>
Quiet time	5 s
Starting frequency	100 000 Hz
Ending frequency	0.1 Hz
Steps per decade	5
DC bias	0.1 V, in respect to a reference
AC excitation amplitude	10 mV

3.3.5.2 Four-probe method

To perform electroconductivity measurements, the hydrogels were dried entirely at RT. Dried hydrogels were coated with four equally distanced 50 nm thick gold strips to improve electrical contact by physical vapour deposition using an Edwards E306A thermal evaporator. The electroconductivity was measured using the four-probe technique with a probe station coupled to a Keithley 2400 Source meter unit. The conductivity of each dried hydrogel was measured in 4 different spots, and electroconductivity was averaged from 3 mats. For this, the following hydrogels were tested: 15AlgP, 15AlgP_1molA, 15AlgP_5molA, 15AlgP_10molA, 15AlgP_1molB, 15AlgP_5molB, and 15AlgP_10molB were tested. The thickness of the mats was measured using a digital micrometre head IP54 0-25 mm spherical (Filleta).

3.3.5.3 Cyclic voltammetry

Cyclic voltammetry was performed in an Electrochemical Analyzer (CH Instruments) with a boxed connector DSC4MM for screen-printed electrodes (Metrohm DropSens) interfaced with a personal computer. Hydrogels were prepared and placed with a spatula on a disposable screen-printed carbon electrode C11L (Metrohm DropSens) to perform the measurement. The working and auxiliary electrodes were made of carbon, and a silver/silver chloride (Ag/AgCl) electrode was used as the reference electrode. Potentials were applied from 0.8 to -1.5 V at different scan rates: 0.01, 0.02, 0.04, 0.06, 0.08, 0.1, 0.2, 0.3, and 0.4 V. s^{-1} . PBS solution was used as supporting electrolyte. For this, the following hydrogels were tested: 15AlgP, 15AlgP_1molA, 15AlgP_5molA, 15AlgP_10molA, 15AlgP_1molB, 15AlgP_5molB, and 15AlgP_10molB. Each measurement was performed in triplicate ($n=3$).

3.3.5.4 LED light test

The ability of the hydrogels to act as functional electronic parts was evaluated by connecting them to a light-emitting diode (LED). The current was provided using an Arbitrary/Function Generator AFG1000 (Tektronix) providing 4 V. The LED lamp metal was used as the positive control, and the air was used as the negative control. This experiment was performed using the hydrogel 15AlgP_5molA.

3.4 3D Printing

The 3D printer used was an F4200N.2 Compact Benchtop Robot from Fisnar aided by a DC100 High Precision Dispenser. The syringe barrels, syringe barrel adaptor, end caps, pistons and dispensing tips were also from Fisnar. The digital model was uploaded to the robot using the Fisnar RobotEdit software. Parameters as printing speed, the applied pressure, and the distance between layers were modified to find the optimal printing conditions.

3.4.1 Exploring different architectures

Different structures and morphologies were fabricated at optimised printing conditions, including structures consisting of filled circles ($r = 4$ mm), empty circles ($r = 6$ mm), squares (10 mm x 10 mm), films (4 mm x 4 mm), and squared meshes (10 mm x 10 mm) with a different number of layers varying from 3 to 100 layers of each material.

3.4.3 3D multi-layer structures

Multi-layer constructs were manufactured intercalating layers of the 9AlgP ink with 15AlgP_1molA or 15AlgP_5molA inks. Structures with seven layers (4 layers of a 15AlgP doped ink intercalated with 3 layers of 9AlgP ink) were fabricated. Four distinct designs were created (Figure 12). The structures represented on Figures 12A and 12B were 3D printed. To fabricate Figure 12A, thin circles of each material were initially printed and crosslinked. After crosslinking, the different layers were mounted on top of each

other with a spatula. The same procedure was performed to fabricate Figure 12B but with thin films. The dimensions of the structures were circles with $r = 4$ mm and films with 4 mm x 4 mm.

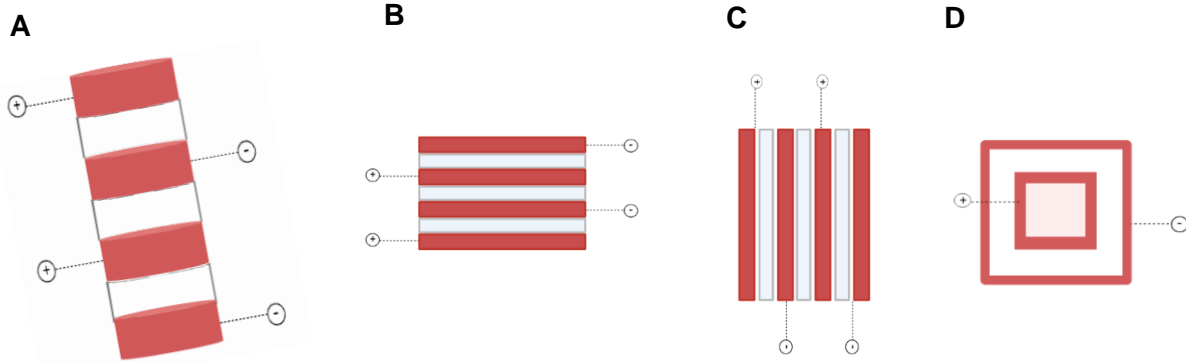


Figure 12. Designs of different multi-layered structures to conjugate bioprinting with the enhancement of the electrical performance of the hydrogel. The constructs were manufactured intercalating layers of the 9AlgP ink and the 15AlgP_1molA or 15AlgP_5molA inks. A) circles ($r = 4$ mm) of intercalated inks; B) films of intercalated inks; C) parallel struts of intercalated inks; D) A large square surrounded by two squares of intercalated ink. Legend: white structures represent the 9AlgP ink and red structures represent the 15AlgP_1molA or 15AlgP_5molA inks; positive (+) and negative (-) symbols represent possible places for electrical current connection to induce structure polarization.

3.4.2 Printability evaluation

3.4.2.1 Printability factor

To estimate inks printability is necessary to introduce the concept of circularity of an enclosed area (A), within a given perimeter (L), which is defined by Eq. 8:

$$C = \frac{4\pi A}{L^2} \quad \text{Eq. (8)}$$

Printability of the inks to achieve square-shaped pores was quantified from microscopy images taken with a Leica DMI3000B (Leica Microsystems). Printability factor (Pr) was estimated as described elsewhere (Distler *et al.* 2021), based on the ratio of the theoretical (C') to the experimental (C) circularity. For a square shape, C' is equal to $\frac{\pi}{4}$. Therefore, Pr was measured considering the pore perimeter (L) and the pore area (A) using Eq. 9:

$$Pr = \frac{\pi}{4} \cdot \frac{1}{C} = \frac{L^2}{16A} \quad \text{Eq. (9)}$$

A perfect gelled ink that originates ideal square-shaped pores corresponds to $Pr=1$, where $Pr < 1$ corresponds to under-gelled inks and rounded pore corners, and $Pr > 1$ to over-gelled inks.

The following inks were evaluated for printability: 10AlgP, 15AlgP, 20AlgP, 15AlgP_1molA, 15AlgP_5molA, 15AlgP_10molA, 15AlgP_1molB, and 15AlgP_5molB. Ink 15AlgP_10molB was not evaluated for printability. The 3D printed scaffolds exhibited a squared-mesh structure with the side dimensions of $10 \times 10 \text{ mm}^2$ and 1-3 layers printed in height, with 0.05 mm distance between layers. A 20-gauge (pink needle; inner diameter 0.5 mm) or a 23-gauge (orange needle; inner diameter 0.6 mm) QuantX™ blunt end dispense tips (Fisnar) were used at a printing speed of 25 mm s^{-1} . The applied pressure and the needle used during printing varied for each ink (see Table 3). To determine the Pr values, the optical images of printed constructs were analysed in ImageJ software to determine the perimeter and area of interconnected channels ($n = 5$).

Table 3. Pressure (psi) applied during printing and respective needle used for each ink. (Pink needle = 0.5 mm; orange needle = 0.6 mm)

<u>Ink</u>	<u>Pressure (psi)</u>	<u>Needle</u>
10AlgP	0.2-1	pink
15AlgP	2-4	pink
20AlgP	15-20	orange
15AlgP_1molA	1.5-4	pink
15AlgP_5molA	2.5-4-5	pink
15AlgP_10molA	2-4	orange
15AlgP_1molB	2	pink
15AlgP_5molB	2-4	pink

3.4.2.2 Line thickness

A line thickness evaluation was conducted to determine how thick the printed strands are compared to a theoretically expected thickness. The theoretical thickness can be estimated by the measure of the inner needle diameter. A 20-gauge (pink needle; inner diameter of 0.5 mm) QuantX™ blunt end dispense tip (Fisnar) was used. Therefore, the theoretical thickness factor is 0.5 mm, and values above or below indicate variations in the printed line thickness. This factor varies with printing parameters as applied pressure and the number of printed layers. The scaffolds used to calculate the thickness factor were the same as before.

3.5. Cell seeding onto 3D scaffolds

For cell seeding experiments, films of the different materials were manufactured with the side dimensions of 10 mm × 10 mm and three layers were printed in height. A 20-gauge (inner diameter 0.5 mm) QuantX™ blunt end dispense tip (Fisnar) and a printing speed of 25 mm s⁻¹ were used. The overall process of printing, cell seeding, and cell characterisation is illustrated in Figure 13. The obtained scaffolds were placed in a 12-well plate and were sterilized with 1% (v/v) anti-anti solution in PBS overnight. The cell seeding was performed with L929 fibroblast cells dropwise using 50,000 cells in 15 µL Dulbecco's modified Eagle's medium (DMEM, Sigma) per each scaffold. Structures were incubated for 1 h inside the laminar flow cabinet after seeding to promote initial cell attachment before adding DMEM until covering the whole scaffold. Subsequently, the well-plate was placed in an incubator (37 °C, 5% CO₂). The medium (supplemented with FBS) was changed every 2–3 days for 8 days. After cells seeding onto the scaffolds, AlamarBlue™ (see section 4.5.1.1) was performed at different cell culture time points (to access cell proliferation capability). Live/Dead staining via calcein-AM/ethidium homodimer-1 staining (see section 4.5.1.2) and a Hoechst-Phalloidin staining (see section 4.5.1.3) were used at the end of the culture to measure cell viability and to elucidate the cells cytoskeleton organization, respectively.

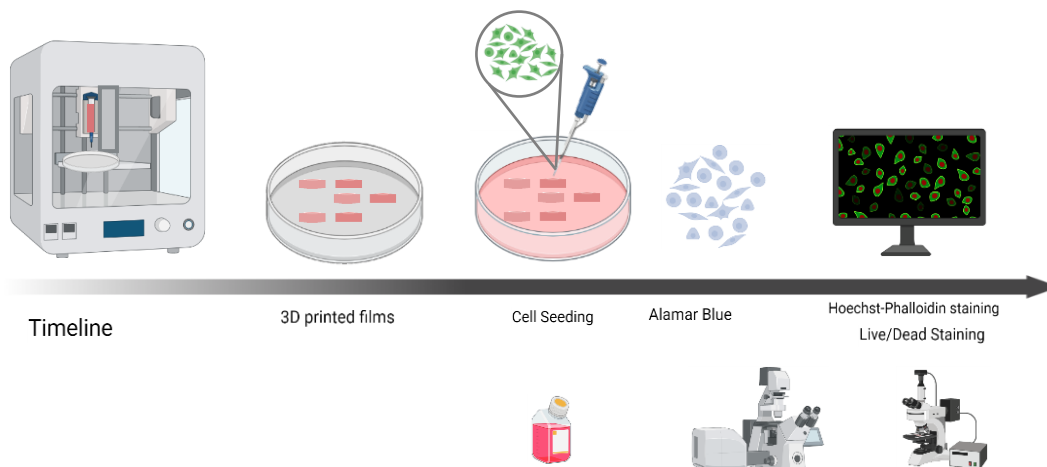


Figure 13. Illustration of the 3D printing process and following seeding experiment. 3D printed films (4 mm x 4mm) were fabricated directly into a petri dish using a printer at RT. After that, 50 000 mouse fibroblast cells were seeded in each film. DMEM (pink bottle) was added to the petri dish until the films were fully covered. The films were incubated for 8 days. Alamar Blue proliferation assay (at day 2 and day 7), Hoechst/Phalloidin staining (at day 5), and Live/Dead (at day 8) staining were performed. Image created using BioRender.

3.5.1 Alamar Blue

Cellular proliferation was assessed using Alamar Blue™ Cell Viability Reagent (Thermo Fisher Scientific) on days 2 and 7 after seeding (50,000 cells/film) to get an indirect estimate of cell number in the 3D printed films. The AlamarBlue™ reagent is reduced at the oxygen level in the electron transport chain, and the

readout is proportional to the cell number (Ansar Ahmed *et al.* 1994; Goegan *et al.* 1995; Nociari *et al.* 1998) AlamarBlue™ reagent (100 µl) was added to the medium of the wells. The plate was covered with aluminium foil, then incubated for 2h in the CO₂ incubator. Then 100 µl aliquots were removed to estimate the reduced AlamarBlue™ by measuring fluorescence at a wavelength of 590 nm after excitation at 560 nm using a Plate Reader Infinite® 200 PRO (TECAN).

3.5.2 Live/Dead viability assay via calcein-AM/ethidium homodimer-1 staining

A Live/Dead viability (Thermo Fisher Scientific) assay using calcein-AM and Ethidium homodimer-1 staining was performed to assess the viability of the seeded cells. After 8 days of culture, each sample was stained with 4-mmol/L green-fluorescent calcein-AM and 2-mmol/L red-fluorescent ethidium homodimer-1 (Molecular Probes, Invitrogen) in sterile PBS solution, covered by aluminium foil and incubated for 30 minutes. The scaffolds were examined for cell viability and cytotoxicity using a fluorescent microscope, Leica DMI3000B (Leica Microsystems), with a green fluorescent protein (GFP) filter and Texas Red (TxRed) filter to visualise living and dead cells, respectively. Three representative images were obtained for each structure. The resulting images were used to perform live and dead cells quantification via ImageJ software.

3.5.3 Hoechst-Phalloidin staining

Hoechst-Phalloidin staining of L929 fibroblasts was performed by fixing cells in 4% formaldehyde (Sigma) in PBS for 30 minutes at RT. Washed three times with PBS and permeabilised with 0.01% Triton-X 100 (Sigma) in PBS for 8 minutes. After being washed three times with PBS, the scaffolds were ready for staining. Nucleus staining was performed using a 5 µg.mL⁻¹ Hoechst 33342 (Thermo Fisher Scientific) nucleic acid stain that emits blue fluorescence when bound to dsDNA solution in PBS for 10 minutes at 37°C. Scaffolds were rewashed in PBS, and the Alexa Fluor 488® (Thermo Fisher Scientific) phalloidin probe with high affinity to cytoskeleton filamentous actin (F-actin) conjugated to a green-fluorescent dye was applied for 30 minutes at RT. A final washing step was performed before fluorescence microscopy imaging.

3.6 3D Bioprinting

For 3D bioprinting experiments, circles of the different materials were manufactured with a radius (r) of 4 mm and three layers were printed in height. A 23-gauge (inner diameter 0.6 mm) QuantX™ blunt end dispense tip (Fisnar) and a printing speed of 25 mm s⁻¹ were used.

The overall process of printing, including cell characterisation, is illustrated in Figure 14. The bioinks solvent was Media 3, but the scaffolds were immersed in DMEM (Sigma) after printing. Subsequently, the

bioprinted rings were placed in an incubator (37 °C, 5% CO₂) for 8 days. The medium (supplemented with FBS) was changed every 2–3 days.

After the 3D bioprinting processes, microscope observations and Live/Dead staining via calcein-AM/ethidium homodimer-1 staining (see section 4.6.2) to measure cell viability were performed.

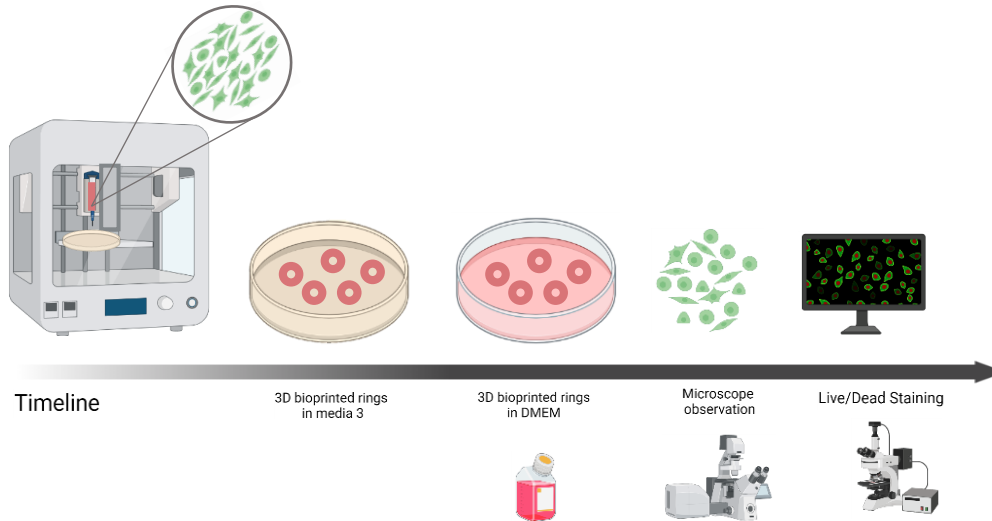


Figure 14. Illustration of the 3D bioprinting process. 3D bioprinted circles ($r = 4$ mm) were fabricated directly into a petri dish using a printer at RT. After printing, DMEM (pink bottle) was added to the petri dish until the circles were fully covered. The films were incubated for 8 days. Microscope observations and Live/Dead (at day 8) staining were performed. Image created using BioRender.

3.6.1 Bioprinting media optimization

3.6.1.1 Bioink formulation

To formulate the bioinks, the same experimental procedure from section 3.1 was used. However, instead of using ultrapure water (MilliQ, Millipore, Merck), the materials were dissolved in DMEM, and customised solutions labelled as Media 1, 2, and 3. Different concentrations of AlgP ranging from 5g.L⁻¹ to 10 g.L⁻¹ were formulated.

To assess the biocompatibility of the solutions. Solutions were sterile-filtered and incubated with L929 fibroblasts to perform a WST-8 assay (described in the section 3.1.4.2). In this case, solutions were incubated for 30, 60 and 120 minutes. DMEM was used as positive control and Triton-X as the negative control. Measurements were performed in triplicate ($n=3$).

3.6.2 Bioprinting process

The bioprinting process was performed using the same instrument described in previous sections. Cells were suspended using the previous protocols to reach a suspension of 3 400 000 cells/mL for bioprinting. 500 μ L of cell suspension was incorporated into the 15AlgP and into the 15AlgP doped bioinks mixing thoroughly to reach a final concentration of 50.000 cells per mL of bioink. A ring structure with a radius of 4 mm was printed using the bioink and three layers were printed in height, the distance between layers was 0.05 mm, the printing pressure was 8-10 psi, and the printing speed was set at 25 mm.s⁻¹. A 23-gauge needle was used. The scaffolds were printed to culture plates (Falcon) and incubated in a 5 mL culture medium (10% FBS (Sigma) and 1% penicillin-streptomycin (Sigma) in DMEM. The medium was changed every 2–3 days for 11 days. After 8 days of culture, the bioprinted scaffolds were evaluated for cell viability using a Live/Dead staining procedure described in previous sections.

3.7 Statistical analysis

All data are presented as mean values \pm standard deviations. Each experiment was conducted in triplicate (n = 3) unless stated otherwise. Statistical significance was performed using t-student tests (GraphPad Prism 9).

Chapter 4. Results and Discussion

4. Results and Discussion

4.1 Ink formulation

4.1.1 Optimizing Algae-based polysaccharide ink concentration

To optimize the AlgP concentration on the inks, four inks with different AlgP concentrations were prepared (10 g.L⁻¹, 15 g.L⁻¹, 20 g.L⁻¹, and 25 g.L⁻¹). From those inks, we chose to work with inks made of 15 g.L⁻¹ AlgP. Through visual observation, we decided to discard the ink with 10 g.L⁻¹, 20 g.L⁻¹, and 25 g.L⁻¹ AlgP. The inks with 10 g.L⁻¹ were near the liquid state, which could provide difficulties during the gelation process. The inks with 20 g.L⁻¹ and 25 g.L⁻¹ were discarded since they reached a highly viscous state (near the solid state) and cannot be manipulated. However, the solution with 15 g.L⁻¹ AlgP was in an intermediate state that allowed manipulating the transition between the liquid and solid behaviour of the ink. Therefore, the 15AlgP ink was used as the primary ink for further procedures and chose to be doped with natural conjugated molecules.

4.1.2 Doping: dispersion of natural conjugated molecules

Molecule A (molA) and molecule B (molB) were selected for this work due to their molecular structure and natural availability. These molecules are conjugated molecules, and we hypothesise they can enhance the electric properties of our inks due to the presence of conjugated π double bonds in which charges can move quickly by doping mechanism. However, molA and molB are not water-soluble compounds, and such characteristics proved to formulate such inks challenging. Intermediate steps were performed and evaluated to efficiently optimise natural conjugated molecules interaction with the AlgP solutions (see Table 4 for more detailed information). For that, four alternative methods were analysed: stirring, emulsions, organic solvents, and ultrasounds. The water-emulsions system was not pursued due to its complexity, and the use of organic solvents is out of this project's scope due to sustainability and edibility concerns. Finally, contrary to stirring, the use of ultrasounds was effective in dispersing both natural conjugated molecules. Hence, the ultrasound method was selected and studied in more detail.

Table 4. List of the methods available to disperse the natural conjugated molecules within the algae-polysaccharide ink. Stirring, emulsions, organic solvents, and ultrasound were considered. A brief description and feasibility output of each method is described.

Methods available	Description	Output
1. Stirring	Dissolve natural conjugated molecules through stirring directly on the AlgP water solution until dissolved.	Natural conjugated molecules do not dissolve with stirring

2. Emulsions	Water-emulsion system that allows suspensions of natural conjugated molecules in edible fats like vegetable oils inside the AlgP water solution	This method was not evaluated due to its complexity
3. Organic Solvents	Dissolve natural conjugated molecules in organic solvents and mixing them with the AlgP water solution	Natural conjugated molecules dissolve in a few organic solvents
4. Ultrasound	Disperse natural conjugated molecules directly on the AlgP water solutions via ultrasounds	This method was effective in dispersing natural conjugated molecules

To evaluate the maximum molecule concentration possible to disperse in the 15AlgP ink, an experiment was conducted using different concentrations: 1, 5, 10, and 20 g.L⁻¹ of molA or molB. The molecules particles were added to the 15AlgP solution and submitted to an ultrasonic bath for different times according with molecule concentration. In Figure 15 is represented the ultrasonic bath step duration versus the molecule concentration for each solution. The ultrasound power was stopped when there was no visual evidence of particles in suspension. From Figure 15, it was possible to confirm that higher concentrations implied longer exposition to ultrasounds to achieve dispersion than for lower concentrations. Also, we concluded that molB particles disperse quicker than molA particles. This outcome was predicted when adding the molecule B powder to the 15AlgP ink (Figure 15), as the data in Figure 15 clearly show that without ultrasound induced dispersion, the molB inks have more dispersibility in the 15AlgP ink than the molA inks. In fact, we observed during ink formulation that molB was more in a powder format than molA that presented more solid small particles. We hypothesise that this could also had impacted dispersibility. Solutions with 20 g.L⁻¹ concentrations are not represented in Figure 15 because we were not able to disperse particles at such a high concentration at the conditions used. For this reason, in further experiments the inks used were 15AlgP_1molA, 15AlgP_5molA 5, 15AlgP_10molA, and 15AlgP_1molB, 15AlgP_5molB, and 15AlgP_10molB.

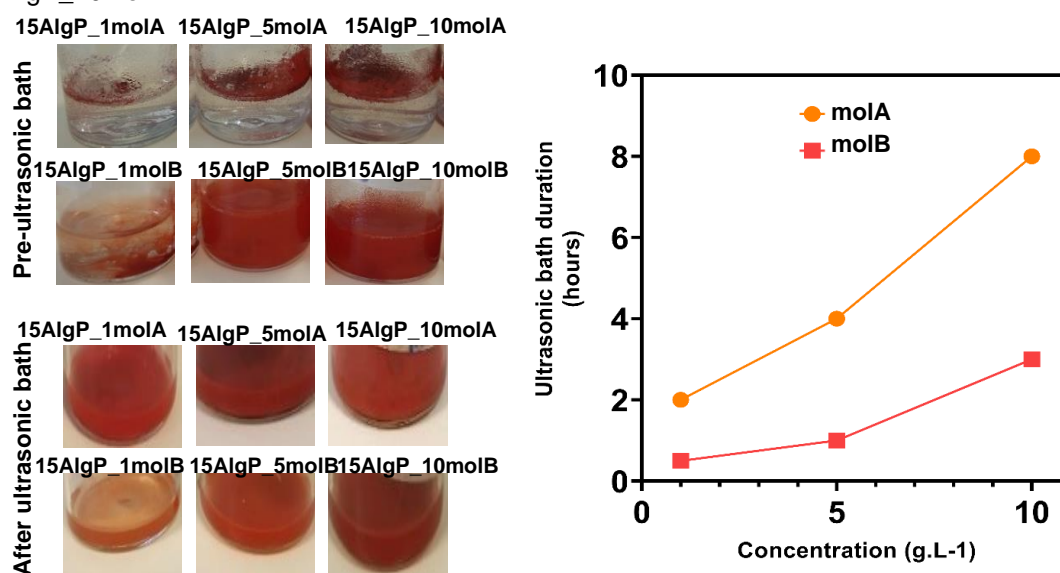


Figure 15. Ultrasonic bath duration of 15AlgP inks doped with 1, 5 and 10 g.L⁻¹ of molA or molB showing that higher concentrations require prolonged ultrasonic exposure. MolB particles disperse quicker than molA particles.

4.1.2 Cell Culture

4.1.2.1 Evaluation of formulation ingredients cytotoxicity

WST-8 assay was performed to evaluate the toxicity of the scaffold components (AlgP, molA and molB) in culture medium to confirm that these materials are biocompatible and can be used in the manufacturing of the scaffolds.

In the presence of an electron carrier, the WST-8 is reduced by molecules present in the membrane of metabolically active cells to produce a water-soluble, yellow-coloured product (formazan). In dead cells, this product is not formed. Formazan is soluble in the culture medium and directly proportional to the number of living cells, and this allows to determine the number of viable cells via colorimetric measurements.

For this assay, the absorbance of the positive control (cells cultured in DMEM) was assumed as 100% viability after 1 hour of incubation and the absorbances for the other conditions after 1 hour of incubation were normalised against this positive control. The same logic was followed at 24 hours of incubation.

After 1 hour of incubation, no significant differences in cell viability were observed between conditions (Figure 16). However, scaffold components conditions viability was above control viability (100%). WST-8 assay relies on the cleavage of the tetrazolium salt to formazan by cellular mitochondrial enzymes. The assumption is that the conversion is dependent on the number of viable cells. Nevertheless, the addition of AlgP, molA, and molB to the cells may result in increased enzymatic activity, to respond to potential induced cell metabolism stress, without affecting cell number or cell viability. Since the difference was up to 20% in viability, this phenomenon could have happened due to natural variations of cellular metabolism or minor pipetting errors that led to slightly more cells in a well than in another. After 24 hours, a decrease in the viability was observed for all the scaffold's components conditions. The culture medium with AlgP showed the viability of $78.48\% \pm 4.02$ and molA exhibited $69.7\% \pm 9.82$ and molB $71.92\% \pm 13.72$, respectively. AlgP viability is near to the non-cytotoxic domain (80-100% cell viability). However, molA and molB viability reached lower levels.

We hypothesise that at 24h cells are still adapting to the natural conjugated molecules presence and more time points at longer period of incubation are needed to precisely evaluate their impact on the cells. In the first 24h, L929 cells could have been more sensitive to natural conjugated molecules, but after 24 h, viability could increase. Considering these results, we decided to continue working with these materials.

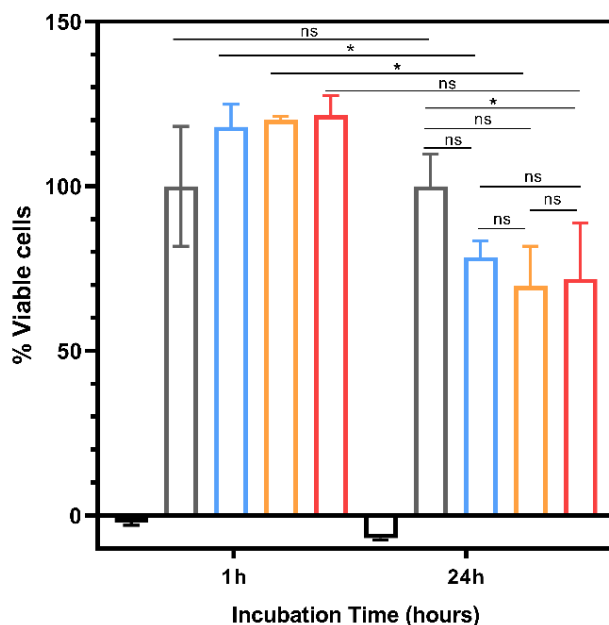


Figure 16. Cytotoxicity assay for biomaterials compounds. The viability of L929 fibroblasts cells grown on culture media (DMEM) supplemented with 15 g.L^{-1} AlgP (blue bar), 1 g.L^{-1} molA (orange bar), and 1 g.L^{-1} molB (red bar) using a WST-8 viability assay. DMEM (grey bar) is the positive control and triton-X (black bar) is the negative control. Viability measured for 1h and 24h of incubation reveals a non-significant decrease. DMEM incubation shows higher viability than the supplemented media. Data are shown as mean \pm SD ($n=3$). The student's test was performed (ns = not significant; * = $0.01 < p\text{-value} < 0.05$).

4.2 Ink characterisation

4.2.1 UV-Visible spectra

The presence of molA and molB was confirmed using UV-spectroscopy. The UV-spectra are illustrated in Figure 17. This method showed the potential for the analysis of molA and molB concentration because these pigments can absorb radiation in the visible region (380-700 nm). MolA spectrum showed three peaks around 460, 510, and 560 nm (Figure 17A) and the molB (Figure 17B) spectrum showed two peaks at 520 and 575 nm, respectively. Natural conjugated molecules have highly variable optical densities according with the organic solvents matrix (e.g. dichloromethane, hexane, or methanol) in which they are dissolved. In our study the solvent matrix was water, which can lead the natural conjugated molecules to exist in different forms than when dissolved in organic solvents, and thus make peak interpretation and comparison with other studies more challenging. Although the absorbance values could be mainly to the turbidity of the solutions, we could still identify similar patterns and characteristic peaks of each molecule.

UV-Vis spectrum of hydrogels, including natural conjugated molecules, showed similar profiles compared to the pigments present in natural fish, as astaxanthin. The colour is an important parameter for

food acceptability, with warm colours, typically leading to higher consumer acceptance than, for example, cold colours as blue (Spence 2021). These results are vital for developing 3D printed cell-cultured fish with structures and colour tonalities appealing to the consumer, which can play an essential role in consumer acceptance. Note that whitefish and some seafood also present warm (pink/red) colours.

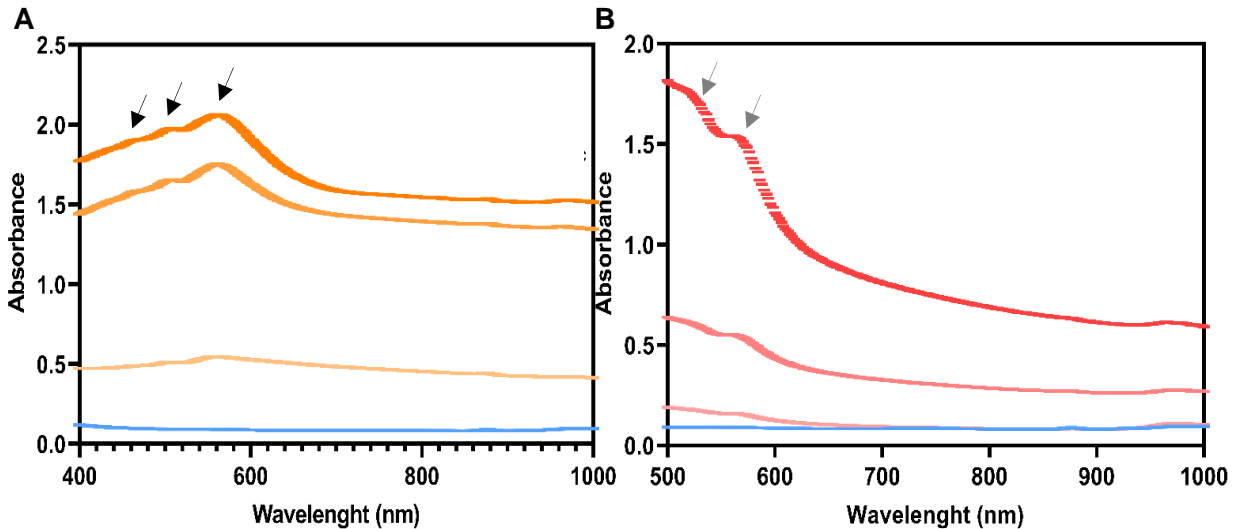


Figure 17. A) Uv-visible spectroscopy spectra of 15AlgP (blue), 15AlgP_1molA (light orange), 15AlgP_5molA (orange), and 15AlgP_10molA (dark orange) hydrogels showing characteristic peaks forming at $\lambda \approx 460, 510,$ and 560 nm suggesting the presence of molA inside AlgP hydrogel. Black arrows indicate the mentioned peaks. B) Uv-visible spectroscopy spectra of 15Alg, 15AlgP_1molB (light pink), 15AlgP_5molB (pink), and 15AlgP_10molB (dark pink) hydrogels showing characteristic peaks forming at $\lambda \approx 520$ and 565 nm suggesting the presence of molB inside AlgP

4.2.2 Rheological Assessment

4.2.2.1 Algae-based polysaccharide temperature-dependent behaviour

At high temperatures, AlgP exists in the solution as a random coil. Further cooling leads to helix formation and aggregation, which forms a stable 3D network. During this process, several factors can affect the transition temperature. To determine the transition temperature of the 15AlgP ink (see table 1 for nomenclature), temperature sweeps were performed, varying the temperature from 37 to 20 °C. This temperature range mimics what happens during the printing process, where 37°C corresponds to the incubator temperature and 25-20 °C to the printing temperature. To determine the changes in the polymer framework after adding natural conjugated molecules, 15AlgP_5molA ink was also tested.

The results are shown in Figure 18 with a viscosity versus temperature plot. The curves indicate the sol-gel transition (coil-to-helix) supported by a minimum point at 29°C, separating both behaviours. Below such temperature, the viscosity increases with cooler temperatures suggesting that the inks are more stable due to helix aggregation, reaching a solid-state. For temperatures higher than 29°C, the viscosity remains constant due to non-organised structures, probably as random coils.

The addition of molA showed no significant difference between the 15AlgP ink behaviour, suggesting that, at the concentration range used, natural conjugated molecules do not substantially affect the polymer framework of AlgP.

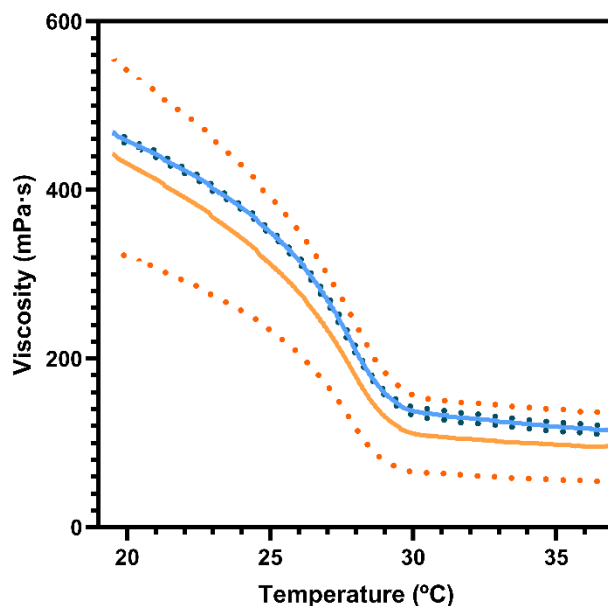


Figure 18. Rheological assessment of 15AlgP (blue) and 15AlgP_5molA (orange) inks. Temperature sweeps showing an increase in viscosity with decreasing temperature, indicating thermo-sensitivity. The addition of molA did not change the ink thermo-behaviour. Solid lines indicate the average values, and the dotted lines indicate the SD. Data are show

4.2.2.2 Algae-based polysaccharide gelation kinetics

To characterise the viscous behaviour of the materials, the storage modulus (G') and the loss modulus (G'') were recorded over ten minutes, at 25 °C. The G' represents the elastic portion of the viscoelastic behaviour and reflects the elastic performance of material when deformed. The G'' characterises the viscous portion of the viscoelastic behaviour, which reflects the flow of a material while it is deformed. When a 3D network is not fully developed, there are many non-interacting segments such as random coil and loops within the hydrogel. These are mobile domains and less effective elastically. The G'' is attributable to these non-interacting segments. During gelation, the establishment of more networks results in G' values higher than G'' , where solid-like behaviour dominates the viscoelastic properties of the hydrogel (Weng *et al.* 2007). Therefore, viscoelastic materials with $G' > G''$ reflect interactions inside the material, for example, chemical bonds or physical-chemical interactions.

Figure 19 represents the variance of G' and G'' in ten minutes for all the ink evaluated, respectively. In all conditions, our inks showed $G' > G''$, indicating that helix formation had already occurred. This behaviour is typical of gel-like products. This formation was confirmed with the graph showing no intersection between the G' and the G'' , indicating that gelation time already took place. We hypothesised that the gelation occurred during the sample preparation and placement on rheometer, and thus the inks

were crosslinked before the measurement. According to Stading and Hermansson, the absence of G' and G'' crossover reflects a similar dependence to that exhibited by solid gels (Stading and Hermansson 1990).

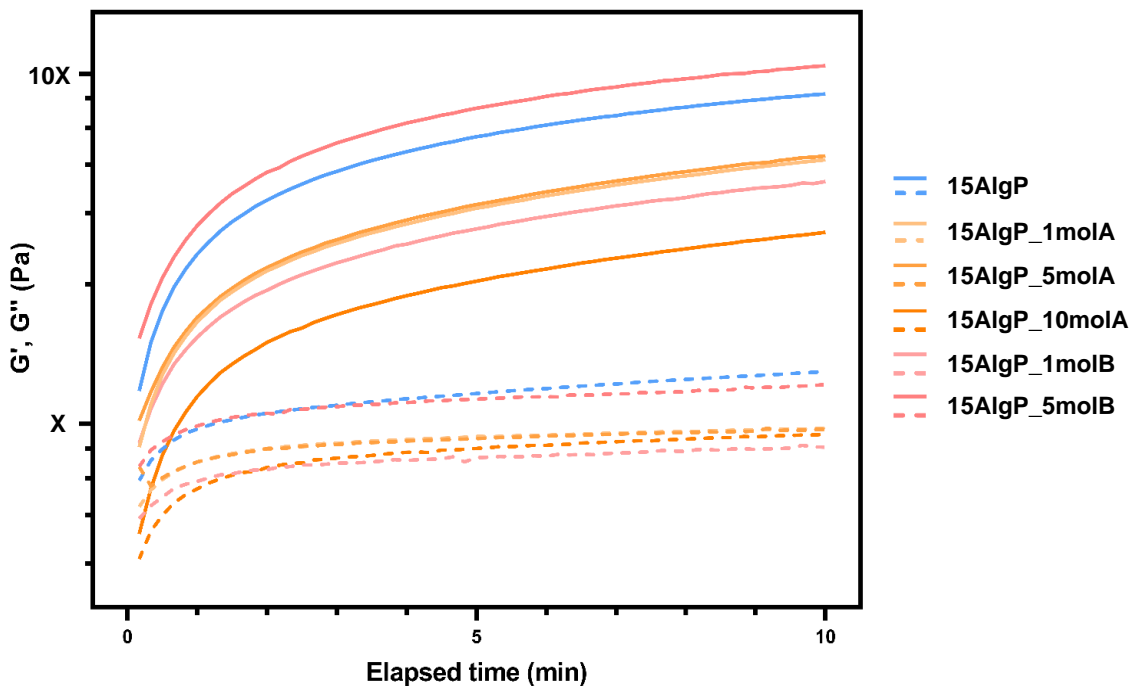


Figure 19. Monitoring the storage (G' —) and loss (G'' ---) modulus of 15AlgP, 15AlgP_1molA, 15AlgP_5molA, 15AlgP_10molA, 15AlgP_1molB, and 15AlgP_5molB inks for 10 minutes at 25°C. The values from y axis are presented in a confidential annex.

Actually, as seen above, for temperatures lower than 29°C, the sample's viscosity increases substantially, indicating that gelling is taking place. As the sample was placed at 25°C to perform the analysis, it induced the gelation of the inks. Therefore, the gelling kinetics was affected by the ink temperature. This experiment also confirmed that the sample handling window in its gel state is short and highly temperature-dependent.

The curve profile did not change with the addition of natural conjugated molecules. However, the addition of molA and molB resulted in a lower modulus, indicating that such particles inside the gel network prevent specific chemical and physical interactions. Inks 15AlgP_1molA and 15AlgP_5molA showed a similar impact in the network formation. However, 15AlgP_10molA ink showed to have a more accentuated impact. We hypothesize that the larger the particle agglomerate, frequent at this concentration could impact helix formation and other interactions within the gel. At low concentrations of molB, the ink follows a similar behaviour, except for 15AlgP_5molB ink. The higher values in viscoelastic functions of 15AlgP_5molB ink, in particular G' , suggests the existence of a more robust 3D network with more solid-like characteristics than the other conditions doped with natural conjugated molecules (e.g. conditions like in the 15AlgP ink). However, the impact of natural conjugated molecules on the 3D gel network needs to be studied in more detail to reach definitive conclusions.

Figure 20 represents G' (Pa) and G'' (Pa) at 10 minutes of elapsed time to facilitate the interpretation of each ink viscoelastic behaviour at such time point. After 10 minutes G'' , that represents the viscous portion of the viscoelastic behaviour, does not vary between conditions. This representation highlights that the natural conjugated molecules in the inks 15AlgP_1molA and 15AlgP_5molA have similar impact in the network formation, with similar G' . The 15AlgP_10molA, with higher molA content showed to have a more accentuated impact in the 3D network formation, attributed to the higher or larger particle agglomerates. The behaviour of 15AlgP_1molB ink is similar to 15AlgP_1molA and 15AlgP_5molA inks. However, increase of molB to an intermediate concentration of 5g.L^{-1} (15AlgP_5molB ink) leads to a viscoelastic behaviour like the 15AlgP (non-doped) ink. We hypothesised that at this concentration molB particles were able to dissolve and not only dispersed through the AlgP, leading to a solution with viscoelastic properties similar to those of 15AlgP. This result agrees with the ones from the ink formulation section where molB shown to had more efficient dispersion.

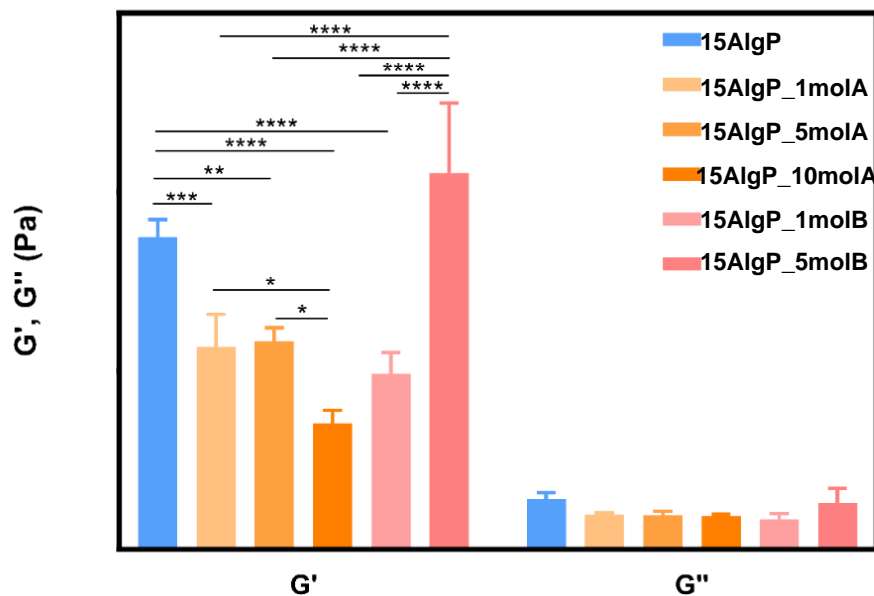


Figure 20. Graphical representation of the storage (G') and loss (G'') modulus of 15Alg, 15AlgP_1molA, 15AlgP_5molA, 15AlgP_10molA, 15AlgP_1molB, and 15AlgP_5molB inks after 10 minutes of elapsed time, at 25°C . Data are shown as mean \pm SD ($n=3$). Statistical significance was assessed using 2way ANOVA analysis showing non-significant (<0.9999) p-values for G'' and significant p-values for G' (* = $0.01 < p\text{-value} < 0.05$; ** = 0.0016 ; *** = 0.0009 ; **** = < 0.0001). The values from y axis are presented in a confidential annex.

4.3. Scaffold characterisation

4.3.1 Casting hydrogels on moulds

Hydrogels were cast on moulds to showcase the ability of our materials to form 3D gel structures. Casted AlgP and AlgP doped hydrogels were successfully prepared within 5-10 minutes of incubation at RT. This method confirmed that AlgP concentrations below 15g.L^{-1} result in liquid solutions that do not

support themselves (Figure 21A). Higher AlgP concentrations seemed to lead to more robust hydrogels (Figure 21B). Hydrogels with different shapes and sizes were prepared. These hydrogels maintained their physical structure and capacity to self-support for at least two months, immersed in PBS at RT. Several characterisation techniques were subsequently performed to evaluate the properties of these hydrogels further.

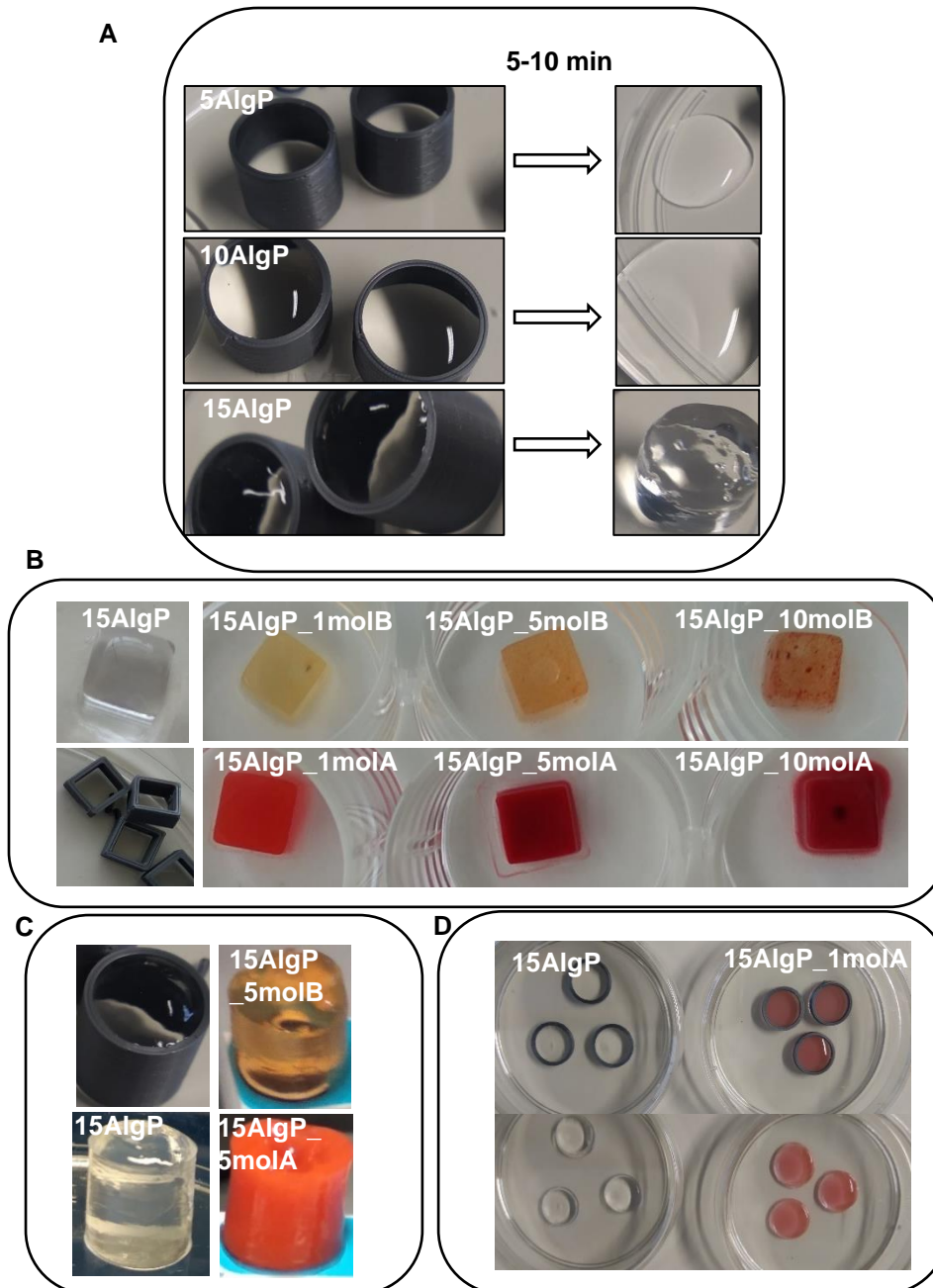


Figure 21. A) At left is shown the 5AlgP, 10AlgP, and 15AlgP inks once inside the 3D printed moulds, and at the right the respective structure after 5-10 minutes of gelation. 5AlgP, 10AlgP hydrogels were not solid while 15AlgP originated a solid structure. At the bottom 15AlgP based inks were used to construct hydrogels using moulds with different shapes B) 3D squared moulds (5 mm x 5 mm); C) 3D cylindric moulds with diameter a of 9 mm and 8 mm in height; D) 3D circle mould with a diameter of 9 mm and 2 mm in height.

4.3.2 Mechanical evaluation

4.3.2.1 Compression tests

A uniaxial compression test was performed to evaluate the mechanical properties of the inks. The Young's modulus values of each sample were calculated from the stress-strain curves showed in Figure 22. Young's modulus values shown in Figure 23 do not present statistical difference between the values, which indicates that the addition of natural conjugated molecules does not significantly affect the mechanical properties of the hydrogels. The construct robustness was also shown through mechanic manipulation of the structures (using tweezers and a spatula), with no permanent deformation observed (Annexe 2). The mechanical properties are crucial for developing 3D printed cell-cultured fish. Consumer acceptance will rely on the cell-cultured fish structure, texture, and resemblance to fish meat. Yutaka *et al.* estimated a young's modulus of non-frozen tuna meat to be approximately 50 kPa (Sciences 1992). Other authors revealed that fish epidermal keratocytes (wound-healing cells in fish skin) show a modulus ranging from 10-55 kPa (Laurent *et al.* 2005). These values are in the order of magnitude of those obtained for AlgP based scaffolds. Therefore, we considered our scaffold adequate for developing 3D printed cell-cultured fish. In the future, compression tests and young modulus estimations will also be considered for the cooked fish tissue.

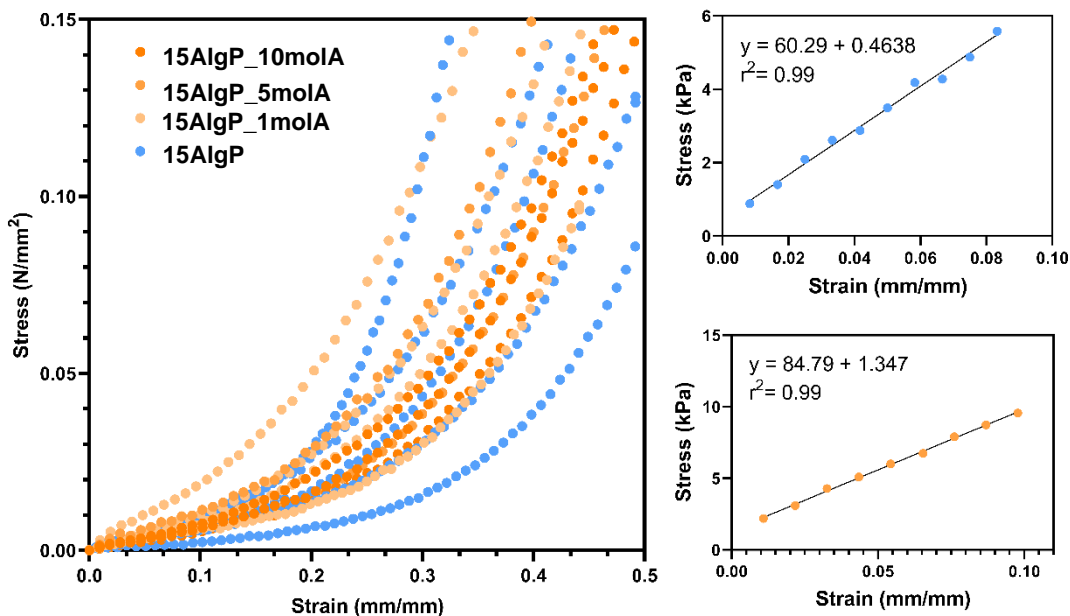


Figure 22. A) Compression stress-strain curve of 15AlgP, 15AlgP_1molA, 15AlgP_5molA, and 15AlgP_10molA hydrogels. B) Stress-strain linear regressions of 15AlgP and 15AlgP_5molA showing $r^2 > 0.9$ and the calculated slope values (Young's modulus) in kPa.

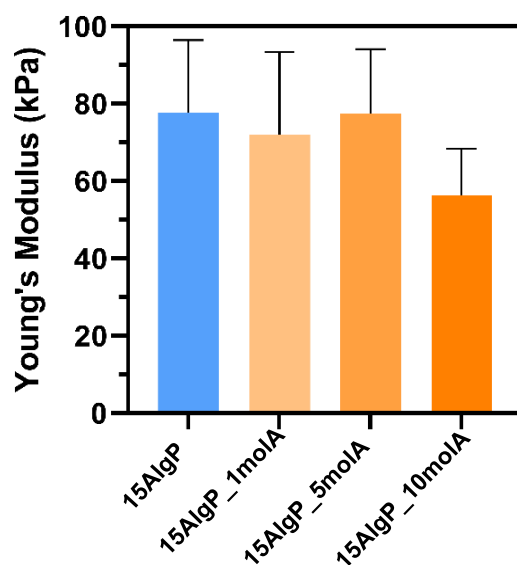


Figure 23. Quantified Young's modulus of the 15AlgP, 15AlgP_1molA, 15AlgP_5molA, and 15AlgP_10molA hydrogels. A similar behaviour of Young's modulus is observed for all hydrogels. Data are shown as mean \pm SD. Statistical significance was assessed using t-student analysis showing non-significant p-values (p -value ≥ 0.05).

4.3.3 Chemical and physical characterisation

4.3.3.1 Water content

Water is the principal component of the edible portions of seafood. The average moisture percentage in raw edible fish and shellfish flesh varies between $\approx 70\%$ and 82.8% . Some examples of typical edible fish water contents are present in Table 5 (Venugopal and Shahidi 1996; Lenas *et al.* 2011; van Ruth *et al.* 2014). Therefore, high water content values of the scaffolds are highly relevant to mimic the fish native tissue as this can significantly affect the organoleptic properties and texture of the 3D printed fish fillet.

The fabricated scaffolds' water content values are represented in Figure 24. Figure 24A describes the performance of AlgP scaffolds prepared at different AlgP concentration and Figure 24B of the scaffolds doped with natural conjugated molecules. There is a small, but statistically significant different reduction of the water content with the increase of AlgP concentration, explained by an increase in the cross-linking density (Nishida *et al.* 2021). Higher AlgP concentrations enhance helix formation and aggregation, increasing the cross-linking density of the scaffold 3D network. The addition of natural conjugated molecules had nearly no effect on the water content of the scaffolds. These molecules are dispersed in the 3D network and could interact with the AlgP arrangement or cross-linking. However, the addition of natural conjugated molecules does not affect the water content. All scaffolds showed a water content above 97% . The water content can be a predominant factor affecting the cell adhesion strength and behaviour (Nishida *et al.* 2021).

This impact will be discussed later. In sum, considering that water content percentage within the scaffold should decrease with cell growth and naturally produced ECM components, we consider that our scaffold is suitable for fish cell culture.

Table 5. List of common edible fish species and their correspondent water contents in percentage with respective literature references.

Fish specie	Water content (%)	Reference
Cod (<i>Gadus morhua</i>)	81.6 ± 1.9	
Salmon (<i>Salmo salar</i>)	69.3 ± 6.6	(van Ruth <i>et al.</i> 2014)
Shrimp (<i>Caridean shrimp</i>)	82.4 ± 4.3	
Mediterranean sea bass (<i>Dicentrarchus labrax</i>)	74.6	(Lenas <i>et al.</i> 2011)
Blue fin Tuna (<i>Thunnus thynnus</i>)	71.2	(Venugopal and Shahidi 1996)
Turbot (<i>Rhombus maximus</i>)	80.9	

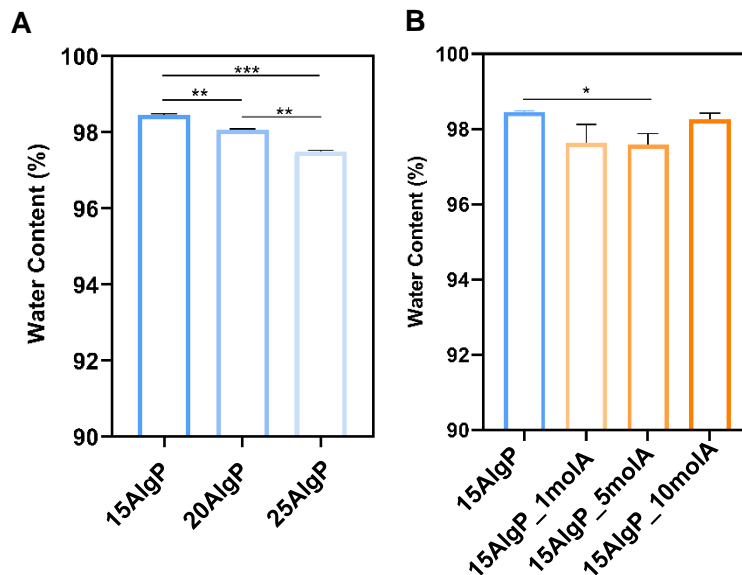


Figure 24. A) Water content of the 15AlgP, 20AlgP, and 25AlgP hydrogels and of B) 15AlgP hydrogel compared with 15AlgP_1molA, 15AlgP_5molA, and 15AlgP_10molA. Data are shown as mean ± SD (n = 3). Statistical significance was assessed using t-student analysis showing non-significant p-values (p-value ≥ 0.05) and values with different significances (* = 0.01 < p-value < 0.05; ** = 0.001 < p-value < 0.01; *** = 0.0001 < p-value < 0.001).

4.3.3.2 Swelling degree

Algae-based polysaccharide (AlgP) hydrogels were analysed for their water uptake capacity (swelling degree). In fish, the ability to maintain water balance and homeostasis derives from robust mechanisms of osmoregulation (Ortiz 2001). This way, marine animals have a high capability of preserving the organism's water content levels. Besides, as seen above, fish tissue has high water content values and do not require swelling function. Therefore, our AlgP based scaffolds must have a low capacity of uptake water. Since the constructed scaffolds have high water content, we anticipated that the swelling degree would be small.

The results are illustrated in Figure 25. Hydrogels start to swell immediately after immersion in PBS and reach the equilibrium of swelling after 72h (3 days), at 10% of swelling degree. The high swelling rate until day 3 was due to the initial ionic potential difference (Figure 25A). After that, internal and external ions reached an equilibrium state, stabilising the swelling rate. From day 7 until day 40, the hydrogels remained in solution (Figure 25B). The slightly decrease in scaffold weight reveals water loss, possible degradation of the hydrogel or could be also associated with sample manipulation. Thus, more time points are required to evaluate the degradation effects precisely.

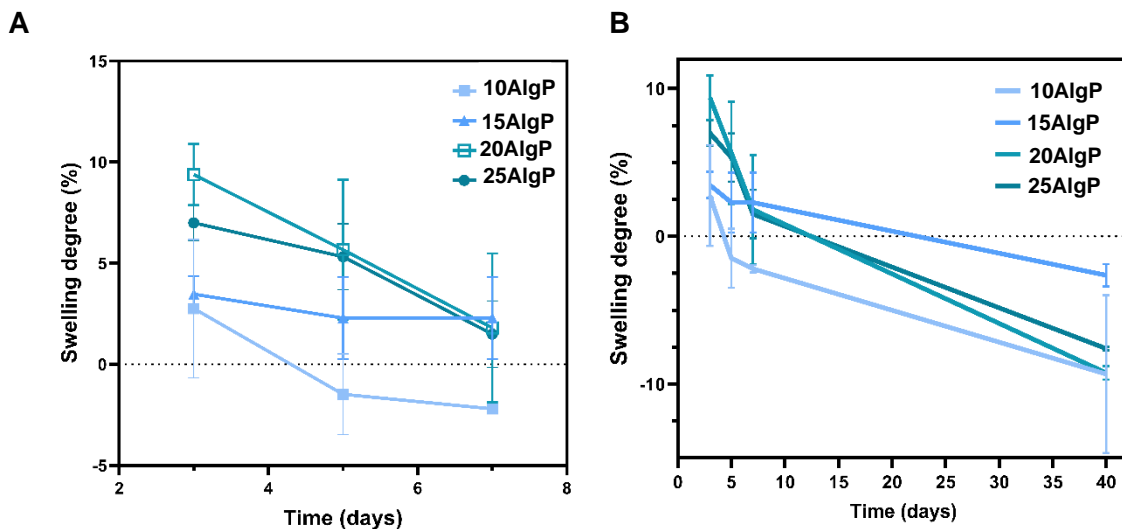


Figure 25. A) Swelling degree for 10AlgP, 15AlgP, 20AlgP, and 25AlgP hydrogels at days 3, 5, and 7. Swelling reaches a swelling of 10% at day 3. B) Swelling degree for 10AlgP, 15AlgP, 20AlgP, and 25AlgP hydrogels at days 3, 5, 7 and 40. Data are shown as mean \pm SD (n = 3).

4.3.4 Surface proprieties

The surface characteristics of the scaffolds can potentially impact biocompatibility by limiting the cell-material interaction. Thus, proprieties as wettability, surface chemistry, surface energy, and surface topography impact cell-biomaterial interaction (Menzies and Jones 2010). In this section, surface wettability and surface topography are discussed.

4.3.4.1 Evaluation of the surface wettability

The contact angle was measured to evaluate the wettability of the surface of the scaffold. High contact angles indicate a low wettability and a hydrophobic solid surface, while low contact angles suggest high wettability and hydrophilic surfaces. Figure 26A shows that AlgP scaffolds and AlgP doped scaffolds exhibited a low contact angle between 1.2° and 3.3° . Consequently, the surface wettability exhibit superhydrophilic behaviour. This behaviour was expected as our structures have a very high content of water molecules. Figure 26B confirmed it by demonstrating images taken seconds after the contact drop surface where the glycerol drop formed a continuous fluid film over the scaffold surface.

A study by Menzies *et al.* discusses the impact of contact angle on biocompatibility, the authors recognised that superhydrophilic surfaces prevent cell-material interactions, and can promote cell-cell interactions leading to spheroid formation (Menzies and Jones 2010). In section 4.5.1.3, the impact of contact angle (surface wettability) on cell behaviour is further discussed.

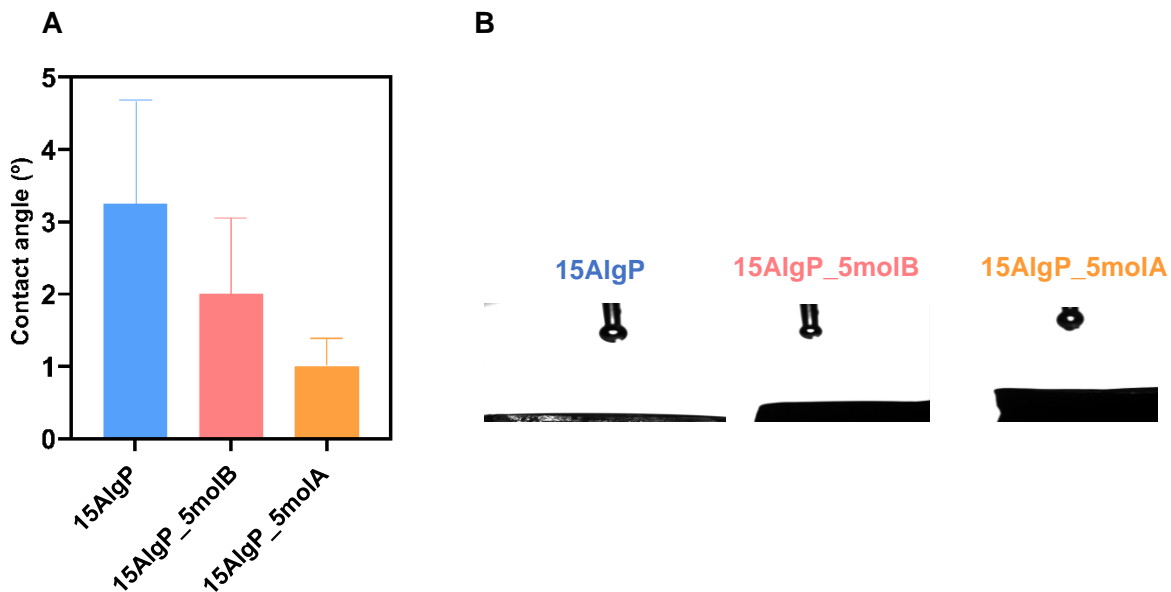


Figure 26. Surface properties of the 15AlgP, 15AlgP_5molA, and 15AlgP_5molB hydrogels. A) The hydrogels show low contact angles, typical of superhydrophilic specimens. Data are shown as mean \pm SD. B) Representative images of each contact angle measurement.

4.3.4.2 Scanning Electron Microscopy (SEM)

The morphology and surface topography of the AlgP scaffolds and AlgP doped scaffolds was evaluated by SEM at different magnifications. Microstructure analysis of the hydrogel specimens via SEM revealed the presence of specific morphologies on the hydrogels as flake-like and sponge-like structures (Figure 27). Flake-like structures were observed in AlgP, molA, and molB hydrogels showing consistency between specimens. We expected the porosity of these structures to be relatively high. However, due to the limitations in the sample preparation process, pores were not observed. Alternative sample preparation techniques such as critical point drying will be considered in the future to preserve the porosity of the hydrogels.

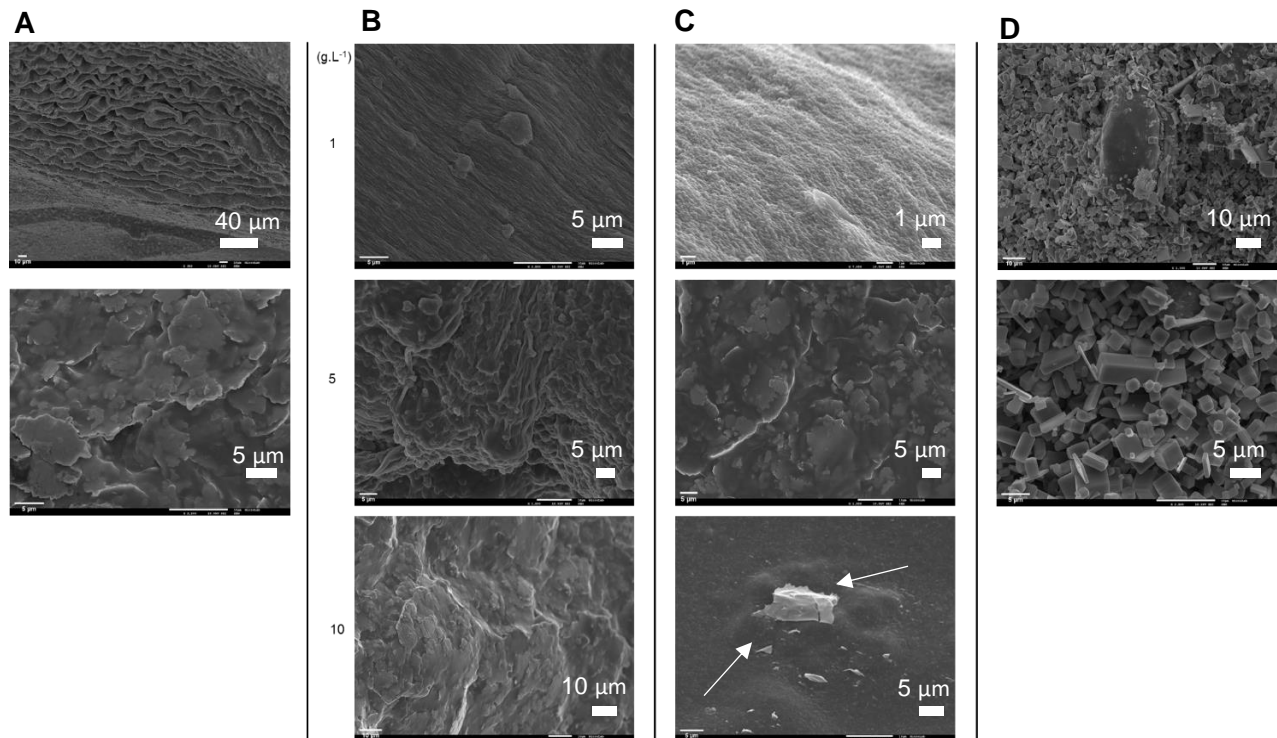


Figure 27. Scanning electron microscopy (SEM) images of the scaffolds. A) SEM images of 15AlgP hydrogel showing a sponge-like (top image), and flake-like (bottom image) structures; B) SEM images of 15AlgP_1molA, 15AlgP_5molA, and 15AlgP_10molA hydrogels also showing flake-like structures (at 10g.L⁻¹). C) SEM images 15AlgP_1molB, 15AlgP_5molB, and 15AlgP_10molB hydrogels with similar flake-like structures (at 5g.L⁻¹) and indicating the formation of molecule B particles (at 10g.L⁻¹) on the hydrogel surface in comparison to non-doped 15AlgP hydrogel. White arrows indicate the presence of molB particles surrounded by the AlgP matrix. D) SEM images of 15AlgP hydrogel and structures that can be crystals at the hydrogel surface.

4.3.5.1 Electrochemical Impedance Spectroscopy

The scaffolds conductivity depends on the efficiency of the polymer's charges transport and the interchain transport efficiency. There are two mechanisms on how electrical current can flow in a hydrogel: ionic, electronic, or a mixture of both. Here, the electronic behaviour of the hydrogels' scaffolds was assessed using electrical impedance spectroscopy (EIS). Impedance is the opposition to current flowing in an AC circuit that contains resistance (the real part) and reactance (the imaginary part). Usually, impedance values are represented using the Nyquist and the Bode plot. The Bode plot provides information about impedance's frequency-dependent behaviour and phase angle behaviour (θ). The Nyquist plot represents the negative imaginary impedance ($-Z''$) plotted versus the real part of the impedance (Z'), and through its interpretation is possible to identify the equivalent circuit of our system and calculate the resistance (R).

The impedance phase angle of a perfect resistor is 0° . For a perfect inductor, impedance θ is $+90^\circ$, and for an ideal capacitor, impedance θ is -90° . A negative phase shows the presence of a capacitor, and a positive sign reveals the existence of an inductor. Figure 28 demonstrates that all the evaluated hydrogels behave like capacitors since the θ approaches $\sim -80^\circ$ at low frequencies ($\leq 100\text{Hz}$) but do not reach 90° (Premathilake *et al.* 2017). This observation indicates the predominant capacitance but with possible additional contribution from distributed charge storage (Bo *et al.* 2012). In fact, in our hydrogels the conduction is mainly ionic, and in the interface between the electrodes is formed an electric layer composed of ions (Bockris and Reddy 1998). For this reason, in the interface between the metal electrode and our hydrogels, the frequency dispersion response cannot be described by an ideal capacitor, and the response is described by a constant phase element (CPE) a frequency dependent component used to represent deviations from an ideal capacitor (Freire 2010). Therefore, we considered the presence of a CPE as a capacitor that changes with the frequency (Mobarak *et al.* 2012).

Moreover, the capacitive reactance of a capacitor decreases as the frequency across its plates increases. Therefore, capacitive reactance is inversely proportional to frequency. Capacitors store electrical energy in an electric field. As the frequency increases, the capacitor passes more charge across the plates each time, resulting in a higher current flow through the capacitor, appearing as if the internal impedance has decreased. This behaviour was observed for all the evaluated scaffolds since impedance has a high value at low frequencies and a low value at higher frequencies (Figure 29).

On the other side, at high frequencies (100000 Hz), the phase angle of all fabricated scaffolds approached zero, behaving like resistors. At this frequency, impedance becomes independent of frequency, such behaviour had already been reported for gellan gum conducting hydrogels filled with PEDOT:PSS with a water content above 97%, as in our specimens (Warren and in het Panhuis 2014). With these results, we hypothesize that the fabricated scaffolds work as capacitors at low frequencies and as resistors at high frequencies.

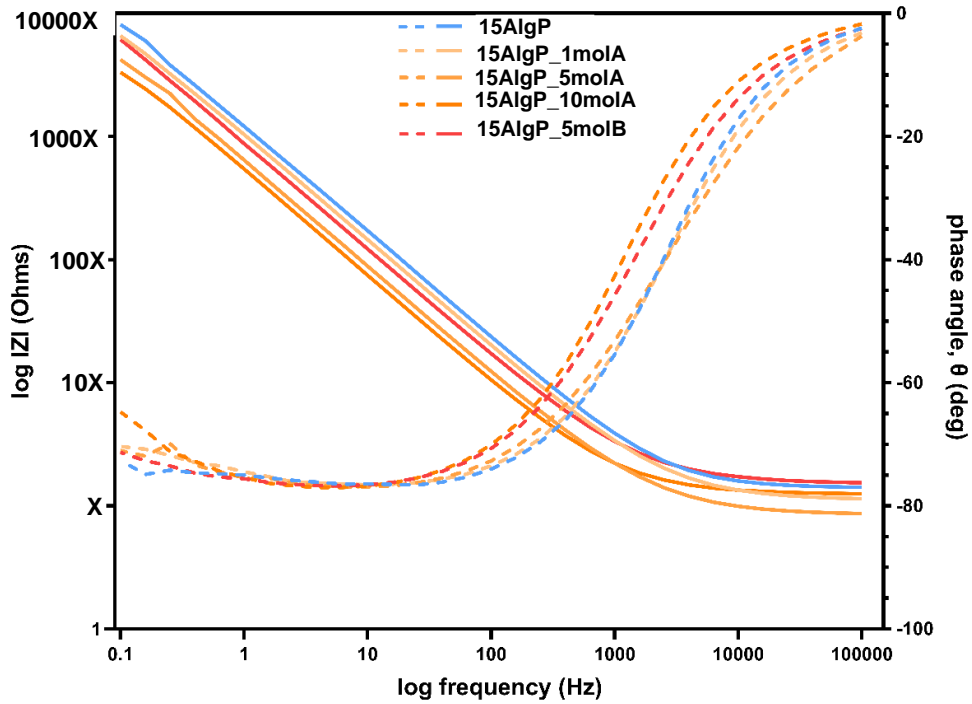


Figure 28. EIS Bode plot of 15AlgP, 15AlgP_1molA, 15AlgP_5molA, and 15AlgP_10molB wet hydrogels. The x-axis is a logarithmic scale of the frequency, and the y-axis is the logarithm of the impedance, |Z|, while the second ordinate is the phase angle, θ . 15AlgP hydrogel shows higher impedance than molecule A doped hydrogels. Data are shown as mean \pm SD (n=3). The values from y axis are presented in a confidential annex.

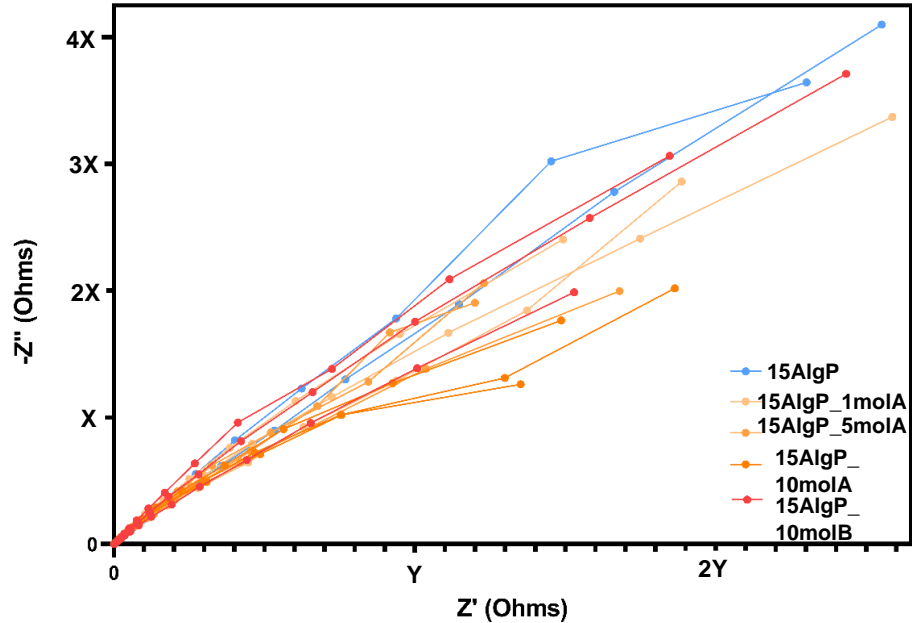


Figure 29. EIS Nyquist plot of wet hydrogels doped with varying concentrations of molecules A and B: 15AlgP, 15AlgP_1molA, 15AlgP_5molA, and 15AlgP_10molB. The negative imaginary impedance $-Z''$ is plotted versus the real part of the impedance Z' . The values from y axis and x axis are presented in a confidential annex.

Figure 29 shows the Nyquist plot for all hydrogels recorded at RT. The curve profile displays a linear relation between the Z' and Z'' components of the impedance, with a slope of 45° , suggesting that the hydrogel is behaving like a Warburg diffusion element (W_s), that is usually used to model charge carriers like ions (Warren and in het Panhuis 2014).

The data in the Bode and Nyquist plots allowed to create a possible equivalent circuit (Figure 30) to estimate the solution resistance (R_s) of the hydrogels and to calculate the conductivity (σ). Therefore, the constructed equivalent circuit model considers a charge transfer resistance (R_{ct}) due to a combination of kinetic and diffusion processes (Warburg Impedance), and a CPE. The equivalent circuit for modeling interfacial electrochemical reactions represents the combination of the R_s in series with the double layer capacitance, approximated to a CPE. Since a charge transfer diffusional reaction is occurring in parallel with the charging of the double layer, the R_{ct} associated with that response is in parallel with the CPE. Moreover, we considered that the reaction is controlled by a charge diffusion rate, and a diffusional resistance element (W_s) is present in series with the R_{ct} (Lasia 1999).

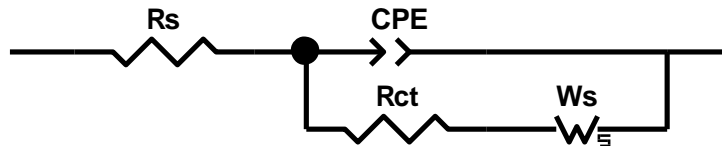


Figure 30. A possible design of the equivalent circuit of the fabricated scaffolds system composed of a constant phase element (CPE), a R_{ct} (Charge transfer resistance), and a W_s (Warburg element) representing the diffusional impedance. R_s is the solution resistance.

EIS performed on the scaffolds confirmed a slightly increased conductivity of the hydrogels doped with $1\text{g}\cdot\text{L}^{-1}$ molA (15AlgP_1molA) (Figure 31). Higher concentrations of both natural conjugated molecules are shown to achieve the opposite effect. Lately, several examples of polymers based on π -conjugated backbones have been established (Bouaamlat *et al.* 2020). The π -conjugates enhance the mobility of electrons along the molecule backbone. Here, we hypothesis that higher molecules concentrations may lead to aggregates formation. These aggregates may be blocking the mobility of electrons along with the network. Consequently, lower concentrations achieved higher conductivities.

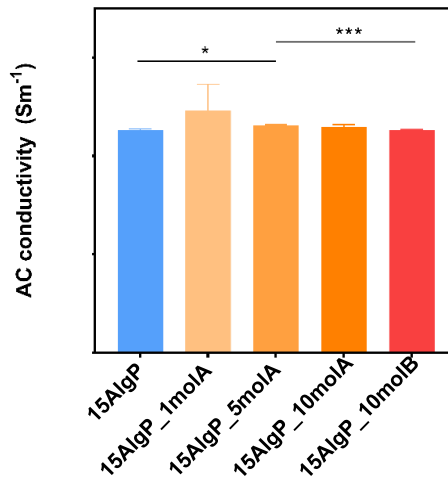


Figure 31. Conductivity of wet 15AlgP, 15AlgP_1molA, 15AlgP_5molA, 15AlgP_10molA, and 15AlgP_10molB hydrogels. Data are shown as mean curves \pm SD..

4.3.5.2 Four-probe method

The hydrogel samples were dried to assess differences in conductivity in the wet and dry states (Figure 32). The conductivity of the dry specimens increased with the addition of natural conjugated molecules, except for the hydrogel 15AlgP_5molA. However, this specimen provided handling problems during the drying process and the gold deposition step (resulting in less than four thick gold strips), making the result not significantly robust (n=1). Alternative sample preparation methods such as thermal drying will be considered in the future. On the other side, the other hydrogels doped with molA and molB revealed higher conductivities. As seen above, a consistent behaviour was observed where to high concentrations of natural conjugated molecules resulted in lower conductivity. This behaviour may be due to the aggregate formation, which blocks the charge motion. Therefore, the dried hydrogel that showed higher conductivity was 15AlgP_1molB. The comparison of such value with the ones from EIS analysis shows that the ionic component of the conductivity of our systems surpasses the electrical component. However, this brings up a potential feature for our scaffolds that will be evaluated in the future.

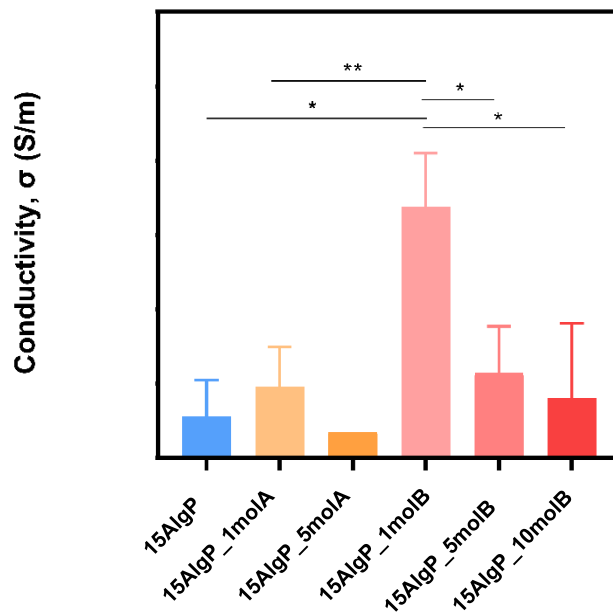


Figure 32. Electrical conductivity of dried 15AlgP, 15AlgP_1molA, 15AlgP_5molA, 15AlgP_10molA, 15AlgP_1molB, 15AlgP_5molB, 15AlgP_10molB evaluated via four-point probe measurements. Non-doped 15AlgP showing less conductivity than doped hydrogels, except for 15AlgP_5molB. Lower concentrations of AlgP and molB resulted in higher conductivities. The conductivity of 15AlgP_1molB hydrogels is almost four times higher than 15AlgP_1molB hydrogel. Data are shown as mean \pm SD (n=3, except for 15AlgP_5molA due to sampling problems). Statistical significance was assessed using t-student analysis showing non-significant p-values (p-value \geq 0.05) and values with different significances (* = 0.01 < p-value < 0.05; ** = 0.001 < p-value < 0.01).

4.3.5.3 LED light test

A light-emitting diode (LED) light demonstrated that it was possible to conduct direct current (DC) using the hydrogel to supply a LED (Figure 33A). The relative intensity of the LED was calculated by the area of emitted light (Figure 33B). A conductive metal was used as a positive control and the air as the negative control. The 15AlgP_5molA hydrogel turned on the LED with $\frac{1}{4}$ of the positive control intensity. In the future, we will consider performing the experiment for the 15AlgP hydrogel to precisely evaluate the impact of adding natural conjugated molecules to our hydrogels, as this will be a more accurate control of the experiment.

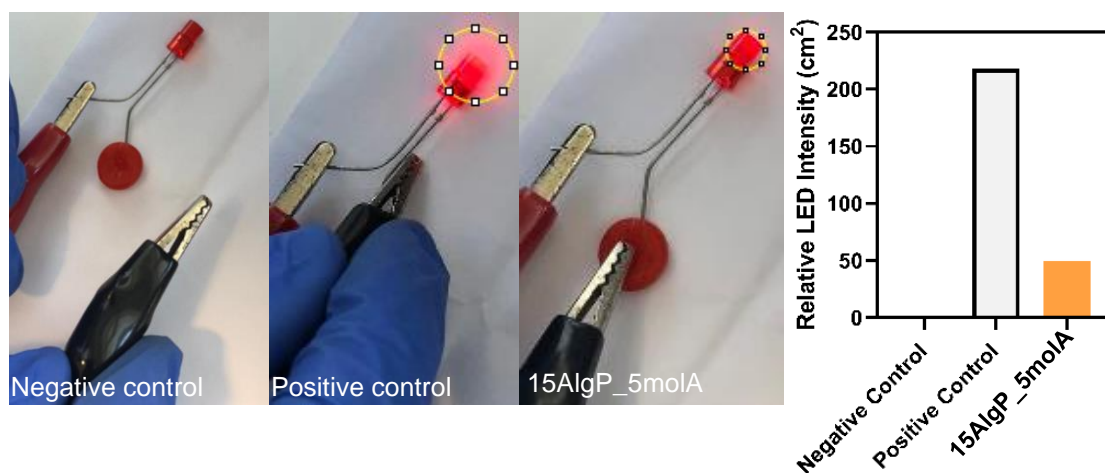


Figure 33. A) Images of a DC circuit conducted using 15AlgP_5molA hydrogel and a LED. B) Quantified LED intensity using the area of emitted light. A conductive metal was used as a positive control and the air as the negative control.

4.3.5.4 Cyclic voltammetry

Cyclic voltammograms of all evaluated hydrogels showed almost the mirror image of the potential sweep (positive-moving) curve in the opposite direction of sweep (negative-moving) (Figure 34). This compartment demonstrates the reversibility of the redox-capacitor. In his work, Bo *et al.* describes that an enlargement of the CV curve area with increasing voltage scan rate for rectangular-shaped curves indicates a predominant capacitive behaviour (Bo *et al.* 2012). The obtained voltammograms are close to a rectangular shape, which is characteristic of non-ideal capacitors (Allagui *et al.* 2016). This result supports the findings obtained in the impedance spectroscopy.

The redox-capacitor response seemed to depend on scan rate since cyclic voltammograms showed differences in their area. Capacitance is directly proportional to the curve area, so it varies at different scan rates (Bandaranayake *et al.* 2015). Therefore, it was clear that the addition of natural conjugated molecules resulted in larger curves, representing an enhanced capacitive behaviour (for more scan rates see Annex 4). Moreover, hydrogels doped with molA seemed to have slightly more capacitance than the hydrogels

doped with molB, suggesting that molA helps to store charges. This behaviour was accentuated at scan rate 0.4 V.s^{-1} where the hydrogels 15AlgP_1molA and 15AlgP_5molA had larger curves. EIS analysis complemented this observation (Allagui *et al.* 2016).

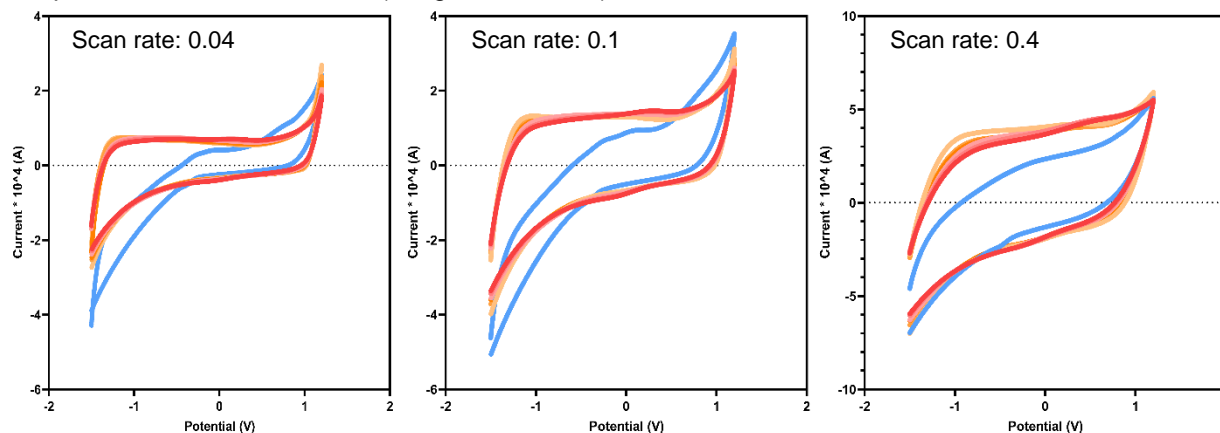


Figure 34. Cyclic voltammetry measurement at different scan rates (0.04 V.s^{-1} , 0.1 V.s^{-1} , and 0.4 V.s^{-1}) of all the fabricated hydrogels indicating an enlargement of the curve area with the increase of the voltage scan rate. Legend: 15AlgP (blue), 15AlgP_1molA (light orange), 15AlgP_5molA (orange), 15AlgP_10molA (dark orange), 15AlgP_1molB (light pink), 15AlgP_5molB (pink), and 15AlgP_10molB (dark pink).

4.4 3D Printing

Extrusion-based 3D printing technique was used to fabricate 3D scaffolds through continuously depositing material layer-upon-layer, without any material as support (Kirchmayer *et al.* 2015). We anticipated that AlgP scaffolds could self-supported itself since hydrogels produced with moulds originated consistent and rigid structures.

4.4.1 Printability evaluation

4.4.1.1 Printability factor

Printability evaluation measures the fidelity of the printing process and prevents the fabrication of undesirable printed structures. Ink printability, namely the ability to form a 3D structure with exemplary integrity, is a representative criterion to evaluate the ink physical properties.

Printability quantification with the printability factor (Pr) revealed that 15AlgP, 15AlgP_5molA, 15AlgP_1molB, and 15AlgP_5molB showed to be adequate inks (inside the grey region, $0.85 \leq \text{Pr} \leq 1.1$ Figure 35B) to form rectangular pores ($\text{Pr} \approx 1$). The ink 15AlgP_5molA showed a slight drop in Pr with a bit of tendency to have strut fusion (Figure 35A). However, this ink printability was inside the printability region (grey region, Figure 35B). On the other side, the ink 15AlgP_10molA showed a relevant drop in Pr with a tendency to have strut fusion and more circular pore morphology (Figure 35A). We hypothesised that the decrease in printability with the addition of 10 g.L^{-1} of molA to the 15AlgP solution was due to larger particles that changed the flow along the needle. In contrast, 15AlgP_1molB, and 15AlgP_5molB inks showed the highest printability among all the samples, revealing a tendency to form rectangular pores even clearer than

15AlgP (Figure 35A). This result agrees with the ones from the ink formulation and rheological assessment where molB shown to had more efficient dispersibility, that could had led to a more fluid flow along the printing needle, therefore, resulting in higher printability. In conclusion, the results confirmed that the dispersion of natural conjugated molecules did not affect the printability of the hydrogels.

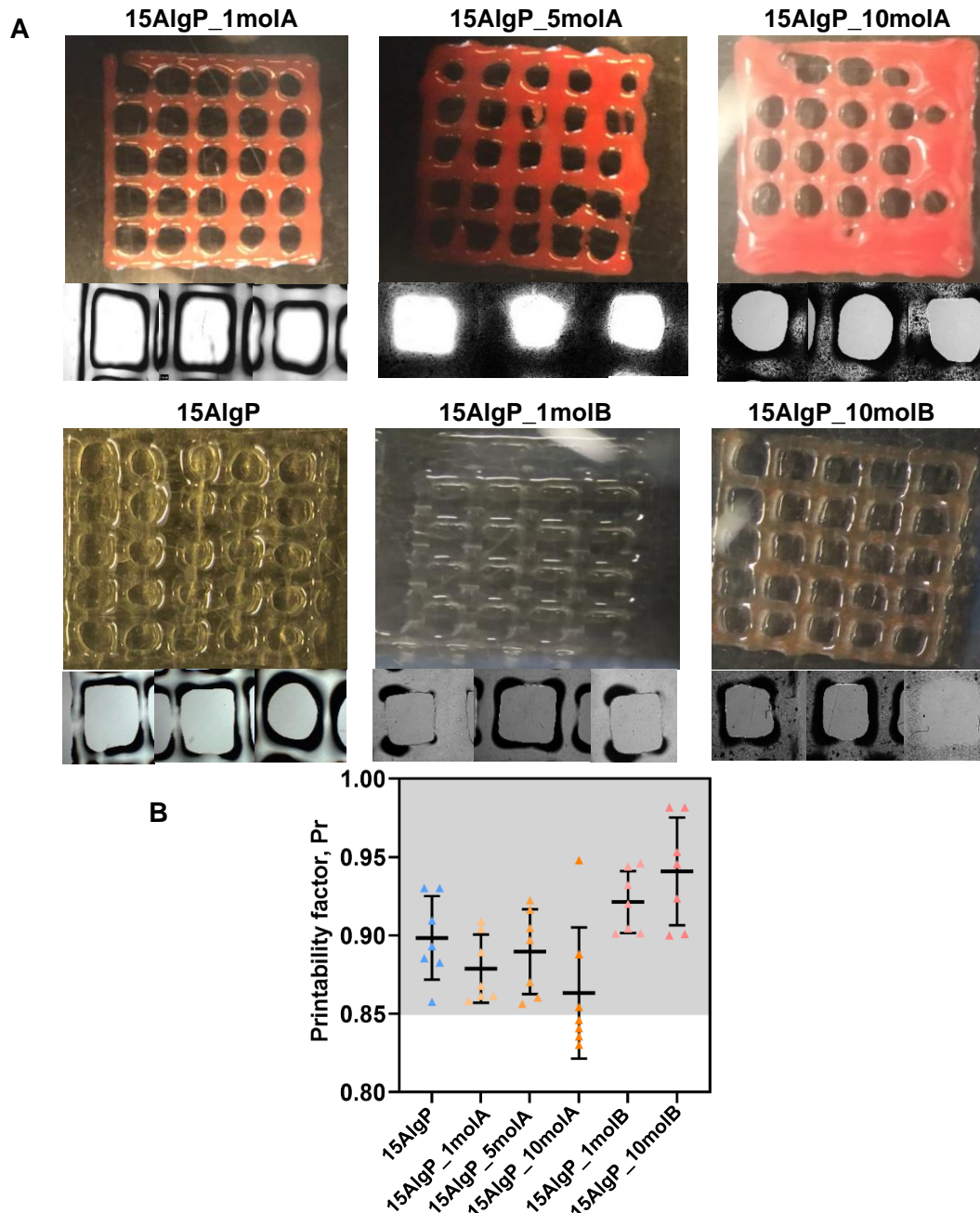


Figure 35. A) Optical microscopy images of 3D-printed 15AlgP, 15AlgP_1molA, 15AlgP_5molA, 15AlgP_10molA, 15AlgP_1molB, and 15AlgP_5molB squared meshes (top) and the light microscope image of each evaluated square inside the respective squared mesh (bottom). B) Printability factor (Pr) derived from the 3D-printed hydrogels, is inversely proportional to pore-circularity, an indicator of pore circularity and hence printability of the ink (Pr = 1 perfectly square pore, Pr < 1 circular pore, and Pr > 1 over-gelated pore). The grey region marks the range of adequate ink printability (from 0.85 to 1.1) (Ouyang *et al.* 2016). Data are shown as mean \pm SD (n=7).

4.4.1.2 Line thickness evaluation

The line thickness of 3D printed squared meshes with a different number of layers was evaluated (Figure 36). The anticipated line thickness is 0.5 mm as this is the inner needle diameter. All the evaluated scaffolds showed a line thickness increase with the increase of layer with an inclination to form strut fusions and pore circularity. Line thickness was higher for the 15AlgP_5molB at all printed layers (Figure 37). This behaviour has been reported for high water content materials. In their work, Senior *et al.* anticipated that the low viscosity of the hydrocolloid solutions caused them to spread and fall when printing multi-layered structures. To overcome these hurdles, she discussed a manufacturing approach using a supportive particulate gel bed and have enabled the production of complex gel structures (Moxon *et al.* 2017; Senior *et al.* 2019). In future experiments, we will consider applying such manufacturing strategy to our material. Other approaches related to the printing parameters, improving the crosslink degree, and the gelation process will be evaluated.

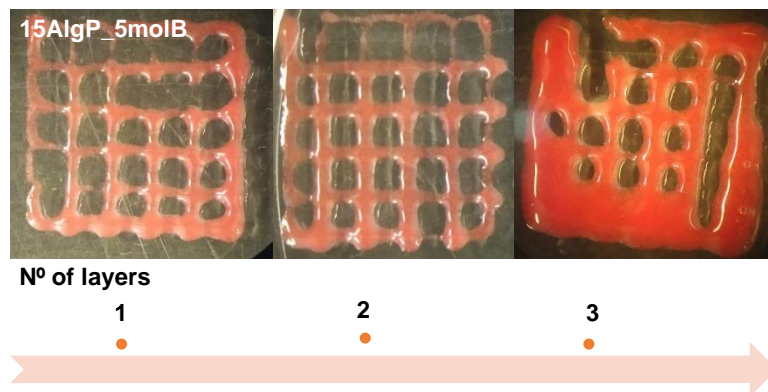


Figure 36. Optical microscopy images of 3D printed 15AlgP_5molB squared meshes with 1, 2, and 3 printed layers.

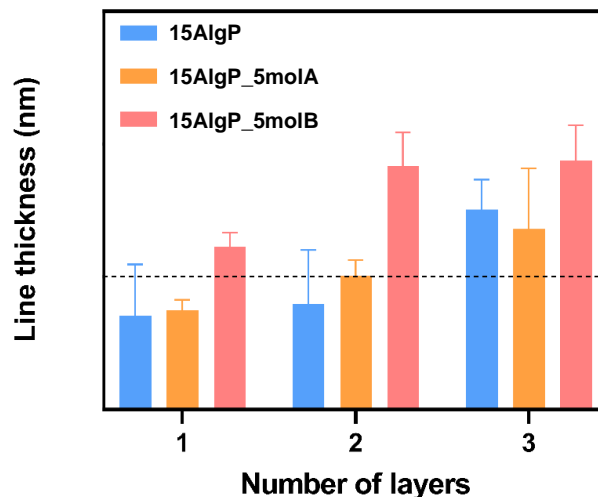
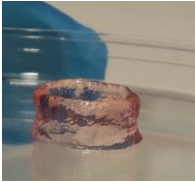
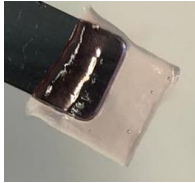


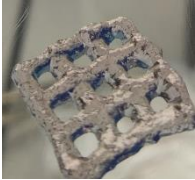
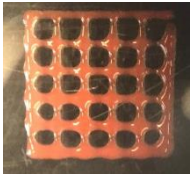
Figure 37. Line thickness over three different layers derived from the 15AlgP, 15AlgP_5molA, and 15AlgP_5molB 3D-printed hydrogels showing the expected line thickness marked with a black dotted line (x mm = pink needle inner diameter). Data are shown as mean \pm SD ($n=3$). The values from y axis are presented in a confidential annex.

4.4.2 Exploring different architectures

3D printing is a versatile technique to design different scaffold architectures that can provide physiologically relevant native-like structure to guide cells, enhance their functions and develop 3D structured tissues. 3D printed scaffolds can enable an adequate spread of media, nutrients, growth factors, and cell location. However, the scaffold can be designed to have different structures and shapes, featuring different geometric elements (layout, height, size, diameter, deposition angle, layer thickness, number of layers, and pore size). Diffusion limitation of nutrients and metabolic waste products in scaffolds is a significant constraint, and optimization in the architectural design of scaffolds provides an alternative method to circumvent those hurdles (Lee *et al.* 2008). Recently, a study showed that orthogonal-based designs can provide optimal geometry and, when combined with naturally based coatings, can promote cellular proliferation (Souness *et al.* 2018). Table 6 shows different scaffolds constructed using AlgP based inks and discusses their advantages and disadvantages.

Table 6. List of different shaped 3D printed scaffolds. An image of each scaffold is shown along with the parameters used during each printing process. Advantages and disadvantages of each structure were debated.

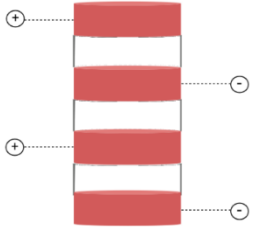
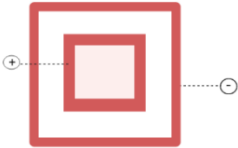
Scaffold	Printing process parameters used	Advantages	Disadvantages
	Filled circle (r = 4 mm) 20 layers Needle (inner diameter = 0.5 mm) Line speed: 20 mm.s ⁻¹ Pressure: 3 psi	Consistent structure with high mechanical properties. Fast, easy, and reproducible fabrication. Easy to handle.	The filling can provide nutrients/wastes diffusion limitations and promote necrotic zones inside the scaffold.
	Circle (r = 6 mm) 100 layers Needle (inner diameter = 0.5 mm) Line speed: 20 mm.s ⁻¹ Pressure: 10 psi	High diffusivity since the culture medium can circulate in the middle of the scaffold.	Fragile and can deform easily when manipulated.
	Film 4 mm x 4 mm 3 layers Needle (inner diameter = 0.5 mm) Line speed: 25 mm.s ⁻¹ Pressure: 2 psi	Uniform structure. Fast, easy, and reproducible fabrication. Easy to handle. Orthogonal design.	Too simple to promote adequate architecture for cell growth

	<p>Square 10 mm x 10 mm 15 layers Needle (inner diameter = 0.5 mm) Line speed: 20 mm.s⁻¹ Pressure: 7.8 psi</p>	<p>High diffusivity since the culture medium can circulate in the middle of the scaffold. Orthogonal design.</p>	<p>Fragile can deform easily when manipulated.</p>
	<p>Squared mesh 10 mm x 10 mm 10 layers (Az = 0.1 mm) Needle (inner diameter = 0.5 mm) Line speed: 20 mm.s⁻¹ Pressure: 11 psi</p>	<p>High diffusivity since the culture medium can circulate in the multiple holes of the scaffold. Orthogonal design.</p>	<p>The thickness of the lines can promote necrotic zones inside the scaffold.</p>
	<p>Squared mesh 10 mm x 10 mm 2 layers (Az = 0.5 mm) Needle (inner diameter = 0.5 mm) Line speed: 25 mm.s⁻¹ Pressure: 4 psi</p>	<p>High diffusivity since the culture medium can circulate in the multiple holes of the scaffold. Orthogonal design.</p>	<p>Probability of providing very different zones within the same structure.</p>

Designing a scaffold that can model the structure-function relationships allows to tailor it to address specific limitations and meet features of target scaffold. Multi-layered structures can provide layer-specific structure-function. depending on the purpose of the scaffold, using different materials and cell in different layers. In sum, with this approach is possible to combine techniques, materials, cell types and functions that generate multiple cell layers in a scaffold near to native tissues that possess layered structures with various biological and mechanical requirements (Knight *et al.* 2013) Goins *et al.* reviewed the multi-layer approaches that use synthetic and natural materials (Goins *et al.* 2019).

In this work, the use of a multi-layered scaffold through 3D multi-material printing was explored aiming to enhance the electrically conductive feature of the structure. This combination has the potential to improve mechanical scaffold properties and direct cell alignment. Table 7 shows selected designs relying on multi-layer approaches that use AlgP based inks and natural conjugated molecules-based inks in different layers. Table 7 also discuss advantages and disadvantages of the presented designs. Preliminary results of multi-layer constructs produced by sandwiching the different elements were achieved.

Table 7. List of different shaped 3D printed multi-layered scaffolds mounted with intercalated inks. The illustration of each scaffold is shown along the real image after the mounting. Advantages and disadvantages of each structure were debated.

Design	Scaffold	Advantages	Disadvantages
	 Circles	High diffusivity since the culture medium can circulate in the multiple holes of the scaffold.	Not uniform and consistent. More difficult to construct.
	 Films	Consistent structure with high mechanical properties.	Very low diffusivity. Extremely compact.
	Intercalated struts were not 3D printed	Easy fabrication process.	Fragile and breakable.
	Squares within each other were not 3D printed	High diffusivity since the culture medium can circulate in the hole of the scaffold.	

4.5 Cell culture

4.5.1 Cell seeding onto 3D scaffolds

Fibroblast cells were seeded onto 3D printed films (10 mm x 10 mm) of 15AlgP, 15AlgP_molA, and 15AlgP_5molB and cultured for 8 days, as previously described in Materials and Methods section (Figure 38). Cells were evaluated for proliferation rate, viability, and morphology.

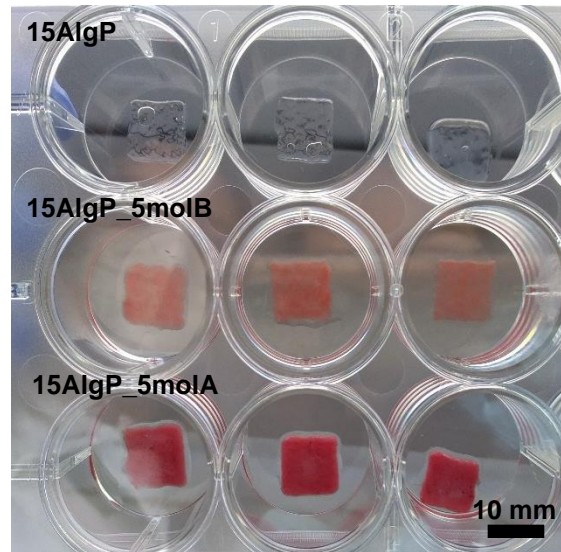


Figure 38. 3D printed films(10 mm x 10 mm) of 15AlgP, 15AlgP_5molB, and 15AlgP_5molA.

4.5.1.1 Alamar Blue

Figure 39 represents the emitted fluorescence at day 2 and day 7 after seeding fibroblasts cells on the 3D printed films (15AlgP, 15AlgP_5molB, and 15AlgP_molA). The control condition represents fibroblast cells growing in a transparent polystyrene plate. As mentioned before, the AlamarBlue™ assay measures the metabolic activity of cells rather than the cell number. In comparison to the control condition, 3D printed films conditions seem to have lowered the cellular metabolic activity of cells. This decrease in the fluorescence was more accentuated for the 3D printed films doped with natural conjugated molecules. However, this outcome can be attributed to several events, rather than just cell death. The 3D culture or the addition of natural conjugated molecules could have induced a higher lag phase or possibly lowered cellular metabolism. These hypotheses are valid but cannot be elucidated by AlamarBlue™ assay and were further evaluated using a Live/Dead viability assay.

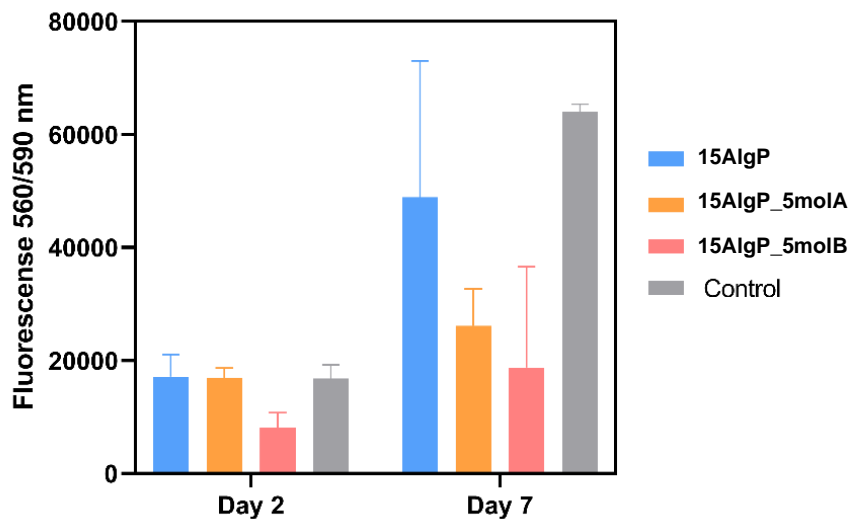


Figure 39. Proliferation assay. AlamarBlue™ reduction as an indirect estimation of cell number of mouse fibroblasts seeded in different 3D printed films. Cells were seeded in 3D printed films on day 0. At day 2 and day 7 after seeding, AlamarBlue™ was added to the medium and incubated for 2h. The reduction of AlamarBlue™ was detected using fluorescence (excitation at 560 nm and emission at 590 nm) in a plate reader. Each column shows the mean \pm SD of three independent experiments (n=3) with three 3D printed films for each condition.

4.5.1.2 Live/Dead viability assay via calcein-AM/ethidium homodimer-1

Live/Dead viability assay is based on membrane integrity and esterase activity. Plasma membrane integrity is determined by ethidium homodimer-1, which enters cells with a compromised plasma membrane to bind DNA and emit red fluorescence. On the other side, live cells are identified by calcein-AM, which is converted to a green fluorescence after interaction with intracellular esterase's. In Figure 40A, are shown the microscope images of fibroblast cells seeded onto 3D printed films. The control condition represents fibroblast cells growing in a transparent polystyrene plate. The percentage of viability was calculated (Figure 40B) accounting for the number of live (green) and dead (red) cells. All conditions showed high viabilities. However, the microscope images confirmed that the number of cells in the 3D printed films was lower than in control.

Moreover, this reduction is even more accentuated in the 3D printed films doped with natural conjugated molecules. These results confirmed the hypothesis of cells going through a higher lag phase than in controls, that led to a low cellular metabolism quantification in the AlamarBlue™ assay. The decreased fluorescence observed above was most probably due to a reduced number of cells and not cell death. However, we cannot discard the hypothesis that this cell growth inhibition could also be due to the

presence of molecules A and B. To confirm this results, we decided to perform Hoechst-Phalloidin staining to visualize in more detail the fibroblast cells on the 3D printed scaffolds.

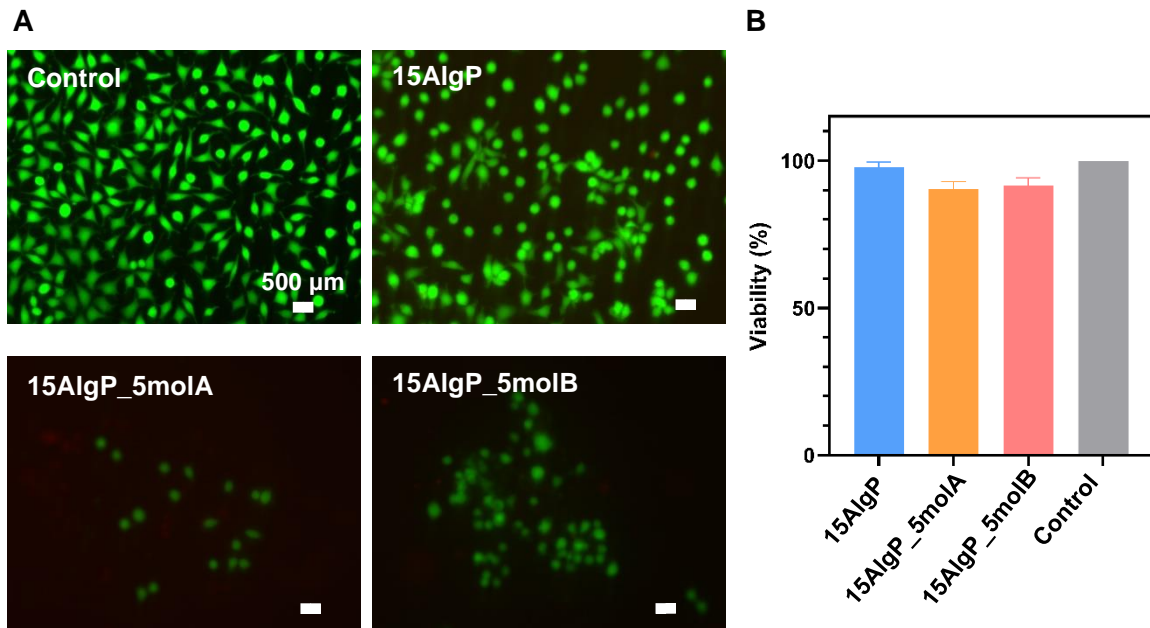


Figure 40. A) Fluorescence microscope images of L929 fibroblast cells seeded onto 3D printed films after staining with calcein/ethidium homodimer-1, at day 8. B) Cytocompatibility study of 15AlgP, 15AlgP_5molA, and 15AlgP_5molB hydrogels using a Live-Dead viability assay. Data are shown as mean \pm SD (n=3). Scale bar: 500

4.5.1.3 Hoechst-Phalloidin staining

The cytoskeleton plays a vital role in multiple cellular events, conditioning cell shape, adhesion, motility, intracellular transport, and cellular division (Galkin *et al.* 2012; Stringham *et al.* 2012). Cell adhesion to biomaterials surface is critical because, after adhesion, cells can initiate spreading and proliferation. Therefore, usually the cell adhesion and proliferation ability are an essential initial evaluation of the biocompatibility of the materials. The results on Figure 41 show the Hoechst-Phalloidin staining obtained for each condition of 3D printed film (15AlgP, 15AlgP_5molA, and 15AlgP_5molB) and control. This staining enabled the identification of actin filaments (green) which indicate fibroblast cells-film surface interactions, which were possible to be detected for all conditions. In particular, it was observed the presence of adhesion focal points at the cell periphery, indicating strong adhesion to the substrate. However, these observations were more stringent for the control than for the cells in the printed films. Indeed, compared to the control, the cells cultivated on 3D printed films showed minor cytoskeleton organization and defects in cell spreading. Moreover, cells cultivated on the films tend to form cell clusters and a rounded cell morphology suggested that the fibroblast cells need to adapt to the 3D printed films surface topography (Coradeghini *et al.* 2013).

On the other hand, in comparison to hydrophobic materials, hydrophilic surfaces as AlgP, a polysaccharide containing sulphates in the backbone, as the potential to positively influence cell

adhesion, cell proliferation, and cell differentiation. As observed before, the fabricated scaffolds have high water content and are considered superhydrophilic surfaces. In these conditions, we observed that our scaffolds promote cell adhesion in a clustered manner. These clusters led to higher cell density on the 3D printed films, associated with a round shape due to lower spreading area and higher circularity. Nishida *et al.* suggested that the bound water content suppressed the cytoskeletal organization of adhered cells in these cases (Nishida *et al.* 2021). The author distinguished bound water from intermediate and non-freezing water and discussed the concept of bound water as the water present on the material's surface. His work revealed that the increment of bound water content on the substrates decreased cell adhesion strength and cell spreading. In the future, our studies will examine this factor.

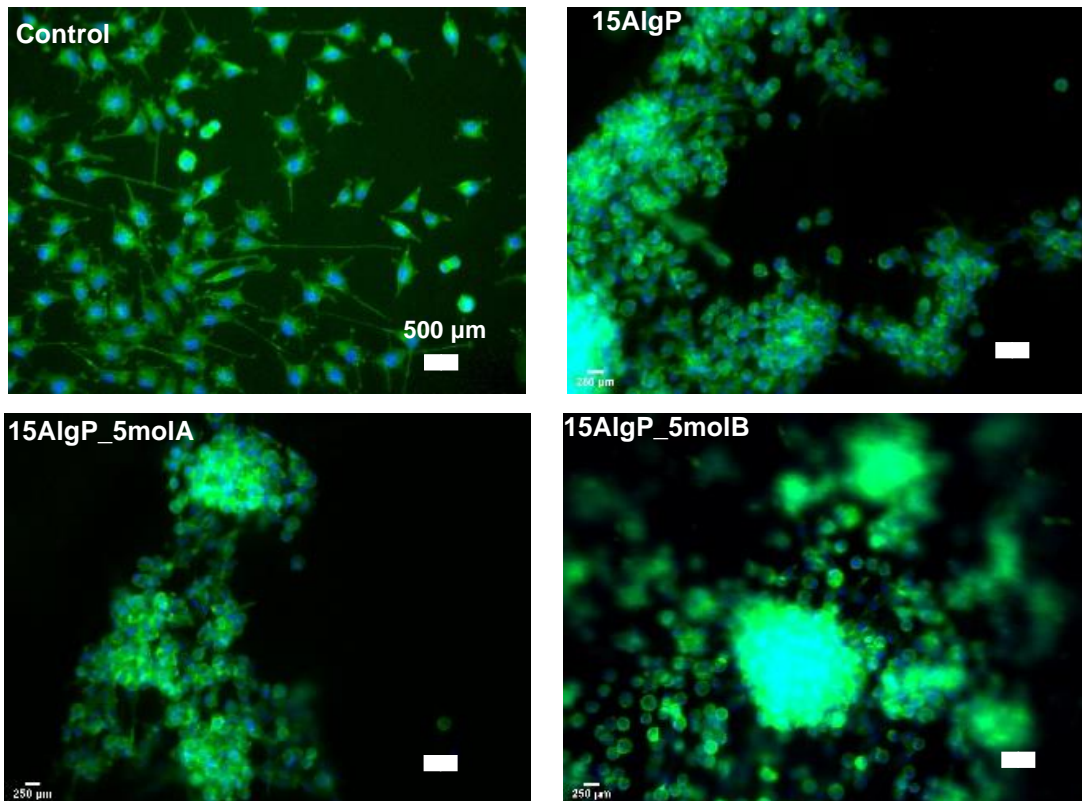


Figure 41. Fluorescence microscope images of L929 fibroblast cells adhered on 15AlgP, 15AlgP_5molA, and 15AlgP_5molB 3D printed films, after 5 days in culture. Alexa 488 Phalloidin stained actin cytoskeleton (green) and Hoechst 33342 stained the cell nuclei (blue). Scale bar: 500 μm.

The number of cell clusters observed in the Figure 41 images were categorised and quantified, and the results obtained are reported in Figure 42. There was not found statistically differences between the values on the total number of clusters for each 3D printed hydrogel (Figure 42A). A closer inspection, considering the number of cell clusters of different size for each hydrogel (Figure 42B) point out that most clusters had a small to medium size containing 20-60 cells in it. A high quantity of clusters was found for

15AlgP_5molB hydrogels, but with many of them considered as very small (10-20 cells). Interestingly, very large clusters (80-100 cells) were detected in 15AlgP and 15AlgP_5molB hydrogels.

In the future, this cell behaviour will be evaluated in more detail to improve cell adhesion and spreading throughout the scaffold.

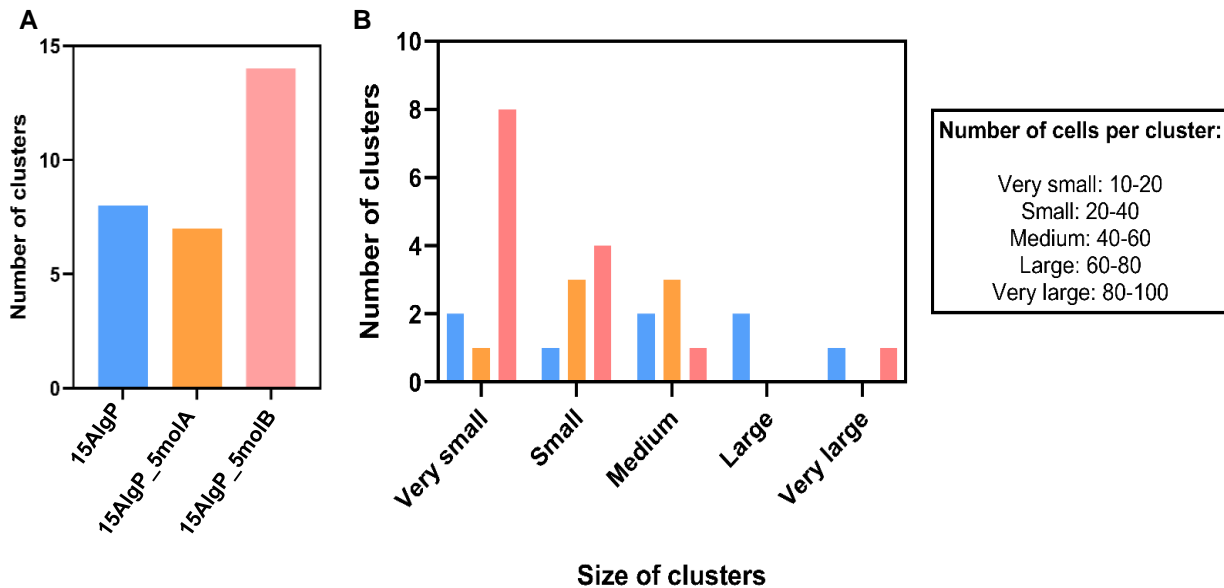


Figure 42. A) Number of clusters present at each 3D printed hydrogel (15AlgP, 15AlgP_5molA, and 15AlgP_5molB); B) separation of the clusters by size (very small, small, medium, large, and very large) according to the number of cells per cluster. The number of cells per cluster size legend is represented at right side.

4.6 3D Bioprinting

4.6.1 Bioink formulation and media optimization

As previously stated, the solvent matrix used during ink formulation was water alone. However, cell survival depends on the solvent matrix around it to contain the right salinity, nutrients, co-factors and so, the straightforward solution to address such needs is to use culture media as solvent matrix, more precisely, DMEM, that was already proved effective in maintaining cell viability (see section 4.1.2.1). However, 15AlgP ink in DMEM (15g AlgP in 1L DMEM) is not printable. Due to the high ionic concentration of DMEM, when AlgP is dissolved in DMEM, polymer helical aggregation is induced, making the sol-gel transition almost instant, and before the printing process, this ink was already solidified. We considered that 15AlgP ink in DMEM was not appropriate for bioprinting. Therefore, we considered that 15AlgP ink in DMEM was not appropriate for bioprinting.

Three novel customised media were formulated: Media 1, Media 2, and Media 3 and their cytocompatibility were evaluated via WST-8 assay, as described before. Figure 43 microscope images showed that cells were grown on DMEM (positive control), and Media 3 had similar proliferation and

morphology. The cell viability measured at 30, 60 and 120 minutes of incubation were similar for DMEM and Media 3, confirming the capacity of Media 3 to maintain cell growth and proliferation.

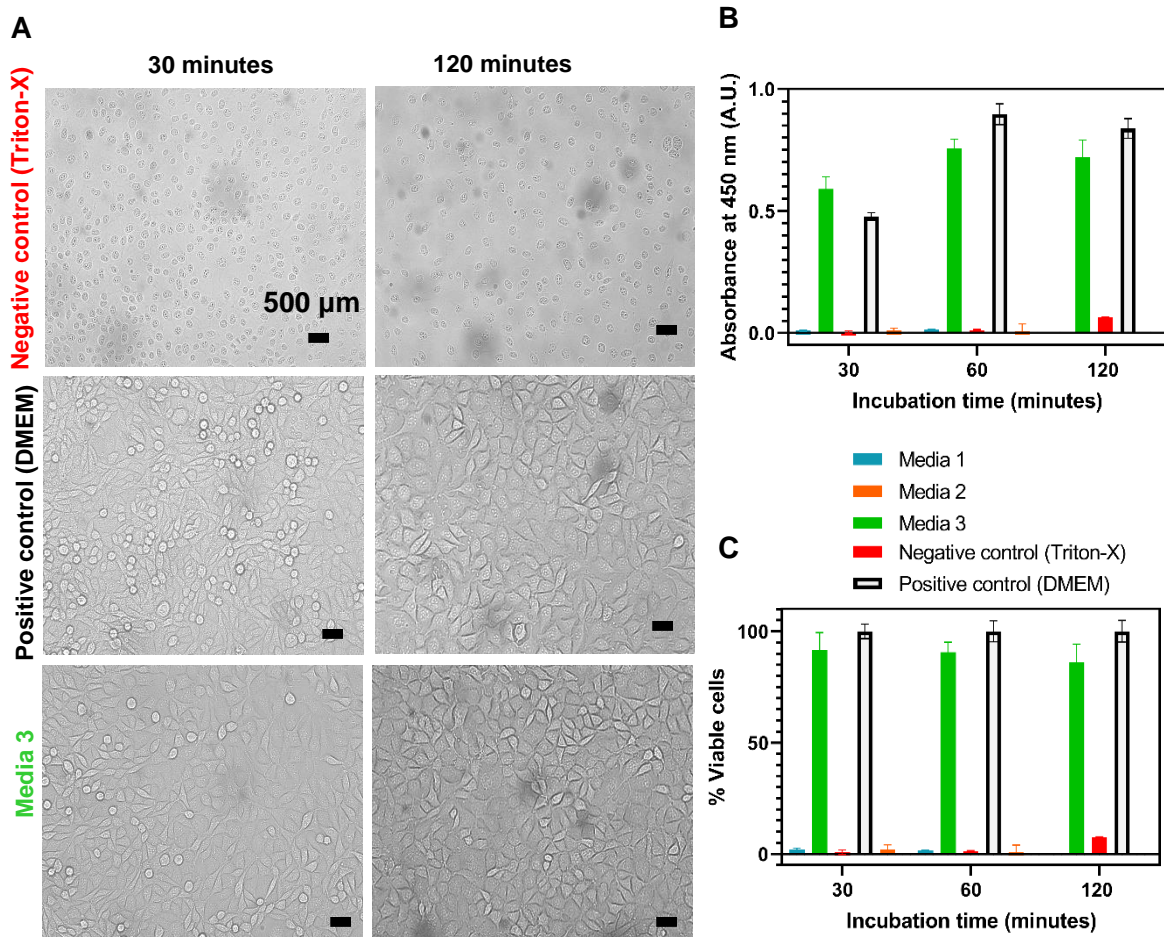


Figure 43. A) Light-microscope images of L929 fibroblast cells grown on DMEM (positive control), Triton-X (negative control), and Media 3 after 30 and 120 minutes of incubation. Cells incubated in media 3 show similar proliferation and morphology as cells incubated in DMEM. B) Respective viability percentage of L929 fibroblasts cells grown on DMEM, Triton-X, and Media 3 using a WST-8 viability assay. Viability measured at 30, 60 and 120 minutes of incubation is similar and reveals a non-significant decrease on viability when using media 3. C) Absorbance at 450 nm (A.U.), measured at 30, 60 and 120 minutes, for L929 fibroblasts cells grown on DMEM, Triton-X, and media 3. Scale bar: 500 μ m.

Media 1 and Media 2 showed cell viabilities near zero (see Annex 3 for the microscope images). The nuclei of these cells were larger revealing that cell low viability might be due to osmolarities imbalance. Therefore, Media 3 was chosen as a solvent for the AlgP based bioinks.

Novel inks with 5g.L⁻¹, 6g.L⁻¹, 7g.L⁻¹, 8g.L⁻¹, 9g.L⁻¹, and 10g.L⁻¹ AlgP in 1L of Media 3 were formulated. The optimal ink was selected from visual observation of the solution's viscous and/or fluidic behaviour at 37°C (incubation temperature) and 25°C (printing temperature) and their printed resolution.

The ink with 10g.L^{-1} was highly viscous and partially in the solid state, while the ink with 5g.L^{-1} was liquid (Figure 48A). Therefore, these inks were discarded, and only the inks with 6g.L^{-1} , 7g.L^{-1} , 8g.L^{-1} , and 9g.L^{-1} AlgP were evaluated for 3D printing performance. The ink 6g.L^{-1} resulted in a weak structure with a poor resolution that broke after printing. The other three structures are shown in Figure 48B. Due to higher resolution, the ink with 9g.L^{-1} AlgP in Media 3 was selected for further bioprinting processes

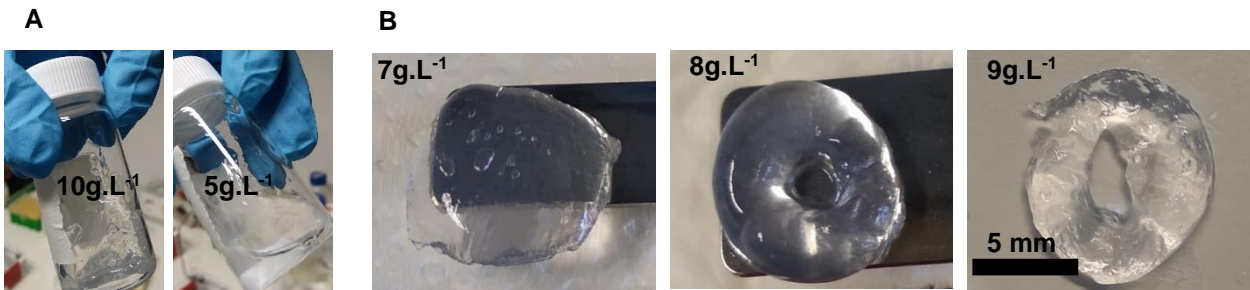


Figure 44. A) Inks with 10g.L^{-1} and 5g.L^{-1} AlgP in 1L of Media 3 showing a solid and liquid state, respectively. B) 3D printed circles. Inks with 7g.L^{-1} , 8g.L^{-1} , and 9g.L^{-1} AlgP in Media 3.

4.6.2 3D bioprinted cells

3D bioprinted rings were fabricated with the bioinks 9AlgP, 9AlgP_molA, and 9AlgP_5molB cultured for 11 days, as previously described in Materials and Methods. Cells were evaluated for viability and morphology with Live/Dead staining and through microscope images.

Figure 45 presents encapsulated fibroblast cells bioprinted with the 9AlgP bioink at day 11 with different magnitudes (x4, x10, and x20). The black dotted lines highlight interface between the ring and the culture plate, showing the curvature of the bioprinted rings. After 11 days (early-stage), the encapsulated cells were spread throughout the hydrogel with elongated morphology as in the controls. As described in the literature, bioprinting enhanced cell distribution along with the material.

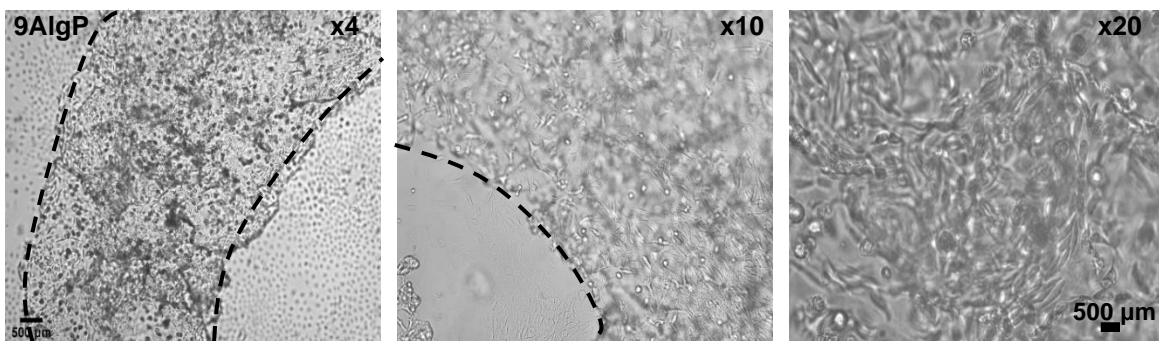


Figure 45. Light-microscope images of 3D bioprinted 9AlgP rings after 11 days in culture, at different magnitudes (x4, x10, and x20). The black dotted lines highlight the interface between the ring and the culture plate, showing the curvature of the bioprinted rings.

Figure 46 presents encapsulated fibroblast cells bioprinted with the 9AlgP bioink, 9AlgP_1molA, and 9AlgP_5molB at day 8. In all conditions, the encapsulated cells were spread throughout the hydrogel. However, the cytoskeleton organization of the fibroblasts was faster in the 9AlgP bioink than in the 9AlgP_1molA and 9AlgP_5molB. The doped bioinks presented spheroid fibroblasts. Previous studies suggest that fibroblasts encapsulated in AlgP based bioinks have the inherent potential to self-organize into 3D aggregated spheroids. Contrarily, in the 9AlgP bioink was possible to observe the change in morphology along the culture time. At this point, the culture was composed of elongated and round cells, but as seen above, within 11 days, elongated cells were predominant.

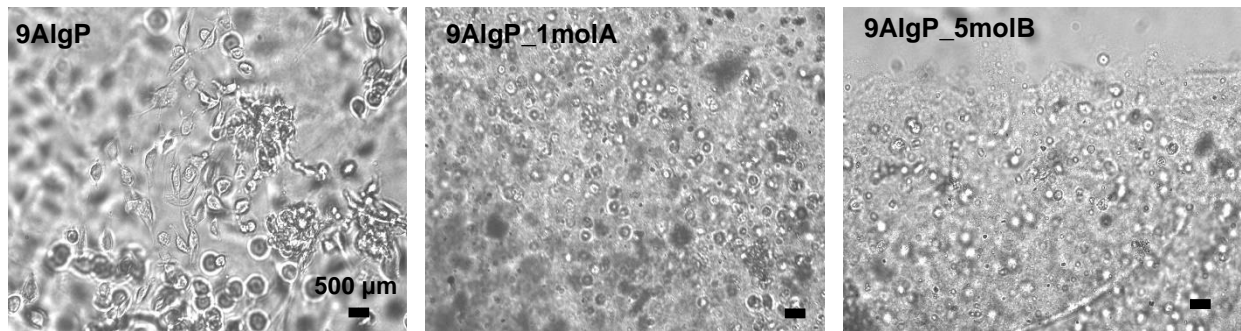


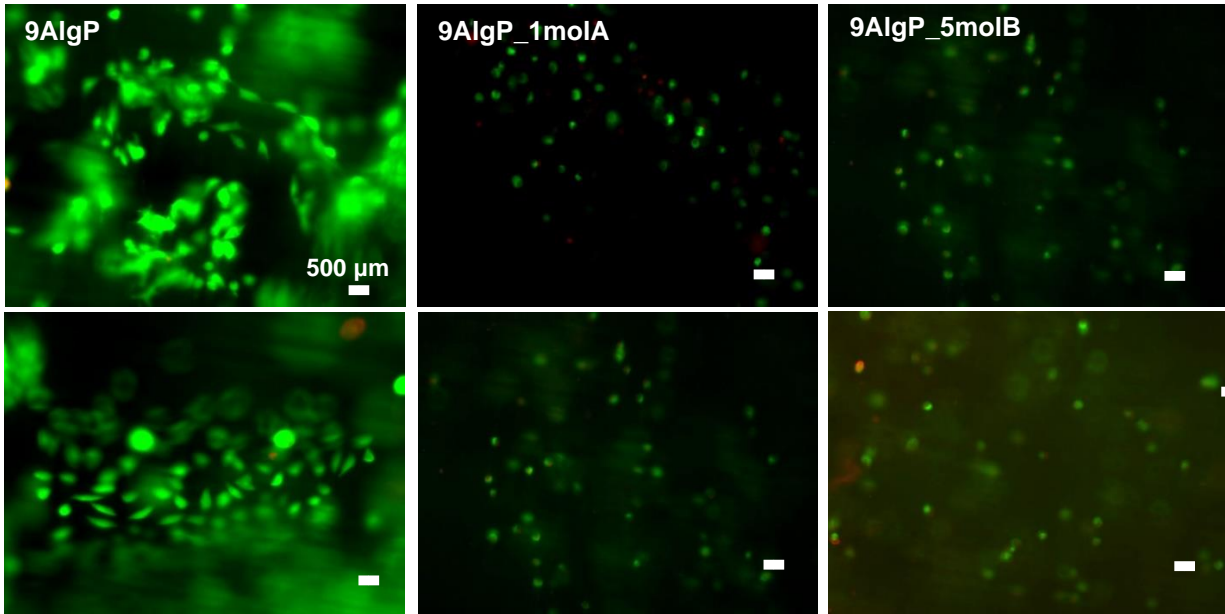
Figure 46. Light-microscope images of 3D bioprinted 9AlgP, 9AlgP_1molA, and 9AlgP_5molB rings at day 8. Scale bar: 500 μm .

Figure 47A presents the results for the Live-Dead viability assay, which uses calcein-AM/ethidium homodimer-1. These results show that most of the encapsulated fibroblast cells were viable after 8 days in culture. The presence of dead cells was negligible, which implies that the hydrogels are cyto-compatible and non-toxic. The percentage of viability was calculated (Figure 47B) by considering the number of live (green) and dead (red) cells. The fabricated hydrogels 9AlgP and 9AlgP_5molA showed high cell viability comparing to 9AlgP_5molB that had lower viability.

Moreover, due to the high natural pigmentation of natural conjugated molecules, we hypothesise that during the encapsulation at a 3D level was not possible quantify all the present viable cells. Even so, the cell viability of cells bioprinted with 9AlgP_5molB that presents in our study the lowest cell viability, still falls on the range of the values reported by other studies on extrusion-based bioprinting.

Regarding the cell morphology, previous studies suggest that fibroblasts encapsulated in AlgP based bioinks have inherent potential to self-organize into 3D aggregated spheroids. Here, this behaviour was also observed, however, within 8 days the fibroblasts encapsulated in the 9AlgP bioink acquired a more fibroblast-like morphology with a higher organised cytoskeleton.

A



B

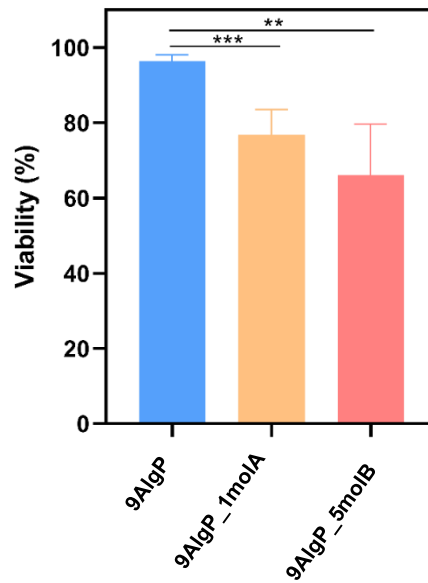


Figure 47. A) Fluorescence microscope images of 3D bioprinted L929 fibroblast cells after staining with calcein/ethidium homodimer-1, at day 8. B) Cytocompatibility study of 9AlgP, 9AlgP_1molA, and 9AlgP_5molB hydrogels using a Live-Dead viability assay. Data are shown as mean \pm SD (n=4). Scale bar: 500 μ m.

Chapter 5. Conclusions and Future Perspectives

5. Conclusions and Future Perspectives

Specific protocols for the fabrication of novel AlgP based inks and bioinks were successfully conceived. These inks were then effectively doped with two different natural conjugated molecules, molA, and molB. The fabrication of such inks was characterized via UV-vis spectroscopy and rheological assessment. UV-vis confirmed the presence of natural conjugated molecules giving colours appealing to seafood consumers.

Our novel inks were used to construct 3D scaffolds using moulds, 3D printing, and 3D Bioprinting techniques with mechanical properties adequate for cell-cultured seafood. Young's modulus values were obtained between 60-80 kPa, which falls on the same order of magnitude as in the one of tuna meat. High water content values were estimated, which is promising to develop fish tissue similar to the one of species such as cod, shrimp, and sea bass.

The novel electrically conductive inks, doped with natural conjugated molecules, were characterized with EIS, four-probe method, cyclic voltammetry (CV), and a LED light test. EIS analysis revealed that the produced hydrogels work as capacitors at low frequencies and as resistors at high frequencies. The capacitive behaviour was confirmed by an enlargement of the CV curves area with the increase of the voltage scan rate. The higher measured conductivity was from 15AlgP_1molA wet hydrogels showing to be just slightly higher than for 15AlgP alone. Four probe method conductivities for dry hydrogels reached much lower values, evidencing the predominance of ionic conductivity over electrical conductivity. A consistent behaviour was observed where to high concentrations of natural conjugated molecules resulted in lower conductivity. This behaviour may be due to the presence of particle aggregates blocking the charge motion.

After, printing assays showed that it is possible to disperse natural conjugated molecules, maintaining the printability of the hydrogels. This capacity was demonstrated by printing different scaffolds with several layers using AlgP based inks as circles, squares, films, and squared meshes.

Cell characterization was performed using mouse fibroblast cells. Cells were onto 3D printed films for 8 days to evaluate their proliferation rate, viability, and morphology. Live/Dead staining showed that all scaffolds had high viabilities. However, we hypothesised that 3D printed films doped with natural conjugated molecules had lower proliferation rates and fewer cells due to a higher lag phase. A Hoechst/Phalloidin staining uncovered that cells were adhered to the 3D printed films but with lower cytoskeleton organization and cell spreading than in control. We detected a tendency to form cell clusters and a rounded cell morphology.

Finally, cells were 3D bioprinted. For that, a novel media specific for bioprinting (Media 3) and novel bioinks were produced. These bioinks were also doped with natural conjugated molecules and then bioprinted into 3D rings scaffolds, cultured for 11 days. Most of the encapsulated cells were viable after 8 days in culture, and that the presence of dead cells was negligible. After 11 days, the encapsulated cells were spread throughout the hydrogel, exhibiting a similar morphology to the controls.

In contrast, doped 3D bioprinted scaffolds cells self-organized into 3D aggregated spheroids. This behaviour is line with literature. In sum, AlgP based exhibited minimal cytotoxicity and is a potential biomaterial for future fabricating scaffolds. Natural conjugated molecules seem to impact the scaffold electroconductive properties at low concentrations. More studies within this effective concentration range will be performed.

In the future, we ambition to reproduce this work with a fish cell line to create scaffolds specifically for cell-cultured seafood.

Chapter 6. Bibliography

6. Bibliography

- Acevedo CA, Orellana N, Avarias K, Ortiz R, Benavente D, Prieto P (2018) Micropatterning Technology to Design an Edible Film for In Vitro Meat Production. *Food Bioprocess Technol.* <https://doi.org/10.1007/s11947-018-2095-4>
- Ahmed EM (2015) Hydrogel: Preparation, characterization, and applications: A review. *J Adv Res* 6:105–121 . <https://doi.org/10.1016/j.jare.2013.07.006>
- Ahmed N, Thompson S (2019) The blue dimensions of aquaculture: A global synthesis. *Sci. Total Environ.*
- Ahmed N, Thompson S, Glaser M (2019) Global Aquaculture Productivity, Environmental Sustainability, and Climate Change Adaptability. *Environ Manage* 63:159–172 . <https://doi.org/10.1007/s00267-018-1117-3>
- Allagui A, Freeborn TJ, Elwakil AS, Maundy BJ (2016) Reevaluation of Performance of Electric Double-layer Capacitors from Constant-current Charge/Discharge and Cyclic Voltammetry. *Sci Rep* 6: . <https://doi.org/10.1038/srep38568>
- Altintzoglou T, Heide M, Altintzoglou T, Heide M (2016) Fish Quality and Consumers : How Do Consumers ' Knowledge About and Involvement in Fish Quality Define Factors That Influence Fish Buying Behavior ? Fish Quality and Consumers : How Do Consumers ' Knowledge About and Involvement in Fish Quality Define Fac. *J Aquat Food Prod Technol* 25:885–894 . <https://doi.org/10.1080/10498850.2014.964432>
- Ambekar RS, Kandasubramanian B (2019) Progress in the Advancement of Porous Biopolymer Scaffold: Tissue Engineering Application. *Ind Eng Chem Res.* <https://doi.org/10.1021/acs.iecr.8b05334>
- Ansar Ahmed S, Gogal RM, Walsh JE (1994) A new rapid and simple non-radioactive assay to monitor and determine the proliferation of lymphocytes: an alternative to [3H]thymidine incorporation assay. *J Immunol Methods* 170:211–224 . [https://doi.org/10.1016/0022-1759\(94\)90396-4](https://doi.org/10.1016/0022-1759(94)90396-4)
- Arulkumar A, Paramasivam S, Rajaram R (2017) Toxic heavy metals in commercially important food fishes collected from Palk Bay, Southeastern India. *Mar Pollut Bull.* <https://doi.org/10.1016/j.marpolbul.2017.03.045>
- Bandaranayake CM, Vidanapathirana KP, Perera KS (2015) A Cyclic Voltammetry study of a gel polymer electrolyte based redox-capacitor. 16:19–27
- Barboza LGA, Dick Vethaak A, Lavorante BRBO, Lundebye AK, Guilhermino L (2018) Marine microplastic debris: An emerging issue for food security, food safety and human health. *Mar. Pollut. Bull.*
- Ben-Arye T, Shandalov Y, Ben-Shaul S, Landau S, Zagury Y, Ianovici I, Lavon N, Levenberg S (2020) Textured soy protein scaffolds enable the generation of three-dimensional bovine skeletal muscle

- tissue for cell-based meat. *Nat Food*. <https://doi.org/10.1038/s43016-020-0046-5>
- Bo Z, Wen Z, Kim H, Lu G, Yu K, Chen J (2012) One-step fabrication and capacitive behavior of electrochemical double layer capacitor electrodes using vertically-oriented graphene directly grown on metal. *Carbon N Y* 50:4379–4387 . <https://doi.org/10.1016/j.carbon.2012.05.014>
- Bockris, John O'M. and Reddy AKN (1998) ION TRANSPORT IN SOLUTIONS. In: *Modern Electrochemistry* 1. pp 361–599
- Bosch AC, O'Neill B, Sigge GO, Kerwath SE, Hoffman LC (2016) Heavy metals in marine fish meat and consumer health: A review. *J. Sci. Food Agric*.
- Bouaamlat H, Hadi N, Belghiti N, Sadki H, Naciri Bennani M, Abdi F, Lamcharfi TD, Bouachrine M, Abarkan M (2020) Dielectric Properties, AC Conductivity, and Electric Modulus Analysis of Bulk Ethylcarbazole-Terphenyl. *Adv Mater Sci Eng* 2020: . <https://doi.org/10.1155/2020/8689150>
- Bryan Walsh (2013) The Triple Whopper Environmental Impact of Global Meat Production. *Time*
- Bryant C, Szejda K, Parekh N, Desphande V, Tse B (2019) A Survey of Consumer Perceptions of Plant-Based and Clean Meat in the USA, India, and China. *Front Sustain Food Syst*. <https://doi.org/10.3389/fsufs.2019.00011>
- Carletti E, Motta A, Migliaresi C (2011) Scaffolds for tissue engineering and 3D cell culture. *Methods Mol. Biol*.
- Chen H, Liu S, Xu XR, Diao ZH, Sun KF, Hao QW, Liu SS, Ying GG (2018) Tissue distribution, bioaccumulation characteristics and health risk of antibiotics in cultured fish from a typical aquaculture area. *J Hazard Mater*. <https://doi.org/10.1016/j.jhazmat.2017.09.017>
- Cheung W, Bruggeman J, Butenschon M (2018) Projected changes in global and national potential marine fisheries catch under climate change scenarios in the twenty-first century
- Choudhury D, Tseng TW, Swartz E (2020) The Business of Cultured Meat. *Trends Biotechnol*. <https://doi.org/10.1016/j.tibtech.2020.02.012>
- Coradeghini R, Gioria S, García CP, Nativo P, Franchini F, Gilliland D, Ponti J, Rossi F (2013) Size-dependent toxicity and cell interaction mechanisms of gold nanoparticles on mouse fibroblasts. *Toxicol Lett* 217:205–216 . <https://doi.org/10.1016/j.toxlet.2012.11.022>
- Corbett DC, Olszewski E, Stevens K (2019) A FRESH Take on Resolution in 3D Bioprinting. *Trends Biotechnol*.
- CQ Press (2020) National Oceanic and Atmospheric Administration. In: *Federal Regulatory Guide*
- Distler T, Polley C, Shi F, Schneidereit D, Ashton MD, Friedrich O, Kolb JF, Hardy JG, Detsch R, Seitz H,

- Boccaccini AR (2021) Electrically Conductive and 3D-Printable Oxidized Alginate-Gelatin Polypyrrole:PSS Hydrogels for Tissue Engineering. *Adv Healthc Mater* 10:1–16 . <https://doi.org/10.1002/adhm.202001876>
- Edelman PD, McFarland DC, Mironov VA, Matheny JG (2005) In vitro-cultured meat production. *Tissue Eng.*
- Enrione J, Blaker JJ, Brown DI, Weinstein-Oppeneheimer CR, Pepczynska M, Olguín Y, Sánchez E, Acevedo CA (2017) Edible scaffolds based on non-mammalian biopolymers for myoblast growth. *Materials (Basel)* 10:1–15 . <https://doi.org/10.3390/ma10121404>
- FAO (2020) *The State of World Fisheries and Aquaculture 2020. Sustainability in action.*
- Farady SE (2019) Microplastics as a new, ubiquitous pollutant: Strategies to anticipate management and advise seafood consumers. *Mar Policy* 104:103–107 . <https://doi.org/10.1016/j.marpol.2019.02.020>
- Fraeye I, Kratka M, Vandeburgh H, Thorrez L (2020) Sensorial and Nutritional Aspects of Cultured Meat in Comparison to Traditional Meat: Much to Be Inferred. *Front Nutr.* <https://doi.org/10.3389/fnut.2020.00035>
- Freire FCM (2010) Impedance spectroscopy of conductive commercial hydrogels for electromyography and electroencephalography. *Physiol Meas* 31: . <https://doi.org/10.1088/0967-3334/31/10/S01>
- Galkin VE, Orlova A, Egelman EH (2012) Actin filaments as tension sensors. *Curr Biol* 22:R96–R101 . <https://doi.org/10.1016/j.cub.2011.12.010>
- Galloway TS, Cole M, Lewis C (2017) Interactions of microplastic debris throughout the marine ecosystem. *Nat. Ecol. Evol.*
- Gattuso JP, Magnan AK, Bopp L, Cheung WWL, Duarte CM, Hinkel J, Mcleod E, Micheli F, Oschlies A, Williamson P, Billé R, Chalastani VI, Gates RD, Irisson JO, Middelburg JJ, Pörtner HO, Rau GH (2018) Ocean solutions to address climate change and its effects on marine ecosystems. *Front Mar Sci.* <https://doi.org/10.3389/fmars.2018.00337>
- Gerhardt C, Suhlmann G, Ziemßen F, Donnan D, Warschun M, Kühnle HJ (2020a) How will cultured meat and meat alternatives disrupt the agricultural and food industry? *Ind Biotechnol.* <https://doi.org/10.1089/ind.2020.29227.cge>
- Gerhardt C, Warschun M, Donnan D, Ziemßen F (2020b) When consumers go vegan, how much meat will be left on the table for agribusiness? *A.T. Kearney* 1–16
- Goegan P, Johnson G, Vincent R (1995) Effects of serum protein and colloid on the alamarBlue assay in cell cultures. *Toxicol Vitro* 9:257–266 . [https://doi.org/10.1016/0887-2333\(95\)00004-R](https://doi.org/10.1016/0887-2333(95)00004-R)

- Goins A, Webb AR, Allen JB (2019) Multi-layer approaches to scaffold-based small diameter vessel engineering: A review. *Mater Sci Eng C* 97:896–912 . <https://doi.org/10.1016/j.msec.2018.12.067>
- Halpern BS, Maier J, Lahr HJ, Blasco G, Costello C, Cottrell RS, Deschenes O, Ferraro DM, Froehlich HE, McDonald GG, Millage KD, Weir MJ (2021) The long and narrow path for novel cell-based seafood to reduce fishing pressure for marine ecosystem recovery. *Fish Fish* 22:652–664 . <https://doi.org/10.1111/faf.12541>
- Haryanto, Khan MM (2018) Electrically Conductive Polymers and Composites for Biomedical Applications. In: *Electrically Conductive Polymer and Polymer Composites*
- Heidemann MS, Molento CFM, Reis GG, Phillips CJC (2020) Uncoupling Meat From Animal Slaughter and Its Impacts on Human-Animal Relationships. *Front. Psychol.*
- Henson SA, Beaulieu C, Ilyina T, John JG, Long M, Séférian R, Tjiputra J, Sarmiento JL (2017) Rapid emergence of climate change in environmental drivers of marine ecosystems. *Nat Commun.* <https://doi.org/10.1038/ncomms14682>
- Hockaday LA, Kang KH, Colangelo NW, Cheung PYC, Duan B, Malone E, Wu J, Girardi LN, Bonassar LJ, Lipson H, Chu CC, Butcher JT (2012) Rapid 3D printing of anatomically accurate and mechanically heterogeneous aortic valve hydrogel scaffolds. *Biofabrication.* <https://doi.org/10.1088/1758-5082/4/3/035005>
- Hocquette JF (2016) Is in vitro meat the solution for the future? *Meat Sci.* <https://doi.org/10.1016/j.meatsci.2016.04.036>
- Khademhosseini A, Langer R (2016) A decade of progress in tissue engineering. *Nat Protoc.* <https://doi.org/10.1038/nprot.2016.123>
- Khrunyk Y, Lach S, Petrenko I, Ehrlich H (2020) Progress in Modern Marine Biomaterials Research. *Mar Drugs* 18:589 . <https://doi.org/10.3390/md18120589>
- Kirchmayer DM, Gorkin R, In Het Panhuis M (2015) An overview of the suitability of hydrogel-forming polymers for extrusion-based 3D-printing. *J Mater Chem B.* <https://doi.org/10.1039/c5tb00393h>
- Knight T, Basu J, Rivera EA, Spencer T, Jain D, Payne R (2013) Fabrication of a multi-layer three-dimensional scaffold with controlled porous micro-architecture for application in small intestine tissue engineering. *Cell Adhes Migr* 7:267–274 . <https://doi.org/10.4161/cam.24351>
- Kyle S, Jessop ZM, Al-Sabah A, Whitaker IS (2017) ‘Printability’ of Candidate Biomaterials for Extrusion Based 3D Printing: State-of-the-Art.’ *Adv. Healthc. Mater.*
- Lasia A (1999) Electrochemical Impedance Spectroscopy and its Applications. *Mod Asp Electrochem* 32:143–248

- Laurent VM, Kasas S, Yersin A, Schäffer TE, Catsicas S, Dietler G, Verkhovsky AB, Meister JJ (2005) Gradient of rigidity in the lamellipodia of migrating cells revealed by atomic force microscopy. *Biophys J* 89:667–675 . <https://doi.org/10.1529/biophysj.104.052316>
- Lee M, Wu BM, Dunn JCY (2008) Effect of scaffold architecture and pore size on smooth muscle cell growth. *J Biomed Mater Res - Part A* 87:1010–1016 . <https://doi.org/10.1002/jbm.a.31816>
- Lenas D, Chatziantoniou S, Nathanailides C, Triantafillou D (2011) Comparison of wild and farmed sea bass (*Dicentrarchus labrax* L) lipid quality. *Procedia Food Sci* 1:1139–1145 . <https://doi.org/10.1016/j.profoo.2011.09.170>
- Liu X, Steele JC, Meng XZ (2017a) Usage, residue, and human health risk of antibiotics in Chinese aquaculture: A review. *Environ Pollut*. <https://doi.org/10.1016/j.envpol.2017.01.003>
- Liu Z, Zhang M, Bhandari B, Wang Y (2017b) 3D printing: Printing precision and application in food sector. *Trends Food Sci. Technol.*
- Liyanage GY, Illango A, Manage PM (2021) Prevalence and Quantitative Analysis of Antibiotic Resistance Genes (ARGs) in Surface and Groundwater in Meandering Part of the Kelani River Basin in Sri Lanka. *Water Air Soil Pollut* 232:1–11 . <https://doi.org/10.1007/s11270-021-05300-2>
- MacQueen LA, Alver CG, Chantre CO, Ahn S, Cera L, Gonzalez GM, O'Connor BB, Drennan DJ, Peters MM, Motta SE, Zimmerman JF, Parker KK (2019) Muscle tissue engineering in fibrous gelatin: implications for meat analogs. *npj Sci Food* 3:1–12 . <https://doi.org/10.1038/s41538-019-0054-8>
- Manage PM (2018) Heavy use of antibiotics in aquaculture: Emerging human and animal health problems – A review. *Sri Lanka J Aquat Sci*. <https://doi.org/10.4038/sljias.v23i1.7543>
- Mandrycky C, Wang Z, Kim K, Kim DH (2016) 3D bioprinting for engineering complex tissues. *Biotechnol. Adv.*
- Marwaha Nisha, Beveridge Malcom PM (2020) Alternative seafood : Assessing food, nutrition and livelihood futures of plant-based and cell-based seafood. *WorldFish* 22–23
- Mason-Jenkins G (1991) Consumer Concerns About Seafood. *J Food Distrib Res* 57–66
- Maulu S, Hasimuna OJ, Haambiya LH, Monde C, Musuka CG, Makorwa TH, Munganga BP, Phiri KJ, Nsekanabo JDM (2021) Climate Change Effects on Aquaculture Production: Sustainability Implications, Mitigation, and Adaptations. *Front Sustain Food Syst* 5: . <https://doi.org/10.3389/fsufs.2021.609097>
- Menzies KL, Jones L (2010) The impact of contact angle on the biocompatibility of biomaterials. *Optom Vis Sci* 87:387–399 . <https://doi.org/10.1097/OPX.0b013e3181da863e>

- Mirdamadi E, Tashman JW, Shiwarski DJ, Palchesko RN, Feinberg AW (2020) FRESH 3D bioprinting a full-size model of the human heart. *ACS Biomater Sci Eng*. <https://doi.org/10.1021/acsbiomaterials.0c01133>
- Mishra D, Shanker K, Khare P (2020) Nanocellulose-mediated fabrication of sustainable future materials. In: *Sustainable Nanocellulose and Nanohydrogels from Natural Sources*
- Mitchell M (2011) Increasing fish consumption for better health - are we being advised to eat more of an inherently unsustainable protein? *Nutr Bull* 36:438–442 . <https://doi.org/10.1111/j.1467-3010.2011.01926.x>
- Modulevsky DJ, Lefebvre C, Haase K, Al-Rekabi Z, Pelling AE (2014) Apple derived cellulose scaffolds for 3D mammalian cell culture. *PLoS One*. <https://doi.org/10.1371/journal.pone.0097835>
- Moxon SR, Cooke ME, Cox SC, Snow M, Jeys L, Jones SW, Smith AM, Grover LM (2017) Suspended Manufacture of Biological Structures. *Adv Mater* 29: . <https://doi.org/10.1002/adma.201605594>
- Nagarajan S, Radhakrishnan S, Kalkura SN, Balme S, Miele P, Bechelany M (2019) Overview of Protein-Based Biopolymers for Biomedical Application. *Macromol. Chem. Phys*.
- Ngwabebhoh FA, Yildiz U (2019) Nature-derived fibrous nanomaterial toward biomedicine and environmental remediation: Today's state and future prospects. *J. Appl. Polym. Sci*.
- Nishida K, Anada T, Kobayashi S, Ueda T, Tanaka M (2021) Effect of bound water content on cell adhesion strength to water-insoluble polymers. *Acta Biomater* 134:313–324 . <https://doi.org/10.1016/j.actbio.2021.07.058>
- Nisticò R (2017) Aquatic-derived biomaterials for a sustainable future: A European opportunity. *Resources*
- Nociari MM, Shalev A, Benias P, Russo C (1998) A novel one-step, highly sensitive fluorometric assay to evaluate cell-mediated cytotoxicity. *J Immunol Methods* 213:157–167 . [https://doi.org/10.1016/S0022-1759\(98\)00028-3](https://doi.org/10.1016/S0022-1759(98)00028-3)
- ONU (2019) *World population prospects 2019*
- Orellana N, Sánchez E, Benavente D, Prieto P, Enrione J, Acevedo CA (2020) A new edible film to produce in vitro meat. *Foods*. <https://doi.org/10.3390/foods9020185>
- Ortiz RM (2001) Osmoregulation in marine mammals. *J Exp Biol* 204:1831–1844 . <https://doi.org/10.1242/jeb.204.11.1831>
- Ouyang L, Yao R, Zhao Y, Sun W (2016) Effect of bioink properties on printability and cell viability for 3D bioplotting of embryonic stem cells. *Biofabrication* 8:1–12 . <https://doi.org/10.1088/1758-5090/8/3/035020>

- Pal K, Banthia AK, Majumdar DK (2009) Polymeric hydrogels: Characterization and biomedical applications. *Des Monomers Polym* 12:197–220 . <https://doi.org/10.1163/156855509X436030>
- Phelps LN, Kaplan JO (2017) Land use for animal production in global change studies: Defining and characterizing a framework. *Glob. Chang. Biol.*
- Place ES, George JH, Williams CK, Stevens MM (2009) Synthetic polymer scaffolds for tissue engineering. *Chem Soc Rev.* <https://doi.org/10.1039/b811392k>
- Post MJ (2014) An alternative animal protein source: Cultured beef. *Ann N Y Acad Sci.* <https://doi.org/10.1111/nyas.12569>
- Potter G, Smith AST, Vo NTK, Muster J, Weston W, Bertero A, Maves L, Mack DL, Rostain A (2020) A More Open Approach Is Needed to Develop Cell-Based Fish Technology: It Starts with Zebrafish. *One Earth*
- Premathilake D, Outlaw RA, Parler SG, Butler SM, Miller JR (2017) Electric double layer capacitors for ac filtering made from vertically oriented graphene nanosheets on aluminum. *Carbon N Y* 111:231–237 . <https://doi.org/10.1016/j.carbon.2016.09.080>
- Pulakkat S, Patravale VB (2020) Marine Resources for Biosynthesis and Surface Modification of Anticancer Nanoparticles. In: *Green Synthesis of Nanoparticles: Applications and Prospects*
- Reddy PP (2015) Climate resilient agriculture for ensuring food security
- Rogers ZJ, Zeevi MP, Koppes R, Bencherif SA (2020) Electroconductive Hydrogels for Tissue Engineering: Current Status and Future Perspectives. *Bioelectricity* 2:279–292 . <https://doi.org/10.1089/bioe.2020.0025>
- Rojas-Downing MM, Nejadhashemi AP, Harrigan T, Woznicki SA (2017) Climate change and livestock: Impacts, adaptation, and mitigation. *Clim. Risk Manag.*
- Rubio N, Datar I, Stachura D, Kaplan D, Krueger K (2019) Cell-Based Fish: A Novel Approach to Seafood Production and an Opportunity for Cellular Agriculture. *Front Sustain Food Syst* 3:1–13 . <https://doi.org/10.3389/fsufs.2019.00043>
- Rubio NR, Xiang N, Kaplan DL (2020) Plant-based and cell-based approaches to meat production. *Nat Commun* 11:6276 . <https://doi.org/10.1038/s41467-020-20061-y>
- Sarkar A, VanLoon GW, Sensarma SR (2019) Sustainable solutions for food security: Combating climate change by adaptation
- Scanes CG (2017) Impact of Agricultural Animals on the Environment. In: *Animals and Human Society*
- Schar D, Klein EY, Laxminarayan R, Gilbert M, Van Boeckel TP (2020) Global trends in antimicrobial use in aquaculture. *Sci Rep* 10:21878 . <https://doi.org/10.1038/s41598-020-78849-3>

- Sciences N (1992) Measurement of Young's Modulus and Poisson's Ratio of Tuna Fish. OGAWA, Yutaka 9:283–290
- Senior JJ, Cooke ME, Grover LM, Smith AM (2019) Fabrication of Complex Hydrogel Structures Using Suspended Layer Additive Manufacturing (SLAM). *Adv Funct Mater* 29:1–10 . <https://doi.org/10.1002/adfm.201904845>
- Shi Z, Gao X, Ullah MW, Li S, Wang Q, Yang G (2016) Electroconductive natural polymer-based hydrogels. *Biomaterials*
- Soares RMD, Siqueira NM, Prabhakaram MP, Ramakrishna S (2018) Electrospinning and electrospray of bio-based and natural polymers for biomaterials development. *Mater. Sci. Eng. C*
- Souness A, Zamboni F, Walker GM, Collins MN (2018) Influence of scaffold design on 3D printed cell constructs. *J Biomed Mater Res - Part B Appl Biomater* 106:533–545 . <https://doi.org/10.1002/jbm.b.33863>
- Spence C (2021) What's the Story With Blue Steak? On the Unexpected Popularity of Blue Foods. *Front Psychol* 12:1–17 . <https://doi.org/10.3389/fpsyg.2021.638703>
- Stading M, Hermansson AM (1990) Viscoelastic behaviour of β -lactoglobulin gel structures. *Food Hydrocoll* 4:121–135 . [https://doi.org/10.1016/S0268-005X\(09\)80013-1](https://doi.org/10.1016/S0268-005X(09)80013-1)
- Stephens N, Di Silvio L, Dunsford I, Ellis M, Glencross A, Sexton A (2018) Bringing cultured meat to market: Technical, socio-political, and regulatory challenges in cellular agriculture. *Trends Food Sci. Technol.*
- Stringham EG, Marcus-Gueret N, Ramsay L, Schmidt KL (2012) Live cell imaging of the cytoskeleton. Elsevier Ltd.
- Sun S, Titushkin I, Cho M (2006) Regulation of mesenchymal stem cell adhesion and orientation in 3D collagen scaffold by electrical stimulus. *Bioelectrochemistry* 69:133–141 . <https://doi.org/10.1016/j.bioelechem.2005.11.007>
- Sun T, Wu H, Wang X, Ji C, Shan X, Li F (2020) Evaluation on the biomagnification or biodilution of trace metals in global marine food webs by meta-analysis. *Environ Pollut.* <https://doi.org/10.1016/j.envpol.2019.113856>
- Tilman D, Clark M (2014) Global diets link environmental sustainability and human health. *Nature.* <https://doi.org/10.1038/nature13959>
- van Ruth SM, Brouwer E, Koot A, Wijtten M (2014) Seafood and water management. *Foods* 3:622–631 . <https://doi.org/10.3390/foods3040622>
- Venugopal V, Shahidi F (1996) Structure and composition of fish muscle. *Food Rev Int* 12:175–197 .

<https://doi.org/10.1080/87559129609541074>

Warren H, in het Panhuis M (2014) Electrical conductivity and impedance behaviour of hydrogel materials. *Nanobiosystems Process Charact Appl* VII 9171:917103 . <https://doi.org/10.1117/12.2066370>

Weng L, Chen X, Chen W (2007) Rheological characterization of in situ crosslinkable hydrogels formulated from oxidized dextran and N-carboxyethyl chitosan. *Biomacromolecules* 8:1109–1115 . <https://doi.org/10.1021/bm0610065>

Wernberg T, Bennett S, Babcock RC, De Bettignies T, Cure K, Depczynski M, Dufois F, Fromont J, Fulton CJ, Hovey RK, Harvey ES, Holmes TH, Kendrick GA, Radford B, Santana-Garcon J, Saunders BJ, Smale DA, Thomsen MS, Tuckett CA, Tuya F, Vanderklift MA, Wilson S (2016) Climate-driven regime shift of a temperate marine ecosystem. *Science* (80-). <https://doi.org/10.1126/science.aad8745>

WWF (2015) Living Blue Planet Report. Species, habitats and human well-being

Xu W, Wang X, Sandler N, Willför S, Xu C (2018) Three-Dimensional Printing of Wood-Derived Biopolymers: A Review Focused on Biomedical Applications. *ACS Sustain. Chem. Eng.*

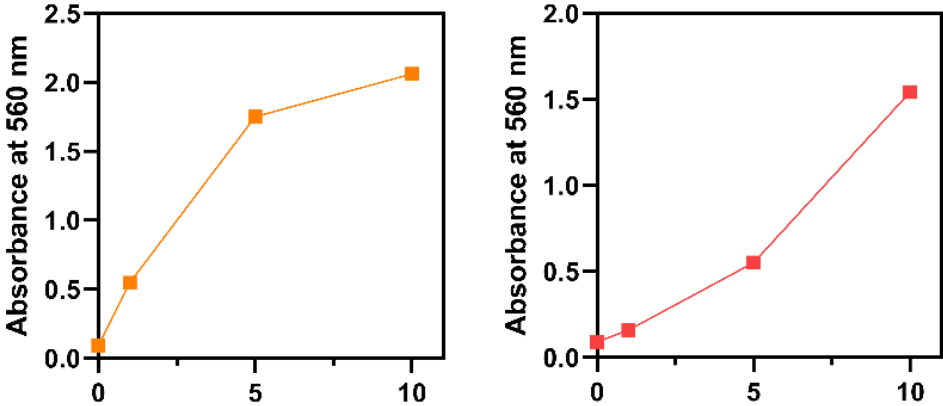
Zhang C, Li X, Kim SK (2012) Application of marine biomaterials for nutraceuticals and functional foods. *Food Sci. Biotechnol.*

Zhao P, Gu H, Mi H, Rao C, Fu J, Turng L sheng (2018) Fabrication of scaffolds in tissue engineering: A review. *Front. Mech. Eng.*

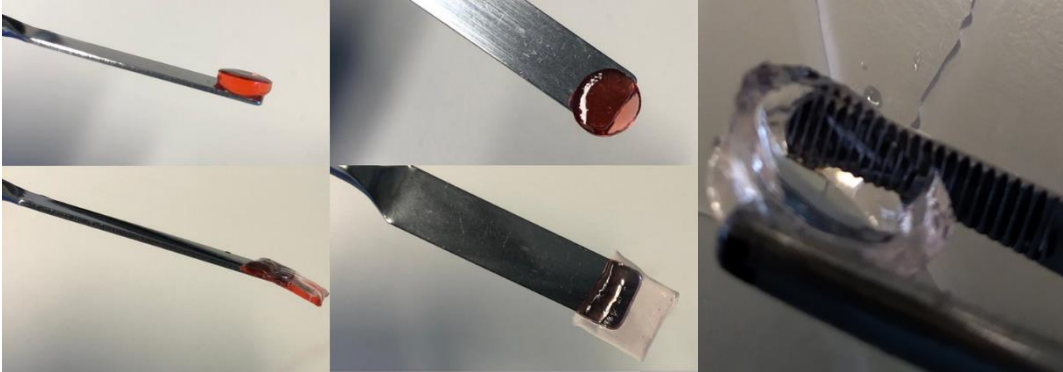
Zhu W, Ma X, Gou M, Mei D, Zhang K, Chen S (2016) 3D printing of functional biomaterials for tissue engineering. *Curr. Opin. Biotechnol.*

Chapter 7. Annexes

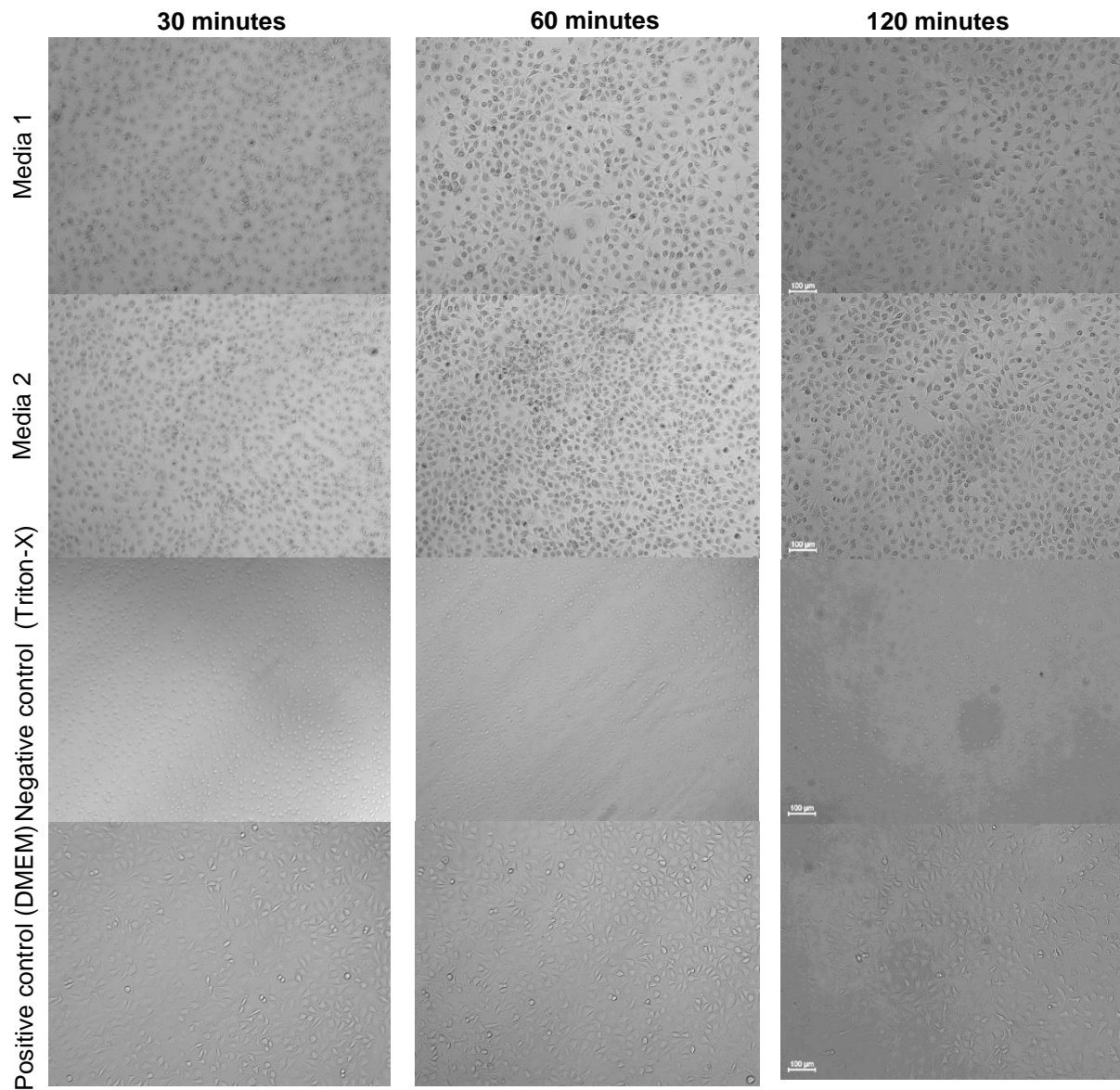
7. Annexes



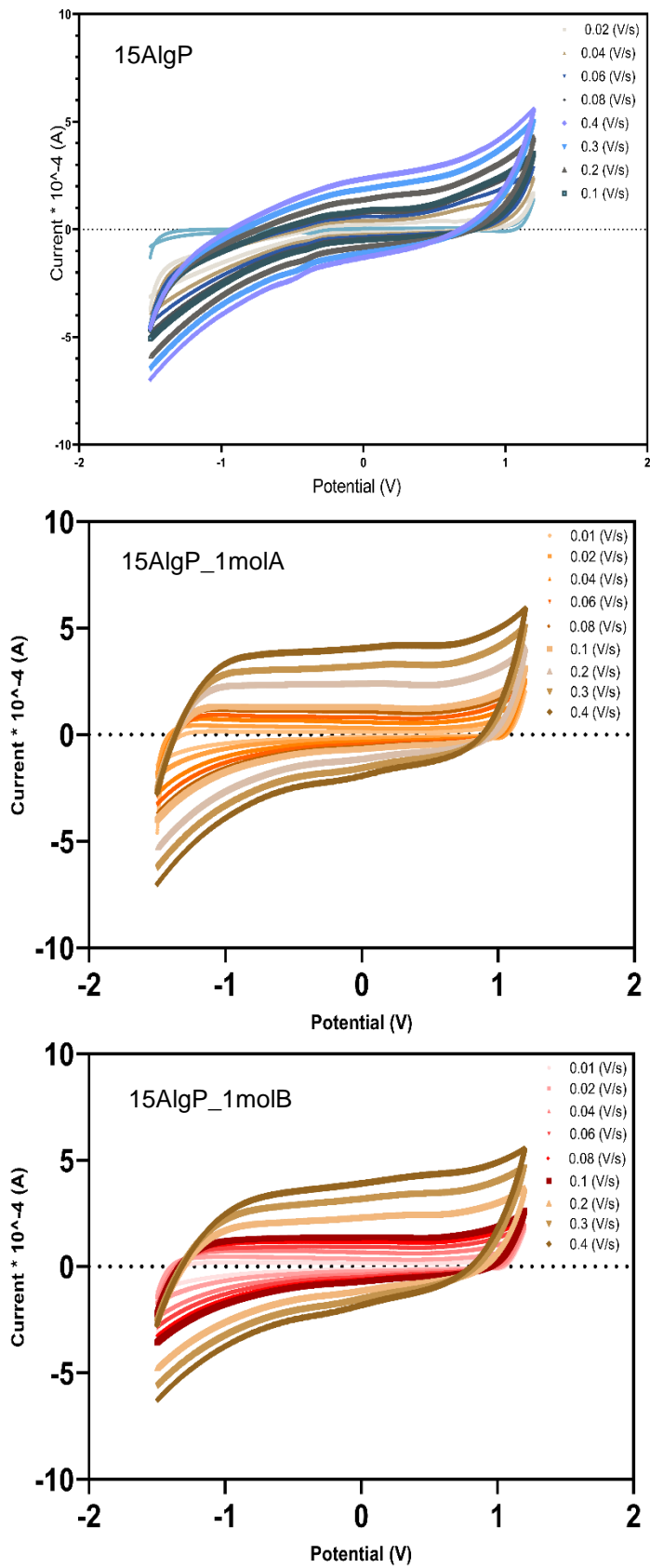
Annex 1. Calibration curves of molecule A and molecule B concentrations at 560 nm.



Annex 2. 3D printed structures showing being manipulated using tweezers and a spatula, with no permanent deformation observed.



Annex 3. Microscope images of the mouse fibroblast cells at 30, 60 and 120 minutes of incubation with DMEM (positive control), Triton-X (negative control), Media 1, and Media 2. Media 1 and Media 2 showed cytotoxic with morphologies like the negative control. The nuclei of these cells were larger revealing that cell low viability might be due to osmolarities imbalance.



Annex 4. Cyclic measurements at different scan rates for the hydrogels 15AlgP, 15AlgP_1molA, and 15AlgP_1molB showing the enlargement of the curve with the increase of the scan rate.